Year : 2016

Université de Lille 1 SCIENCES ET TECHNOLOGIES

Dimensional Measurement of Metallic Object by 3D Vision

A PhD. Dissertation

By

PETER OLUWANISOLA FASOGBON

SNCF RÉSEAU

CRIStAL Centre de Recherche en Informatique, Signal et Automatique de Lille

NOVEMBER 23, 2016

Thesis Committee

Reviewers :	Fabrice MERIAUDEAU	Professor, Univ. Bourgogne, and Univ. Teknologi Petronas
	Bernd JAHNE	Professor, Universitat Heidelberg
Examiner :	Luce MORIN	Professor, INSA de Rennes
Invited :	Stephane AVRONSART	Engineer, French Railway Company (SNCF)
Supervisors :	Ludovic MACAIRE	Professor, Universite de Lille1
	Luc DUVIEUBOURG	Associate Professor, Universite du Littoral-Cote-d'Opale

Abstract

The preventive maintenance of the railway contact wires is very critical to the proper functioning of the railway company. In this PhD thesis, we have demonstrated through various studies and experiments the necessity of using 3D vision system to measure the cross-section area of the contact wires. The major drawback of the present state of art Contact Wire Wear Measurement System is that they measure the wire wear using 2D image processing. Therefore, we have proposed a Contact Wire Wear Measurement System that measures the cross-section of any contact wire using 3D computer vision techniques. The proposed system consists of lasers and Scheimpflug optical devices. The Scheimpflug device is made up of a camera and a special optical lens which ensures that the sensor plane is tilted at double angles with reference to the camera's optical axis. This is a non-classical optical set-up that increases the field of view.

As we have to measure the contact wire using the laser-Scheimpflug device, we need to calibrate the system. We proposed a new calibration method suited for 3D laser-Scheimpflug device triangulation system. It is a two-step calibration process that first estimates the intrinsic parameter of the Scheimpflug device, then determines the laser plane parameters in the calibrated camera coordinate system. The method provides significant improvement on the calibration error compared to the state of art triangulation system.

We have also proposed a method that estimates the cross-section of contact wires directly from their images, that are acquired by the proposed system. First, we use a method to extract the pixels that correspond to the laser line profile projected on the contact wire. Thereafter, these pixels are transformed to the 3D profile by triangulation using the proposed laser-camera calibration method. Finally, a profile analysis method is proposed to determine the cross-section of the contact wire directly from the reconstructed profile. We have validated the system capability both on plug gauge and challenging contact wire samples.

Keywords : *Calibration, Scheimpflug, Laser stripe extraction, Triangulation, 3D reconstruction, Point analysis, Region growing, Sub-pixel interpolation, Gaussian filter, Regression, Bundle adjustment, Polygonal approximation, Rectification*

RÉSUMÉ

Dans cette thèse nous avons montré à travers différentes études et expériences la nécessité de mesurer la section de pièces métalliques.

Les méthodes actuelles sont basées sur des systèmes de vision 2D, ce qui ne permet pas de traiter toutes les géométries possibles. Par conséquent nous avons proposé d'utiliser des méthodes de vision 3D basées sur un couplage laser caméra et sur un dispositif optique de type Scheimpflug.

Ce dispositif non conventionnel augmente le champ de vue focalisé de la caméra. La mesure dimensionnelle de la pièce nécessite une calibration spécifique d'un tel système. Nous avons donc proposé des méthodes de calibrage dont les performances dépassent celles de l'état de l'art.

Une fois le système calibré, la mesure de la section est obtenue par une analyse du profil résultant de la projection du plan laser sur la pièce. La capacité du système développé a été évaluée avec des pièces étalons.

Mots cles : *Calibrage, Scheimpflug, Triangulation, Vision 3D, Mesure dimensionnelle*

Dedication and acknowledgements

This PhD has been successful thanks to the precious contributions of various people over the years. My first gratitude goes to my supervisors, Ludovic Macaire and Luc Duvieubourg, for giving me the chance to work under them. Their support, guidance and patience over the years have given the driving force to go forward through my PhD project. They have transferred to me huge courage and confidence that has helped me a lot in the technical aspect and team work ability required under this PhD project. I learned from them the importance of defining precisely the scientific challenges in a research project, emphasis, and rigorous thinking before a decision is made. Their advice, suggestions and regular communication were very supportive and helpful for me to make my work have better shape and thus more valuable. I really enjoy the ability to analyse problems and discuss together as a team. They have transferred to me the art of illustrating complex scientific ideas in elegant and simple way for every people from different backgrounds of disciplines through reports and presentations.

I will also like to thank my director at SNCF, Stephane Avronsart, who gave me the possibility of working on this interesting and challenging project, which will have positive impact on the future of railway industries. To do a PhD that combines both research and engineering to real world problems is a dream come true. Working on this huge project has prepared me for future in providing solutions to any industrial problems using computer vision. I reserve a special gratitude to my supervisor at SNCF Pierre-Antoine Lacaze for his cooperation and involvement in my PhD project. In spite of the distance, the scientific meetings and discussions with him always end with clearer picture in my mind about the problem and best way to address it directly from engineering view. His experience in railway R&D and software engineering have been very useful on my PhD project. I learned a lot from him during the past years and he has always there for problems regarding real experimental tests, and programming issues. Finally, I will like to thank the project manager at the SNCF Samuel Dubois for his constant help during various experimental tests. He has helped me integrate well into the SNCF working environment, and collaboration with their industrial project partners. I learned from him various efficient ways to manage projects in a huge industrial context.

Thank you to my all the PhD committee members including my reviewers for their time and effort in accurately validating and deeming acceptable my PhD project. Their valuable comments and feedback before and after the defence have been important. I would like to thank all our research group members and everybody associated with CRISTAL Lab including the PhD and post-doctoral students for the great and friendly research atmosphere we had together during the years. Also, I would like to thank the members of the Camescat project that we have had regular technical meetings and worked together over the years. I will like to thank all my friends home and abroad who contributed to making sure I was in a good state of mind to properly accomplish

this thesis. They have been there in the time of troubles to make my stay in France enjoyable from the first day I arrived in this country. Their moral support and compassion have helped me a lot reach the end of a successful PhD thesis. Finally, I would like to thank all of my family members from far away for their priceless support, love, and their prayers.

My gratitude goes to CIFRE-ANRT that made possible this PhD by bringing collaboration between a public research laboratory and an industry. This convention has allowed me to pursue my dream under a PhD that allows the required balance between research and engineering. Finally, my thanks to region Nord-pas-de Calais in France for their finances from the university point of view.

List of Publications

[1] P. Fasogbon, L. Duvieubourg, P. A. Lacaze, and L. Macaire, *Intrinsic camera calibration equipped with scheimpflug optical device*, in proceedings of the 12th international conference on Quality Control and Artificial Vision (QCAV), 2015, Vol. 9534, pp. 16,Äì17.

[2] P. Fasogbon, L. Duvieubourg, and L. Macaire, *Scheimpflug camera calibration using lens distortion model*, in proceedings of IAPR international conference on Computer Vision and Image Processing (CVIP), 2016, Vol. 459 (Springer AISC).

[3] P. Fasogbon, L. Duvieubourg, and L. Macaire, *A fast and precise peak detector for a 3D laser sensor*, in proceedings of the 12th international conference on Uncertainty Modelling in Knowledge Engineering and Decision Making (FLINS), 2016.

[4] P. Fasogbon, L. Duvieubourg, and L. Macaire, *Fast laser stripe extraction for 3D metallic objects*, in proceedings of the 42nd IEEE Industrial Electronics Conference (IECON), 2016 (To Appear)

TABLE OF CONTENTS

LIST OF TABLES

List of Figures

ABBREVIATIONS

CW	**C**ontact **W**ire
CS	**C**ross **S**ection
DC	**D**irect **C**urrent
AC	**A**lternating **C**urrent
CSA	**C**ross **S**ection **A**rea
SRT	**S**pecular **R**eflection **T**echnique
OCS	**O**verhead **C**ontact **S**ystem
CWWMS	**C**ontact **W**ire **W**ear **M**easurement **S**ystem
SNCF	**S**ociété **N**ationale des **C**hemins de fer **F**rançais (French Railway company)
RFI	Italian railway
FS	Finland railway
3D	Three Dimension
2D	Two Dimension
LLS	**L**inear **L**east **S**quare
WLS	**W**eighted **L**east **S**quare
SVD	**S**ingular **V**alue **D**ecomposition
DLT	**D**irect **L**inear **T**ransformation
LM	**L**evenberg **M**arquardt
ROI	**R**egion **O**f **I**nterest
CaMeSCat	Catenary Section Measurement System
EMA	**E**paisseur **M**inimale **A**dmissible (Minimum Acceptable Thickness)
JR	**J**apanese **R**ailway
RENFE	Spanish Railway Company
ATON	Netherland Railway Company CWWMS
MEDES	Spanish Railway Company CWWMS
EPFC	French Railway Company CWWMS
CRS	**C**ontact Wire **R**ecording **S**ystem
RMSE	**R**oot **M**ean **S**quare **E**rror
FOV	**F**ield **O**f **V**iew
DOF	**D**epth **O**f **F**ield
PID	**P**roportional **I**ntegral **D**erivative

SYMBOLS

Symbol	Description	
	Contact Wire	
w, W	the wear width in pixels, and mm	
r_{cw}	the contact wire radius	
A_{cw}	the contact wire worn section area	
CSA	the contact wire cross-section area	
T_{cw}	the residual contact wire thickness	
	Scalar and Matrix	
$(O_w[X_w, Y_w, Z_w])_w$	World coordinate system	
$(O_c[X_c, Y_c, Z_c])_c$	Camera coordinate system	
$(P_w[X_w, Y_w, Z_w])_w$	World coordinate point	
$(P_c[X_c, Y_c, Z_c])_c$	Camera coordinate point	
Untilted Plane		
$(O_I[x, y, z])_I$	Image coordinate system	
$(O_p[u, v])_p$	Pixel coordinate system	
$(p[x, y, z])_I$	Undistorted Image coordinate of projected point	
$(\tilde{p}[\tilde{x}, \tilde{y}, \tilde{z}])_I$	Distorted Image coordinate of projected point	
$(p[u, v])_p$	Undistorted Pixel coordinate of projected point	
$(\tilde{p}[\tilde{u}, \tilde{v}])_p$	Distorted Pixel coordinate of projected point	
Tilted Plane		
$(O_I \equiv O_t[x_t, y_t, z_t])_t$	Image coordinate system	
$(O_t[u_t, v_t])_p$	Pixel coordinate system	
$(p_t[x_t, y_t, z_t])_I$	Undistorted Image coordinate of projected point	
$(\tilde{p_t}[\tilde{x_t}, \tilde{y_t}, \tilde{z_t}])_I$	Distorted Image coordinate of projected point	
$(p_t[u_t, v_t])_p$	Undistorted Pixel coordinate of projected point	
$(\tilde{p_t}[\tilde{u_t}, \tilde{v_t}])_p$	Distorted Pixel coordinate of projected point	
˜	distortion symbol	
ˆ	estimated symbol	
$(O_{st}[X_{st}, Y_{st}, Z_{st}])_{st}$	Laser calibration target coordinate	

CHAPTER 1

INTRODUCTION

Railway infrastructures must be regularly inspected to ensure their working order. Therefore, early detection of faults will avoid costly damage [56]. The maintenance task is generally performed with the use of full inspection train such as French railway company (SNCF) IRIS 320 [73], Italian Geocat system [25] and Japanese Dr. yellow [47]. The emergence of computer vision field has provided non-contact and automated tools to carry out maintenance of railway infrastructures. They include detection of missing sleepers and fasteners [57, 58, 66, 88, 113], obstacle detection [16, 23, 69, 108], pantograph related problems [44, 77], etc. There are still lots of improvement to be made in the inspection of overhead catenary system because railway industries still rely largely on human inspection. The main drawback of human inspection is the need to switch off the high voltage wire to be inspected for long period, which avoids circulation of commercial trains during this period.

According to recent statistics from SNCF field test, the accumulated delays of trains caused by contact wire incidents amount to more than 135 days lost in a year. Contact wire incidents are mainly caused by wire breakage. So, it is important to estimate the degree of contact wire wear before it reaches critical condition. This will allow earlier replacement planning for the wires whose thickness is too small. Between 2001 and 2009, SNCF has tested several Contact Wire Wear Measurement Systems (CWWMS) on the railway network. The main conclusion from these experiments is that no present measurement system meets the required performance expected by the SNCF. Therefore, contact wire maintenance still largely relies on human inspection, which is cumbersome, and time consuming.

In the first part, we briefly present the overhead catenary system used on the SNCF network. Then we describe the specifications about contact wire inspection. The second part is dedicated

to the state of art review about Contact Wire Wear Measurement System (CWWMS) that are based on 3 visual strategies, shadowgraphy, analysis of the acquired contact wire images thanks to single and multiple views. In the final part, we briefly present the specifications of our project and the main contributions in this PhD thesis.

1.1 Overhead Contact System

The Overhead Contact System (OCS) is the electric system of a railway network. From figure 1.1, the overhead system components are named as following, (1) Mast or Pole, (2) Cantilever arm, (3) Insulator, (4) Catenary wire, (5) Connection cable, (6) Dropper or supporting wire, (7) Auxiliary contact wire, (8) Contact Wire, and (9) Pantograph.

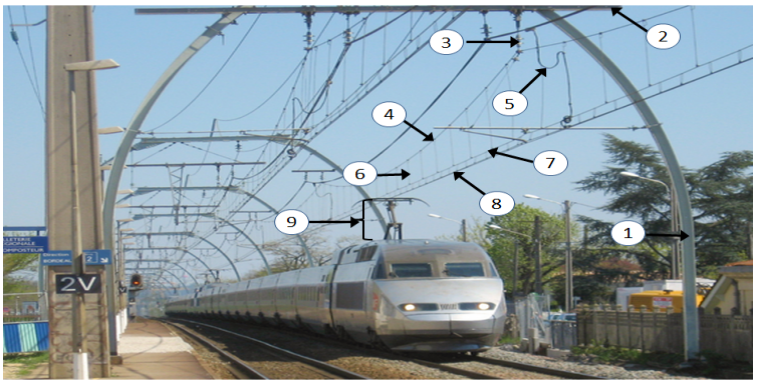

Figure 1.1: The Overhead Contact System (1)-(9)

Contact wires are parallel to the railway track, thanks to the sagged catenary wires. The electricity is transferred to the contact wire through connection cable woven around the dropper, and a clamp is attached at the end of the dropper to hold the contact wire directly from the catenary one (see figure 1.2). The pantograph is the structure mounted on the roof of the train. It has a conducting strip on its top-head that transfers electricity to the train, through sliding across the surface of the contact wire by means of a moving train [77].

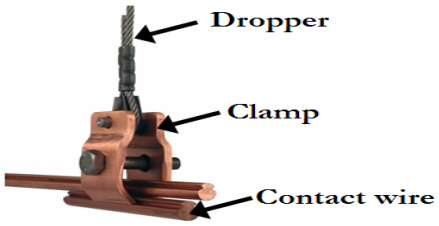

Figure 1.2: Connecting structure of the OCS.

Historically, there exist in France two types of power supply for the railway network with the OCS. The first system emerged in early 1922, and uses low voltage rating of 1.5kV DC. In

1953, the high voltage 25kV AC was completed, and has then become the standard electrification all over the world. However, since substantial amounts of RFF's network, especially at the south of Paris have already been electrified at 1.5kV DC, SNCF therefore engaged in some major electrification projects which lead to the development of a dual-voltage locomotives, which requires the use of two 1.5kV DC contact wire types. The use of these two 1.5kV DC contact wires is mostly common on conventional rail (maximum train speed < 80km/h). We refer to the overhead systems that use a single 25kV contact wire as single unit and those with double 1.5kV as double unit installation, respectively (see figure 1.3).

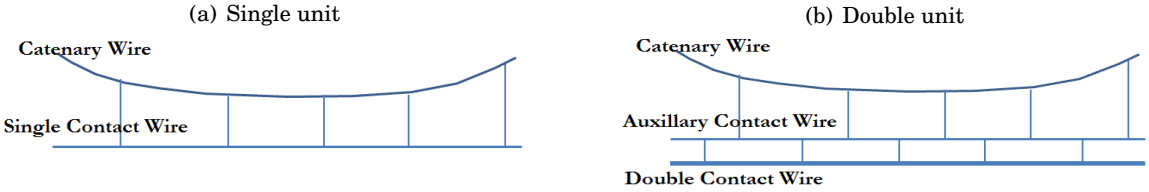

Figure 1.3: Overhead Contact System installation types.

1.1.1 Contact Wire

The location of contact wire varies across the OCS. Figure 1.4 shows the area where the contact wire has to be inspected. This area is delimited by two extreme points **A** and **B**. A 3D coordinate system is placed at the center of the railway track, so that the train moves along y-axis. The distance between the contact wire and the railway track along the vertical direction (z-axis) ranges between 4200mm and 6300mm. Moreover, the contact wire moves along X-axis according to 900mm. The wire can move in the area **A-B**, except when the train enters into a tunnel or railway station, which means that the vertical distance between point **A** and the rooftop is largely reduced.

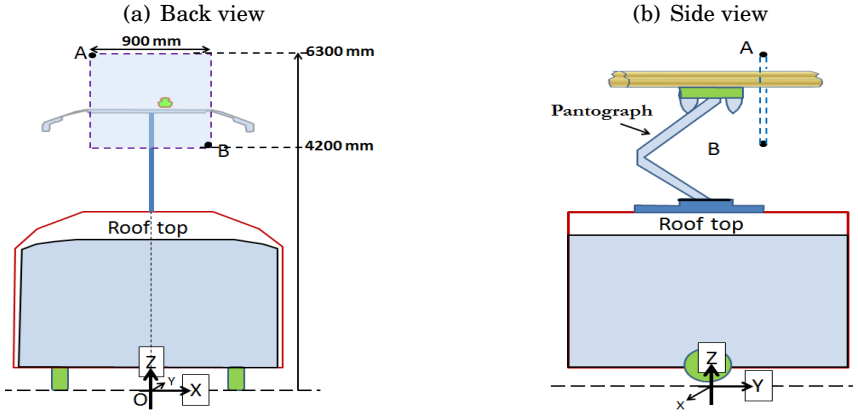

Figure 1.4: Description of the measurement area.

1.1.1.1 Dimension

The contact wires used by SNCF are grouped into "Round" and "Oval" types. Figure 1.5 illustrates the contact wire profile for both the round and oval wires. As contact wire is circular in shape, we describe it with three parameters: center O_{cw}, radius r_{cw}, and thickness T_{cw}. The two wire types are symmetrically grooved on the left and right parts of the circle to form a hollow/notch part. The presence of groove facilitates attachment of the clamp that holds contact wire to the catenary wire.

For the round wire, the radius r_{cw} is constant along the wire surface (excluding the notch region) unlike oval wire that has an almost flat surface "weak curvature" at the bottom-end of the wire. The geometric shape of the round wire makes easy to estimate its cross-section area (CSA) using circle area properties.

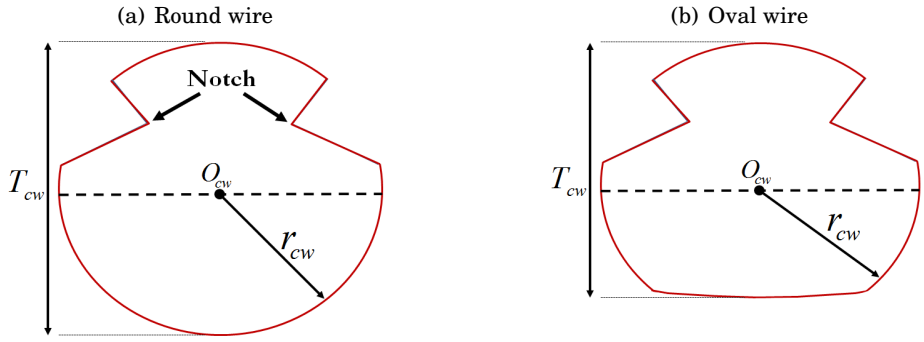

Figure 1.5: Round and oval contact wire types.

From recent statistics, all high speed rails (maximum train speed ≥ 80km/h) now use the round wire type, while the oval type can be found mostly on the conventional rail (speed < 80km/h). Contact wires are traditionally made from copper alloys. This is due to their durability, mechanical strength, high resistance to corrosion, excellent electrical and thermal conductivity. Examples of used copper alloys are copper silver (CuAg), copper tin (CuSn), copper cadmium (CuCd), copper magnesium (CuMg) etc. Contact wires are generally manufactured in different cross-section areas (CSA) ranging between 107 mm^2 and 150 mm^2 (see table 1.1). These nominal CSA values are calculated with the exclusion of the notch area.

	Round wire			Oval wire	
	BC-107	BC-120	BC-150	BF-107	BF-150
r_{cw} (mm)	6.12 ± 0.1	6.42 ± 0.1	7.25 ± 0.1	6.43 ± 0.08	7.55 ± 0.1
T_{cw} (mm)	12.24	12.85	14.50	11.35	13.60
CSA (mm^2)	108.182	119.386	151.461	108.8435	153.1293

Table 1.1: Dimension of SNCF contact wires.

1.1.1.2 Surface aspect

The surface aspect of contact wire located in outdoor condition changes during the time. These wires undergo numerous modifications from chemical reaction with the environment, and carbon polish deposits on the wire surface. So, it is difficult to define a single reflectance function of the wire surface in the visible domain. Figure 1.6 shows the different surface aspects of contact wire.

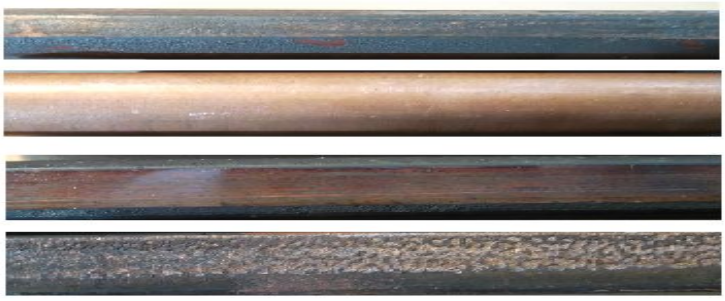

Figure 1.6: Different surface aspects of the contact wire.

1.1.1.3 Grease deposit

The material used to manufacture the contact strip that is located on top of the pantograph affects the life-cycle of the contact wire. Recent contact strip is made of carbon band which increases life-cycle of the wire, whereas the old pantograph uses a combination of steel-copper strip which reduces largely the wire's life-cycle. Therefore, some OCSs on the SNCF network (mostly on conventional lines) that use old pantograph still require projection of grease to the wires. This will ensure that the life-cycle of polished wires increases largely. The grease is made up of about 5 % copper powder, mineral oil and a thickener powder as shown in figure 1.7(a).

(a) Grease appearance

(b) Adverse effect

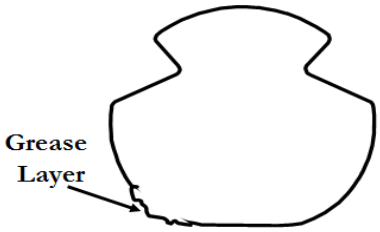

Figure 1.7: Contact wire grease deposit.

As the pantograph slides across the contact wire by means of a moving train, the left-over grease forms a thick surface layer at the side of the contact wire. In most cases, the surface layer deforms the profile of the contact wire as shown in figure 1.7(b).

1.1.1.4 Wear

The continuous friction between the pantograph and the wire leads to gradual wear on the contact wire surface. An illustration of a wear for round wire is shown in figure 1.8, where W is the wear width. By comparing this worn-out wire with the new one shown in figure 1.5a, one can see that the remaining thickness T_{cw} of the worn-out wire is reduced. The wear illustrated in figure 1.8 is a standard one, because the wear segment is perfectly horizontal. Therefore, one can use some geometrical wire models to estimate the remaining cross-section area, thickness T_{cw} or worn-out area directly from the measured width W. SNCF use cross-section area, Spanish railway company (RENFE) use the worn-out area, and Japanese railway (JR) use the thickness measure to determine the degree of a contact wire wear.

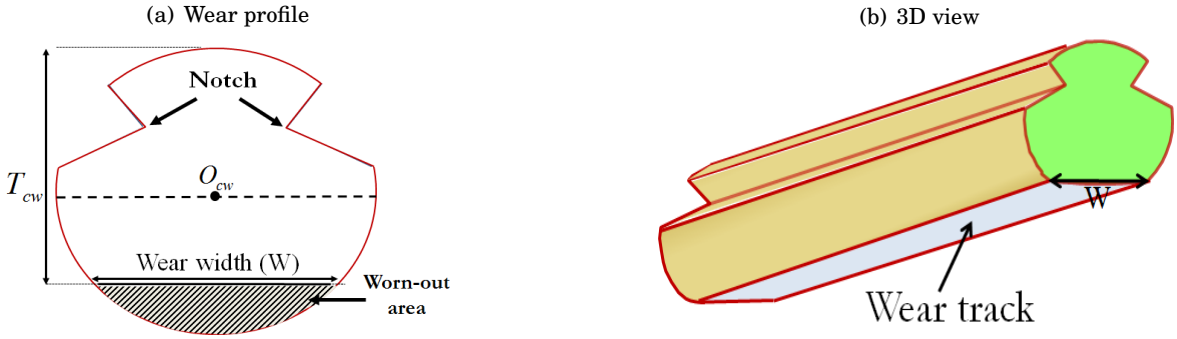

Figure 1.8: Description of contact wire wear profile.

The position of contact wire varies in the measurement area described in figure 1.4. The contact surface between the wire and pantograph depends on the wire location. This results in complex wear profiles that are formed whenever the wire comes in contact with the pantograph. Few examples of wire profiles due to wear are shown in figure 1.9. The profiles in figures 1.9(a-b) are characterized by a single wear segment, where (a) is a standard (horizontal) wear and (b) is an inclined wear. Profiles in figures 1.9(c-e) have several wear segments without any privilege direction. The wear profile in (d) is due to bad sliding quality of the pantograph.

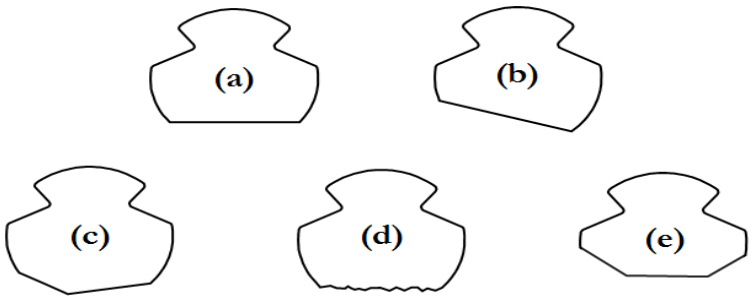

Figure 1.9: Different profiles of contact wire wear. (a-b) are simple wears, (c-e) are complex wears.

1.1.1.5 EMA limit

EMA ("Epaisseur Minimale Admissible" in French) is the acceptable minimum thickness that requires quick intervention for the wire replacement program on the SNCF's network. The EMA values are defined by the SNCF for different wire types that are shown in table 1.1. Whenever the remaining thickness T_{cw} is lower than the EMA, the contact wire has to be replaced.

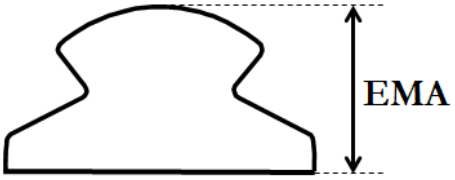

Figure 1.10: Contact wire EMA limit.

However, the thickness is not a relevant feature to estimate the wear degree of the contact wire in all cases. Therefore, it is important to develop a new measurement tool that determines the cross-section area (CSA) of the contact wire over its life-cycle. Accurate and periodical measure of the contact wire cross-section is required by the wire maintenance and repair/replacement planning. When the remaining cross-section of the wire is less than 70% of the original cross-section, the contact wire is considered as being in a critical condition and therefore, must be replaced.

1.1.2 CWWMS Specifications

The Contact Wire Wear Measurement System (CWWMS) using computer vision has to provide the CSA of wires by respecting the following specifications:

- Operating condition: The OCS scene contains different elements such as the catenary wires, droppers, clamps, contact wires etc. Generally, there are two contact wires that move across the measurement area described in figure 1.4, but can be up to four contact wires. Therefore, it is very important to locate the wires so that cameras are focused on the inspected wires. One must also ensure that the spatial resolution at the contact wire surface is fixed in the acquired image. The vision system must also be able to inspect the contact wire in outdoor conditions under sunlight, fog and moderate rain.

- Surface aspect and wear profile: The CSA provided by the system has to be robust against the surface aspect (see figure 1.6) and the wear profile of the contact wire (see figure 1.9).

- Acquisition rate: The measurement system is located on a train moving at 120km/h, which will allow it to be inserted and scheduled in regular commercial train circulation. The CSA has to be measured at every 15mm along the wire at maximum train speed.

- Accuracy: The CSA of the inspected contact wires has to be estimated with Root Mean Square Error (RMSE) that is lower than 3.0 mm^2, for 95% of measurements. The measurement results must also be repeatable. The parameters of acquisition device must be set-up to respect the desired spatial resolution, that will contribute to the accuracy of the measurement system.

1.2 State-of-the-art on CWWMS

The introduction of computer vision has allowed easier means of inspecting the contact wires. The first Contact Wire Wear Measurement System (CWWMS) is based on manual video analysis [70], where the images of the wire scene are acquired using video cameras. Then they are visually classified into satisfactorily, or non-satisfactorily categories on-board. Images that are classified as non-satisfactorily are later cross checked manually by the inspector who will then issue maintenance instructions. Although visual analysis saves lots of time compare to manual measurement, the main problem is the low image resolution. Therefore, it is difficult to identify contact wire wear from viewing the acquired videos.

In this section, we make brief state of art review on existing CWWMS. For simplicity, we regroup these systems into the three following categories,

- Shadowgraphy,
- Single view,
- Multiple view.

The systems that fall into the same category follow the same working principle with slight differences about technological choice. For each category, we review their system illumination, optical set-up, measurement principle, accuracy, and drawbacks.

1.2.1 Shadowgraphy

The CWWMS based on the shadowgraphy principle [59] generally consists of a laser emitter at one end, and a receiver sensor at the other end of the system. The laser emitter scans the contact wire located on its path, so that any signal loss perceived by the receiver sensor is interpreted to determine the contact wire thickness.

1.2.1.1 EPFC System

The EPFC system deployed by SNCF is based on shadowgraphy principle. The system is generally mounted on the pantograph and placed directly close to the contact wire as shown in figure 1.11.

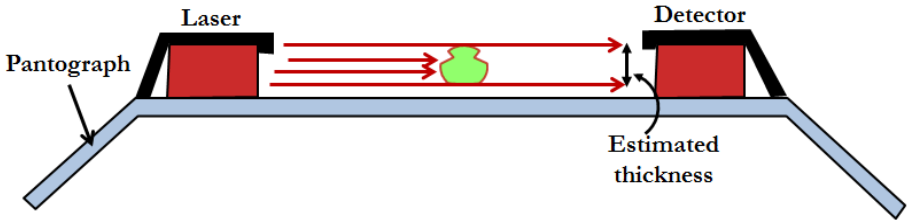

Figure 1.11: Shadowgraphy measurement system.

The wire thickness is estimated thanks to the number of receiver sensor elements that capture the laser signal. A mechanical unit ensures that the contact wires to be measured are well placed and aligned between the laser and detector devices. The system can measure up to two contact wires with maximum train speed of 25km/h.

However, it is difficult to reach a perfect alignment of the contact wire especially in the case of inclined and complex wear profiles (see example in figure 1.12). So, the thickness of badly aligned contact wire is not accurately estimated by shadowgraphy. SNCF has been working on different projects over the years to improve the mechanical alignment of the wires before measurements.

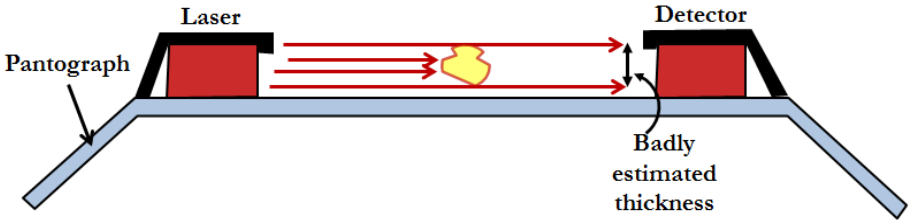

Figure 1.12: Shadowgraphy measurement drawback.

1.2.2 Single View

The single view systems are based on Specular Reflection Technique (SRT). It requires that a camera (line scan or area scan) observes an object illuminated by light source (lamps, lasers etc). The goal of SRT is to provide an output image that exhibits the high specular surface properties of the object to be inspected (see figure 1.13). SRT assumes that the wear track is characterized by its metallic aspect so that the lighting choice and the system set-up should ensure that the grey-levels of the pixels representing the wear track are higher than those of the background pixels.

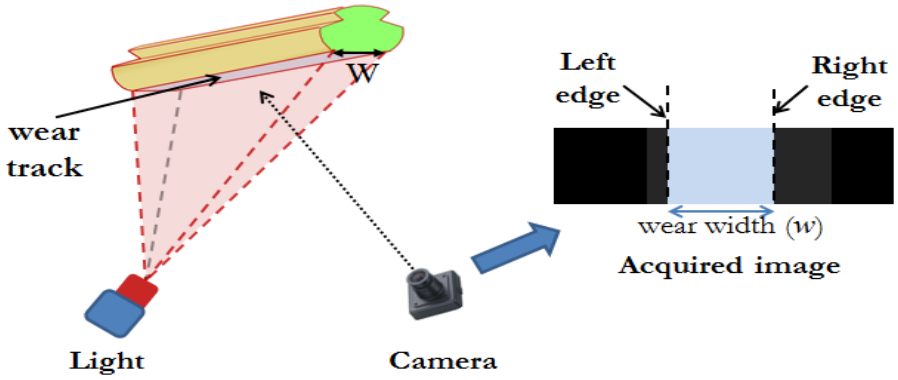

Figure 1.13: Single view system under specular reflection technique.

The left and right edges in the acquired image are determined using edge detection methods,

and then used to estimate the wear width w in pixels. Thanks to a calibration step (i.e. function relation between pixel and mm), the wear width w in the image is transformed to its metric value W (mm). Finally, the wire cross-section area or thickness is determined from W using some geometrical wire models. The performance reached by this technique strongly depends on aspect of the wear track, so that the light is homogeneously reflected by the wear track to the camera.

1.2.2.1 Doctor Yellow

Doctor yellow is a multipurpose inspection train that has been used on the Japanese railway network for a very long time. The first wear measurement system proposed by Kamiya et al. [2] consists of sodium vapour lamp that illuminates the contact wire. The wire is then observed by area scan camera whose location is adjusted according to the height of the wire by means of moving mirrors. Further upgrades to the system over the years are explained in the following papers [31, 48, 94].

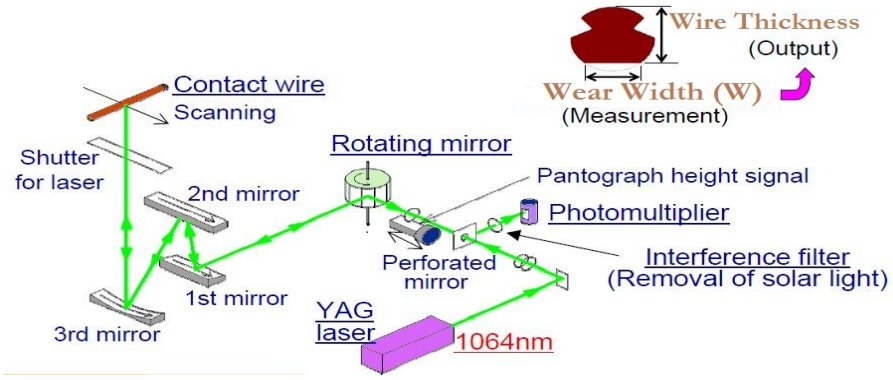

Figure 1.14: Description of system installed on Doctor Yellow [47].

In the updated system version presented by Kusumi et al. [47] (see figure 1.14), the authors used a line scan camera with a photo multiplier to acquire image of contact wire illuminated by a YAG laser. The line scan camera acquires the image with higher spatial resolution compared to area scan cameras used by earlier version of the system. The laser power has to be greater than 5W since the system is located on the roof of the train. As it is required that the spatial resolution of contact wire in the acquired image should be constant, the system thus includes a separate control unit that determines the contact wire's location needed to regulate the mirror's position. The spatial measurement sampling is 70mm for a train moving at maximum speed of 270km/h.

There is no information about the measurement accuracy, but the system can measure the thickness of up to four contact wires simultaneously [91]. An older version of the system was tested by SNCF few years ago and the main conclusion was that Japanese systems are generally very hard to operate, which means they require experts for their maintenance.

1.2.2.2 MEDES System [8]

This system was proposed by Borromeo et al. [8], and located inside the train but not very far from the pantograph. The system component contains six blocks, each block has a line scan camera, a small size LED laser diode and a mirror targeted to the location of the contact wire (see figure 1.15). The system includes a wavelength filter in front of the camera lens to eliminate sunlight effect during the day. The distance between the contact wire and camera is regulated by a PID (proportional-integral derivative) controller to position the cameras so that the spatial resolution does not change with respect to contact wire position. The system measures the wire worn-out area from the determination of wear width in the image, and provides measurements at every 150mm for maximum train speed of 120km/h.

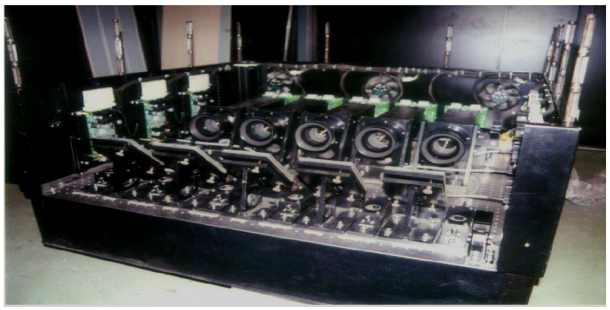

Figure 1.15: MEDES system block arrangement [8].

The system has been installed on SNCF trains, and tested on different samples of the contact wires. The system provides good results on wires with simple wear profiles, both for round and oval wires. However, it cannot measure precisely the contact wires with complex wear profiles. The main advantage is that the system is cheaper and easier to maintain compared to Dr. yellow [47] and ATON systems [28, 83].

1.2.2.3 Meidensha System [86]

Meidensha system (also known as Catenary eye) that uses a LED laser, combined with line scan camera has two main units. The first unit determines the contact wire height, while the second unit estimates its thickness. The contact wire height determination has been performed using two computer vision methods: (1) formerly with the use of marker placed on the pantograph and (2) recently with stereo vision set-up using two line scan cameras. Thanks to the determination of contact wire height, the images are rectified so that the spatial resolution in the acquired images is constant. This ensures that a pixel corresponds to (0.1mm $\times$ 0.1mm) on the wire's surface throughout its location in the measurement area. An example of juxtaposed line-scan images (called spatio-temporal image) provided by the line scan camera is shown in figure 1.16. Assuming that the wire width w for the rectified image is well determined, the thickness of contact wire can then be effectively estimated.

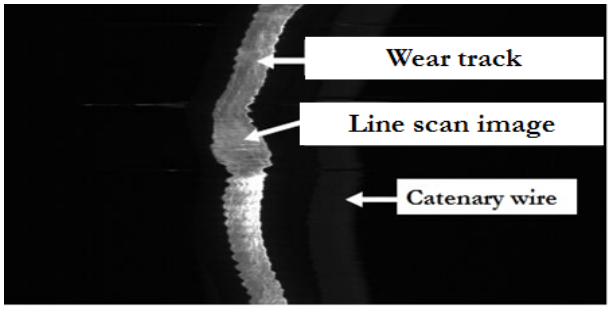

Figure 1.16: An example of juxtaposed line-scan images with Meidensha system [86].

The spatial sampling measurement of the system is 30 mm for maximum train speed of 110km/h. This system has not been tested on the SNCF network, but one can refer to Koshiba [45] for further information.

1.2.2.4 Chugui System [5, 13]

The contact wire is illuminated by a laser, and is observed by an area scan camera according to a specific viewing angle. The laser includes a rotary mirror that produces plane shaped patterns (see figure 1.17). As the spatial location of the wire changes, the author proposed the combination of mirrors, and wire height tracking motor to reach a fixed spatial image resolution, so that one pixel corresponds to 0.3 x $0.3mm^2$ area on the surface of the contact wire.

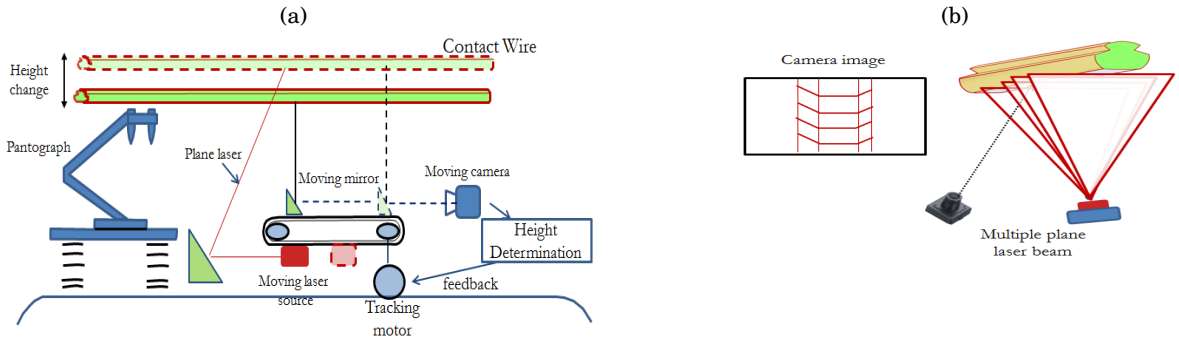

Figure 1.17: Chugui system set-up [13].

The acquired images are analyzed so that the laser stripe center of the projected laser pattern is extracted for each column. The contact wire profile is then determined by linking the obtained stripe centers by a curve (using mean square deviation criteria) directly on the 2D image plane. Finally, the cross-section of the worn-out area is determined by fitting circular arc that passes through the edges of the wear, as shown in figure 1.18.

Experiments were carried out on contact wire samples whose sections are $85mm^2$ and $100mm^2$, and the system can measure up to 4 contact wires. The measurement sampling of the

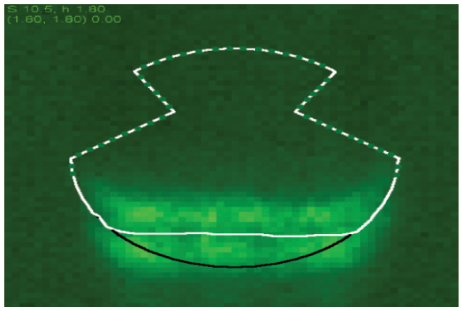

Figure 1.18: Estimated wire profile [42].

system is 10mm for maximum train speed of 60km/h [42]. The authors affirm that the RMSE of the cross-section estimation is $1.5mm^2$. This system has only been tested on simple cases of contact wire wear, and the measurement speed falls below the expectation of SNCF.

As it is difficult to extract contact wire profile from analysis of single view images, other systems acquire several images of the wire according to multiple views. The system based on multiple view will be explained next.

1.2.3 Multiple View

The multiple view systems are also based on the Specular Reflection technique (SRT), which involves illumination of the wear track, followed by an image processing step to estimate the contact wire cross-section or thickness. The main difference from the single view system is the use of two or more cameras that observe the wire with respect to different directions.

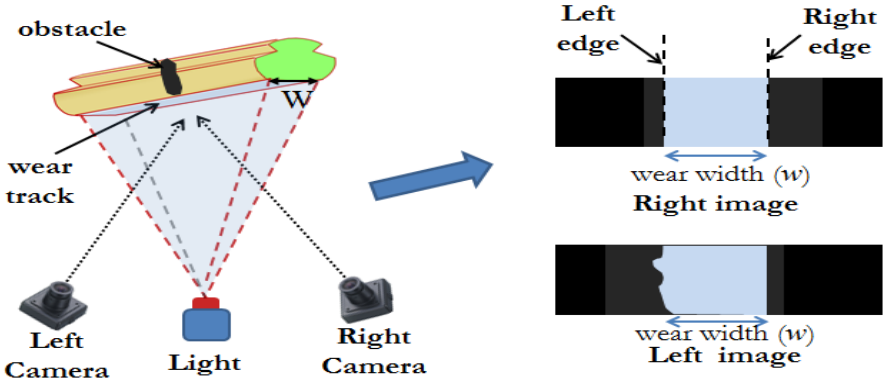

Figure 1.19: Multiple view system.

Figure 1.19 shows an arrangement of a multiple view system with two cameras placed at the left and right side of the contact wire. An obstacle (e.g grease) at the left side of the wire is observed by the left camera. The occlusion from this obstacle impacts wear width estimation from the left camera needed to determine the thickness or cross-section. Thanks to multiple

view set-up, one can then compensate for this problem by using only the image acquired by the right camera. This is done thanks to comparison between the accuracy of wear width extraction provided by the analysis of left and right images.

1.2.3.1 Siemens System [75]

This system was developed to deal with possible grease deposit at one side of the contact wire [75]. Two line scan cameras and infrared laser diodes (15W) were placed on the roof of the measurement train. The cameras are not placed vertically facing the sky in order to prevent direct sunlight effect, and the optical parameters were setup to get a large depth of field that covers the whole measurement zone whose height is approximately 2000mm in figure 1.20a.

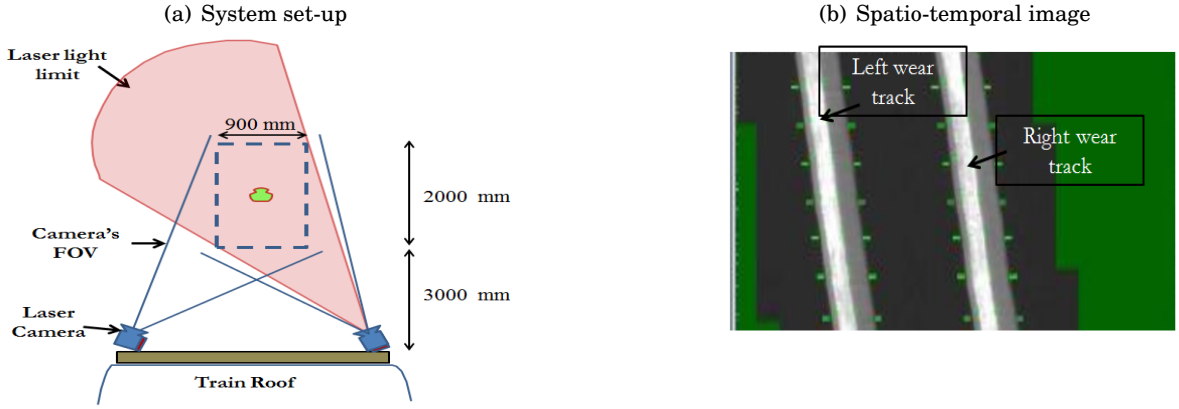

Figure 1.20: Illustration of the Siemens system.

The system uses Chirped Laser Radar technique [76] to determine the wire location, which is then used to rectify the acquired wire images regardless of the distance between wire and camera. Both line scan cameras acquire images at every 100mm for maximum train speed of 120 km/h in order to create a spatio-temporal image shown in figure 1.20b. The overall system suitability for operation in a railway environment was proved by continuous rail tests in 2001 on German railway network [10, 20].

One of the system main drawbacks is the use of high laser power to illuminate the contact wire. This poses high security risk to the railway workers and passengers. SNCF has bought this system in the past, and the main conclusion is that the system only reaches satisfying performances for contact wires with homogeneous surface aspect, and simple wears.

1.2.3.2 WWS System (Fraunhofer) [39]

The Wire Wear monitoring System (WWS) is composed of (a) Contact wire Recording System (CRS) that determines the contact wire spatial location using optical radar techniques [30] and (b) a sub-system that measures the thickness of the contact wire using Specular Reflection Technique

[39]. To measure the wire thickness, the authors use two independent blocks containing the laser and camera (see figure 1.21). Thanks to CRS, each block is targeted to the contact wire using galvanometric scanning mirrors and a motorized objective lens. The acquired images are then processed to extract the wear width needed to estimate the contact wire thickness.

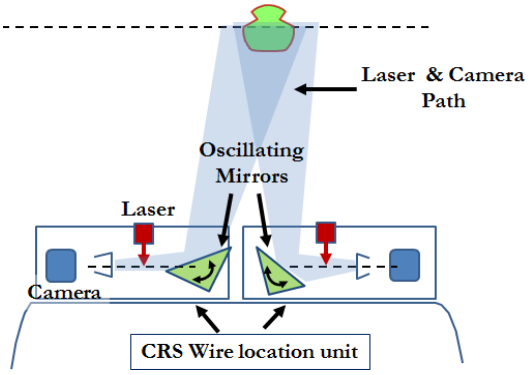

Figure 1.21: WWS measurement system set-up.

The system can measure up to four contact wires, which means each block has the possibility of measuring two wires simultaneously. The system was installed on a train moving at a maximum speed of 160km/h with measurement sampling of 50mm. The test run was done on both Italian and Finland railway networks, but no information about the measurement accuracy is provided.

1.2.3.3 OPTEL System [26]

This system uses two area scan cameras and lasers (power ≈ 1watt) that were placed as shown in figure 1.22. The optical axes of the two cameras are perfectly parallel, which indeed form a stereo vision set-up. The illuminated wear track is projected to the images of both the left and right cameras. The acquired images are filtered to remove noise. The wear width is determined by the analysis of both images.

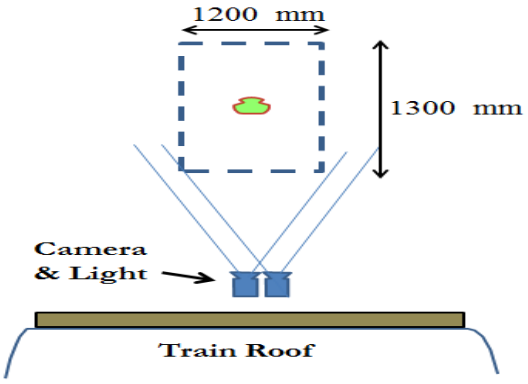

Figure 1.22: Optel measurement System.

The authors proposed a geometrical wire model based on triangle similarity properties to determine the parameters that can be used to characterize the contact wire. The parameters include vertical and horizontal distance, wear width, and thickness in mm [26, 27]. The system can measure up to two contact wires for a train moving at maximum speed of 80km/h. The system has only been tested on moderately inclined wear, and simple wear profiles. There is no detail information about the system location, and the measurement accuracy.

1.2.4 Conclusion

SNCF has made experiments between 2001 and 2009 using most of the CWWMS described in this section. Only the systems in section 1.2.2.4 and 1.2.3.3 have not been tested. The integrity of each system has been evaluated using the repeatability and reproducibility of the CSA measurement of certain challenging test rail stretch on SNCF network. The conclusion from these experiments is that the EPFC system is the most reliable system but only when the contact wires are well aligned before measurement. This has motivated SNCF over the years to improve mechanical alignment unit of the EPFC system, especially for highly inclined wires.

Among the single and multiple view systems, MEDES has provided the most acceptable measurement results on the challenging test rail stretch. It is the only method that succeeds in measuring correctly the CSA of oval wires. The most common problem with single and multiple view systems is that they are susceptible to produce incomprehensible results. Therefore, one is required to regularly verify their measurements. For example, whenever the wire or wear is highly inclined, the wear track may not reflect the light back toward the cameras as expected. As a consequence, only the light reflected from only one of the wear edges (see figure 1.19) is really captured by the cameras, and the system thus concludes that the wear width is lower (thinner) than it really is.

In this section, we have shown that the use of machine vision techniques is very important for contact wire wear measurement. A few vision systems have provided satisfying results but still lack reliability. The measurements provided by these systems are mainly issued from 2D image processing. Indeed, the methods only analyze projection of contact wire's wear track on a plane sensor, and neglect their 3D profile. Therefore, 3D reconstruction of the contact wire profile using multiple view should be relevant to avoid the drawbacks of existing systems. The use of 3D methods will provide richer information of the scene needed for accurate contact wire CSA estimation.

1.3 Camescat Project

The CaMeSCat (Capteur de Mesure de la Section Catenaire "Catenary Section Measurement System") is a research and innovation project. The aim is to bring together panel of experts which include industries and public research laboratories in order to design an embedded system that measures the cross-section of contact wires. It must be able to make measures in outdoor conditions, and at minimum speed of 120km/h to ensure its placement in proper commercial train circulation. The developed system will be used for preventive maintenance of the railway overhead contact system.

This PhD. thesis is achieved under the Camescat project between SNCF (French Railway Company) and CRISTAL laboratory of Lille1 University. The thesis is financed under CIFRE (Conventions Industrielles de Formation par la REcherche) convention, as well as the FUI (inter ministry fund) project of the Nord-Pas-De-Calais region.

1.3.1 Thesis Contributions

The single state of art review about contact wire wear measurement systems was written by Muller et al. [67] before 2000. Therefore, we have made a complete state of art study on recent measurement systems. Our study shows that the CSA of contact wires is approximated from the wear width that has been estimated thanks to analysis of 2D images. Therefore, one can avoid this limitation thanks to estimation of the contact wire profile using 3D vision techniques. For this purpose, a 3D measurement system that is based on laser triangulation is proposed. The system is made up of laser planes and cameras.

Note : Due to intellectual property right and confidentiality of the Camescat project, some sensitive issues about the camera and laser placements as well as their technological choices are omitted in this PhD report.

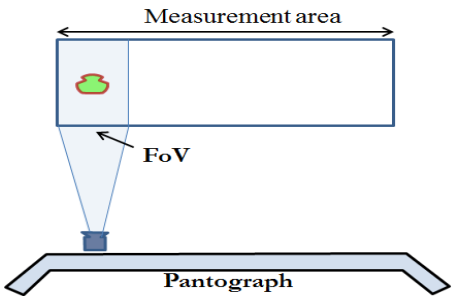

Figure 1.23: System placement problem.

The camera and laser have been placed on a mechanized pantograph to coarsely maintain constant distance from the contact wire, and has also been set-up in order to respect the spatial

resolution required to accurately inspect the contact wire (see figure 1.23). With this set-up, one will need to use a high number of cameras and lasers to cover the whole measurement area. However, the weight of the acquisition device put on the pantograph has to be limited, notably for security purposes. To decrease the number of cameras and lasers, we have used a Scheimpflug optical set-up that increases the camera's field of view, while decreasing its depth of field [18]. The sensor plane is tilted according to an angle θ with reference to the optical axis, thanks to the Scheimpflug lens (see figure 1.24).

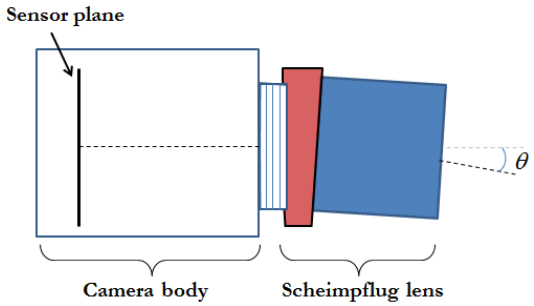

Figure 1.24: Scheimpflug device.

System calibration

To perform dimensional measurement of the contact wire, the laser-camera triangulation system has to be calibrated. For intrinsic camera calibration, we model the formation of an image acquired by a Scheimpflug device. Then, we propose two intrinsic calibration methods using bundle adjustment technique. The proposed methods are tested on real calibration images, and these experiments have shown that our approaches provide better accuracy than classical calibration methods.

The laser-Scheimpflug device has been calibrated with a new pattern. This is a calibration method that requires just a single image of the laser calibration pattern. The pattern has been particularly proposed to suit with the project requirements in terms of security. Once the system has been calibrated, images of laser projection on the contact wire surface are analyzed to measure the contact wire cross-section area.

Cross-section determination by 3D analysis

We first propose a laser stripe extraction technique to locate the center pixels that correspond to the laser projected on the contact wire. Thanks to laser-camera calibration, we transform these pixels to reconstructed 3D points using triangulation technique.

Finally, we develop an algorithm to determine the CSA of different contact wire profiles directly from the reconstructed 3D points. The proposed method combines shape modeling, and

pattern recognition. The performance of the proposed system has been assessed using both simulated, and real datas.

1.3.2 Manuscript Organization

After this general introduction that includes the state of art review on Contact Wire Wear Measurement System, the rest of this PhD thesis manuscript is organized as follows:

Chapter 2 describes our calibration method of the proposed laser-camera triangulation system. The used cameras have been equipped with a Scheimpflug lens. We first recall essential background equation for pinhole image formation, then propose a slight adjustment in the model to formulate tilted image, which is called Scheimpflug image formation model. Next, we propose calibration methods for the Scheimpflug device in order to extract the intrinsic camera parameters. Thanks to the proposed intrinsic calibration procedure, we can then effectively calibrate the whole laser-camera triangulation system. The proposed method has been evaluated and deemed suitable for industrial application.

Chapter 3 presents the thesis contribution that is required for cross-section estimation of the contact wire. It is divided into two successive steps, the profile determination, and the profile analysis. The profile determination starts from accurate extraction of the pixels that correspond to center of the laser stripe projected on the contact wire. Next, the pixels are transformed to reconstructed 3D points, thanks to the system calibration. These reconstructed 3D points are analyzed to determine the cross-section area using shape analysis methods.

Chapter 4 presents various experiments that have been carried out to verify the capability of the proposed contact wire wear measurement system. Indeed, the experiments allow us to validate the whole system chain from calibration to cross-section estimation. The system prototype has been tested on both plug gauge and real contact wire samples. The experimental results have allowed further improvements on final real system conception.

Chapter 5 summarizes the PhD thesis contributions, with few discussions about the performance reached by the system. Various issues regarding the system, and future perspective of the PhD thesis are then detailed.

CHAPTER 2

SYSTEM CALIBRATION

Active 3D reconstruction is one of the artificial vision techniques for generating dense 3D points of an observed object. In our case, it involves the use of a laser plane that intersects the measured object, so that its shape is captured by a 2D camera (see figure 2.1). A ray passing through the camera's optical center O_c is guaranteed to intersect the laser plane at 3D point P_w only if both the ray and laser planes are not parallel in 3D space [80]. So, point P_w is projected to a pixel p in the image plane. Once the homography between image and laser planes has been determined, we can estimate the 3D coordinates of P_w from the spatial coordinates of its associated pixel p in the image by triangulation.

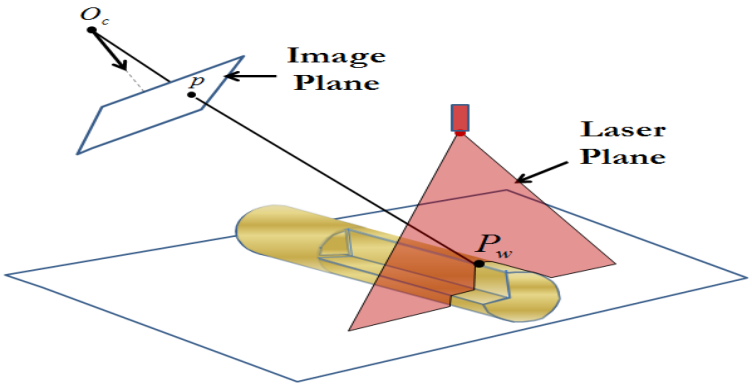

Figure 2.1: 3D laser scanner.

In the following, we introduce the term "line profile", which is the intersection between the laser plane and the object in the scene. In order to determine the 3D coordinates of the line profile from the acquired 2D images (i.e. 3D profile), one needs to first determine the camera's intrinsic parameters, followed by the laser plane position in the calibrated camera coordinate system.

In this chapter, we first detail the image formation model under Scheimpflug set-up. Then, we propose two methods that calibrate a camera equipped with a Scheimpflug lens (Scheimpflug device). Finally, we determine the laser plane position in the calibrated camera coordinate system.

2.1 Image Formation Model

In this section, we give background equations on classical image formation using pinhole model. Next, we explain the Scheimpflug image formation model, and the optical lens distortion.

2.1.1 Pinhole Formation Model

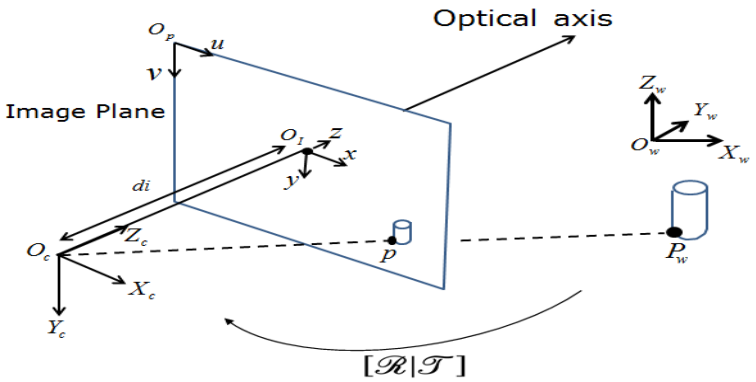

Figure 2.2: Image formation under Pin-hole model.

The pinhole formation model describes the mathematical relationship between the coordinates of a 3D point and its projection onto the image plane of an ideal pinhole camera ($\mathbb{R}^3 \implies \mathbb{R}^2$). In such a case, the internal geometry, the position and the orientation of a camera in the scene are modeled. The simplest image formation using pinhole model is proposed by Hall et al. [33] (see figure 2.2). Various parameters are presented in the following:

- The world coordinate system, $(O_w[X_w, Y_w, Z_w])_w$,
- The camera coordinate system, $(O_c[X_c, Y_c, Z_c])_c$, where O_c is the optical center and Z_c corresponds to the optical axis,
- The optical axis intersects the image plane at O_I called the principal point, with image plane coordinate system $(O_I[x, y, z = 0])_I$, $\|O_c O_I\| = di$ is fixed under pinhole model,
- The pixel coordinate system, $(O_p[u, v])_p$.

Using homogeneous coordinates, and assuming pinhole model with no geometric distortion, a 3D world point $P_w(X_w, Y_w, Z_w)_w$ is projected onto the image pixel $p(u, v)_p$ using a projection matrix $\mathscr{A}$ as shown below,

$$\lambda \begin{bmatrix} u \\ v \\ 1 \end{bmatrix} = \mathscr{A} \begin{bmatrix} X_w \\ Y_w \\ Z_w \\ 1 \end{bmatrix} \quad \text{where } \mathscr{A} = \mathscr{K}[\mathscr{R} \mid \mathscr{T}] \tag{2.1}$$

In equation (2.1), λ is a scaling factor on both u and v axes. The projection matrix $\mathscr{A}$ has been decomposed intro intrinsic $\mathscr{K}$ and extrinsic $[\mathscr{R} \mid \mathscr{T}]$ matrices. The intrinsic matrix models the internal geometry and optical characteristics of the image sensor, while the extrinsic matrices $[\mathscr{R} \mid \mathscr{T}]$ measure the position of the optical center, and the orientation of the camera with respect to the world coordinate system.

2.1.1.1 Extrinsic Parameters

To obtain the camera coordinate point $P_c(X_c, Y_c, Z_c)_c$ from a point $P_w(X_w, Y_w, Z_w)_w$ in the 3D world coordinate, the camera should first be translated to the world coordinate origin and then be rotated. With perspective projection using homogeneous coordinates, this can be written together in a combined matrix notation as,

$$\begin{bmatrix} X_c \\ Y_c \\ Z_c \end{bmatrix} = [\mathscr{R}|\mathscr{T}] \begin{bmatrix} X_w \\ Y_w \\ Z_w \\ 1 \end{bmatrix}, \quad \text{where} \quad \mathscr{R} = \begin{bmatrix} r_{11} & r_{12} & r_{13} \\ r_{21} & r_{22} & r_{23} \\ r_{31} & r_{32} & r_{33} \end{bmatrix} \quad \text{and} \quad \mathscr{T} = \begin{bmatrix} t_x \\ t_y \\ t_z \end{bmatrix} \tag{2.2}$$

The rotation matrix $\mathscr{R}$ is "3x3" in dimension, and is parametrized by Euler angle rotations around the X_w, Y_w and Z_w axes respectively.

2.1.1.2 Intrinsic Parameters

We consider a camera with the optical axis that is collinear to the Z_c axis and whose optical center is located at the origin O_c of the camera coordinate system, so that the lens plane is $(O_c[X_c, Y_c, Z_c = 0])_c$. A 3D point $P_c(X_c, Y_c, Z_c)_c$ in the camera coordinate system is expressed in the image coordinate system, assuming no distortion as:

$$\begin{aligned} x &= di\frac{X_c}{\lambda}, \\ y &= di\frac{Y_c}{\lambda}, \end{aligned} \tag{2.3}$$

where λ=Z_c is the homogeneous scaling factor. The matrix notation of equation (2.3) can then be written as follows,

$$\lambda \begin{bmatrix} x \\ y \\ 1 \end{bmatrix} = \begin{bmatrix} di & 0 & 0 \\ 0 & di & 0 \\ 0 & 0 & 1 \end{bmatrix} \begin{bmatrix} X_c \\ Y_c \\ Z_c \end{bmatrix}, \text{where } \mathcal{K}_{di} = \begin{bmatrix} di & 0 & 0 \\ 0 & di & 0 \\ 0 & 0 & 1 \end{bmatrix} \tag{2.4}$$

Let us define the principal point O_I in the pixel coordinate system as $O_p(u_0, v_0)_p$. We can easily transform points in image coordinate $(x, y, z)_I$ to their pixel location $(u, v)_p$. We should note that the pixels of the image sensors are not necessarily square, and can also be skewed. These characteristics of the imaging system can be taken into account by the camera model thanks to two additional parameters "a" and "sk" which model the pixel aspect ratio, and skewness respectively. The intrinsic matrix that directly maps camera coordinates to pixel coordinates "under pinhole" can now be written as shown below,

$$\begin{aligned} \lambda \begin{bmatrix} u \\ v \\ 1 \end{bmatrix} &= \begin{bmatrix} \frac{di}{s_x} & sk & u_0 \\ 0 & a\frac{di}{s_y} & v_0 \\ 0 & 0 & 1 \end{bmatrix} \begin{bmatrix} X_c \\ Y_c \\ Z_c \end{bmatrix} \\ \text{where } \mathcal{K} &= \begin{bmatrix} f_x \equiv \frac{di}{s_x} & sk & u_0 \\ 0 & f_y \equiv a\frac{di}{s_y} & v_0 \\ 0 & 0 & 1 \end{bmatrix} \end{aligned} \tag{2.5}$$

$f_x \equiv \frac{di}{s_x}$, $f_y \equiv a\frac{di}{s_y}$ are the focal lengths on both u and v axes, s_x and s_y are the pixel sizes. We should also note that the camera skew parameter sk is very close to zero and may be neglected.

Note: Under pinhole model, the focal length f is the same as di, and it is fixed. Therefore, we can write focal lengths on both u and $v-$axis as $f_x \equiv \frac{di}{s_x}$, and $f_y \equiv a\frac{di}{s_y}$ respectively.

2.1.2 Scheimpflug Formation Model

2.1.2.1 Introduction

For any camera to be in perfect focus, the object to be measured has to be placed in a planar surface that is parallel to the image plane. However, having a sharp image can be very difficult when this object moves along an oblique plane to the camera. An example is shown in figure 2.3 where the object plane is located at an oblique angle to the camera. This is the case when one is interested in capturing a very large object such as the facade of a tall building, or a decorative cobblestone pathway. The camera is required to be aimed upward at an angle which makes it difficult to bring the complete object of interest in focus all along the object plane.

In order to bring the object in focus along the object plane in the camera's Field Of View (FOV), one needs to decrease the relative aperture (increase the f-number) of the lens. However, this solution limits the amount of light reaching the sensor, which leads to poor grey-level dynamic in

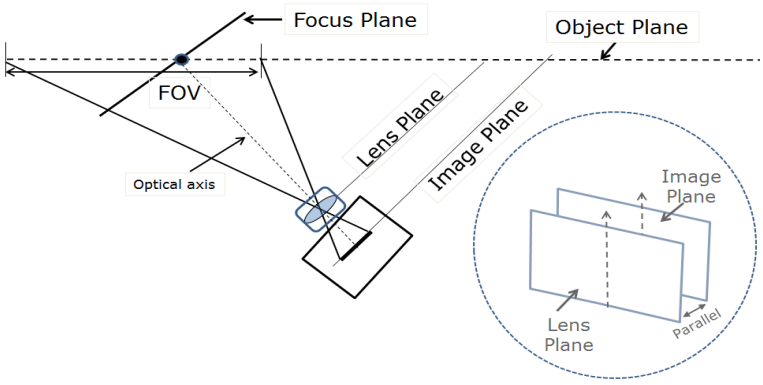

Figure 2.3: Conventional camera set-up.

the image. One way of escaping this dilemma is to use the "Scheimpflug's principle" [18, 64]. This principle calls for three planes to intersect in a common line:

- The object plane containing the observed objects, and oblique to the lens plane,
- The lens plane,
- The image plane that is tilted at given angles θ, γ to intersect with the two other planes.

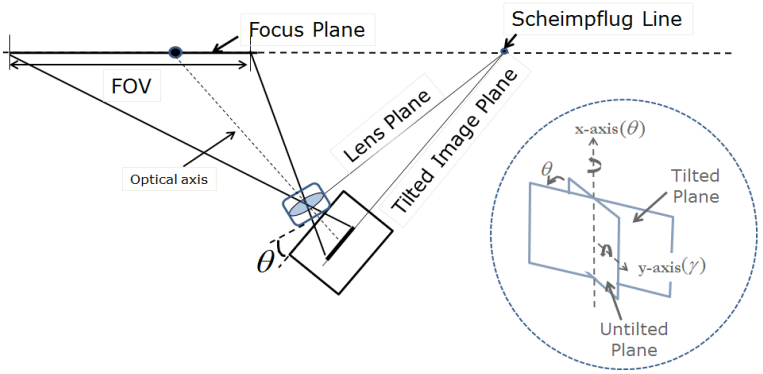

Figure 2.4: Scheimpflug device set-up.

This line of intersection between these three planes is known as the "Scheimpflug line" (see figure 2.4). In this new set-up, the camera focus plane coincides with the object plane which allows us to obtain a sharp camera's field of view that is wide enough to perform 3D dimensional measurement. Scheimpflug principle is employed for Particle Image Velocimetry (PIV) applications [3, 106].

For conventional cameras under pinhole model, the image plane is usually parallel to the lens plane $(O_c, [X_c, Y_c, Z_c])_c$. In Scheimpflug set-up, the image plane is tilted at given angles θ and γ,

(called Scheimpflug angles) around the axis parallel to the X_c, Y_c but in O_I (see figures 2.4 and 2.5). This adjustment ensures that the image plane, the lens plane and the object focus plane intersect at a line parallel to X_c axis, denoted as "Scheimpflug line".

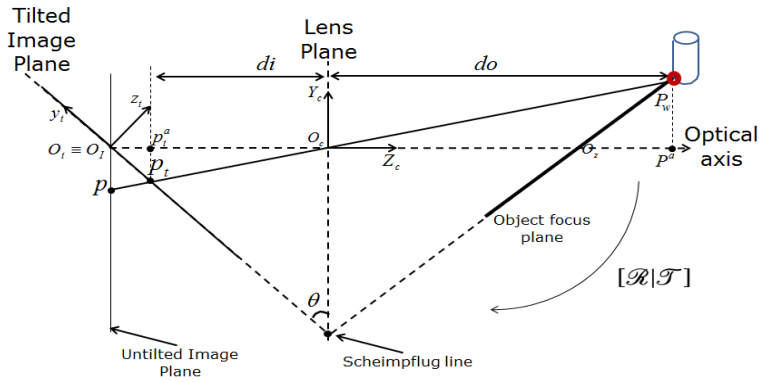

Figure 2.5: Scheimpflug camera model illustration.

For a point P_w along the object focus plane (see figure 2.5), lets denote the image distance $di = \|\overrightarrow{O_c\ p_t^a}\|$ and object distance $do = \|\overrightarrow{O_c\ P^a}\|$ from center of the lens along the optical axis, where p_t^a and P^a are the projections of p_t and P_w to the optical axis. The thin lens equation still hold for Schiempflug set-up so that $\frac{1}{f} = \frac{1}{do} + \frac{1}{di}$. This is possible for any projected points on the tilted image plane from the object focus plane.

We distinguish the following coordinate systems:

- The untilted image coordinate system,$(O_I[x,y,z])_I$, where $z = 0$ for each point on the untilted image plane (Normalized)
- The tilted image coordinate system $(O_t \equiv O_I[x_t,y_t,z_t])_t$, where $z_t = 0$ for each point on the tilted image plane (Normalized)
- The untilted pixel coordinate system $(O_p[u,v])_p$,
- The tilted pixel coordinate system, $(O_p[u_t,v_t])_p$

In order to determine the 3D coordinates of world point P_w from its projected point p_t in the tilted image plane, we need to calibrate the used camera. However, camera calibration methods under pinhole model cannot be used for Scheimpflug device. So we extend the pinhole formation model to take into account Scheimpflug angles. We propose a Schiempflug image formation based on pinhole model assumption.

2.1.2.2 Image Formation Model

Assuming no optical distortion (see section 2.1.1), an object point $P_w(X_w,Y_w,Z_w,1)_w$ is first projected to the point $p(x,y,0,1)_I$ in the untilted image plane as

$$\lambda\ p = \mathcal{K}_{di}[\mathcal{R} \mid \mathcal{T}]\ P_w \tag{2.6}$$

Now, let us model the image formation on the tilted image plane. A ray passing through the optical center O_c of the camera intersects the tilted plane at $p_t(x_t, y_t, 0)_t$ and the untilted one at $p(x, y, 0)_I$ respectively. Without abuse of notations, we represent the point $p_t(x_t, y_t, 0)_t$ in the tilted image plane as $p_c^t(X_c, Y_c, Z_c)_c$ in the camera coordinate system. Likewise, point $p(x, y, 0)_I$ in the untilted image plane is represented as $p_c(X_c, Y_c, Z_c = di)_c$ in the camera coordinate system.

Therefore, the untilted camera coordinate points $p_c(X_c, Y_c, Z_c = di)_c$ can be related to the untilted image coordinate points $p(x, y, 0)_I$ as,

$$\begin{aligned} X_c &= x \\ Y_c &= y \\ Z_c &= di \end{aligned} \tag{2.7}$$

We first apply a projective transformation represented by matrix $\mathcal{K}_c^t$ that transforms point $p_c(X_c, Y_c, di)_c$ to $p_c^t(X_c, Y_c, Z_c)_c$ as shown below (see appendix 7.1.1 for $\mathcal{K}_c^t$ matrix formulation):

$$p_c^t = \mathcal{K}_c^t p_c,$$

$$\text{where } \mathcal{K}_c^t = \begin{bmatrix} di & 0 & 0 \\ 0 & di & 0 \\ 0 & 0 & di \\ tan\ \gamma & -\frac{tan\ \theta}{cos\ \gamma} & 1 \end{bmatrix} \tag{2.8}$$

Then we express point $p_c^t(X_c, Y_c, Z_c)_c$ in the camera coordinate to their point $p_t(x_t, y_t, 0)_t$ in the tilted image plane. This is done by applying combined rotation matrix $\mathcal{R}_s$ with respect to the OX-axis parametrized by angle θ, and OY-axis parametrized by angle γ respectively. The rotation matrix $\mathcal{R}_s$ is preceded by a translation vector $\mathcal{T}_s$ (from O_c to O_I) (See appendix 7.1.2). Finally, $\mathcal{K}_s$ matrix is expressed as below,

$$\lambda\ \mathrm{p}_t = \mathcal{K}_s \mathrm{p}_c^t,$$

$$\lambda\ \mathrm{p}_t = \begin{bmatrix} cos\ \gamma & 0 & -sin\ \gamma & di\ sin\ \gamma \\ sin\ \gamma\ sin\ \theta & cos\ \theta & cos\ \gamma\ sin\ \theta & -di\ cos\ \gamma\ sin\ \theta \\ sin\ \gamma\ cos\ \theta & -sin\ \theta & cos\ \gamma\ cos\ \theta & -di\ cos\ \gamma\ cos\ \theta \\ 0 & 0 & 0 & 1 \end{bmatrix} \mathrm{p}_c^t \tag{2.9}$$

Note that the two steps described earlier complete the Scheimpflug image formation ("Intrinsic formation"). Hence, the point $p_t(x_t, y_t, 0)_t$ on the tilted image plane is deduced from $p_c(X_c, Y_c, di)_c$ in the camera coordinate system as below

(2.10) $$\lambda p_t = \mathcal{K}_s \mathcal{K}_c^t p_c$$

A final conversion in pixel coordinates is effected with $\mathcal{K}_b$ matrix where s_x, s_y are the pixel sizes and (u_0, v_0) are the principal point coordinates in pixel.

(2.11) $$\mathcal{K}_b = \begin{bmatrix} \frac{1}{s_x} & sk = 0 & u_0 \\ 0 & \frac{1}{s_y} & v_0 \\ 0 & 0 & 1 \end{bmatrix}$$

Here is the full equation that that relates points $p_c(X_c, Y_c, f)_c$ to $p_t(u_t, v_t)_p$ in pixel coordinates:

(2.12) $$\lambda p_t = \mathcal{K}_b \mathcal{K}_s \mathcal{K}_c^t p_c$$

Finally, to obtain $p_t(u_t, v_t)_p$ from $P_w(X_w, Y_w, Z_w)_w$ under pinhole model assumption, we have to apply successively equations (2.6), and (2.12). Therefore, the full Scheimpflug pinhole model is shown in equation (2.13) and (2.14), respectively. They are formulated based on plane geometries and rotations with the two Scheimpflug angles $\{\theta, \gamma\}$. See appendix 7.1 for full formulation.

(2.13)
$$\begin{bmatrix} X_c \\ Y_c \\ Z_c \end{bmatrix} = \begin{bmatrix} r_{11} & r_{12} & r_{13} & t_x \\ r_{21} & r_{22} & r_{23} & t_y \\ r_{31} & r_{32} & r_{33} & t_z \end{bmatrix} \begin{bmatrix} X_w \\ Y_w \\ Z_w \\ 1 \end{bmatrix}$$
$$\lambda \begin{bmatrix} x \\ y \\ 1 \end{bmatrix} = \begin{bmatrix} d_i & 0 & 0 \\ 0 & d_i & 0 \\ 0 & 0 & 1 \end{bmatrix} \begin{bmatrix} X_c \\ Y_c \\ Z_c \end{bmatrix}$$

(2.14)
$$\lambda \begin{bmatrix} u_t \\ v_t \\ 1 \end{bmatrix} = \mathcal{K}_b \begin{bmatrix} cos\,\gamma & 0 & -sin\,\gamma & di\,sin\,\gamma \\ sin\,\gamma\,sin\,\theta & cos\,\theta & cos\,\gamma\,sin\,\theta & -di\,cos\,\gamma\,sin\,\theta \\ sin\,\gamma\,cos\,\theta & -sin\,\theta & cos\,\gamma\,cos\,\theta & -di\,cos\,\gamma\,cos\,\theta \\ 0 & 0 & 0 & 1 \end{bmatrix} \begin{bmatrix} d_i & 0 & 0 \\ 0 & d_i & 0 \\ 0 & 0 & d_i \\ tan\,\gamma & -\frac{tan\,\theta}{cos\,\gamma} & 1 \end{bmatrix} \begin{bmatrix} x \\ y \\ di \end{bmatrix}$$

2.1.2.3 Optical lens distortion

A real imaging system deviates from pinhole model due to the use of an optical lens. As a result of lens manufacturing process, straight lines in the world imaged through real lenses generally

become curve-like on the image plane. This means that the camera ray does not necessarily intersect at the optical center. This distortion has not been taken into account by the earlier Scheimpflug formation. Therefore, the world point P_w is projected to the distorted point $\tilde{p}_t$ instead of undistorted p_t as shown in figure 2.6.

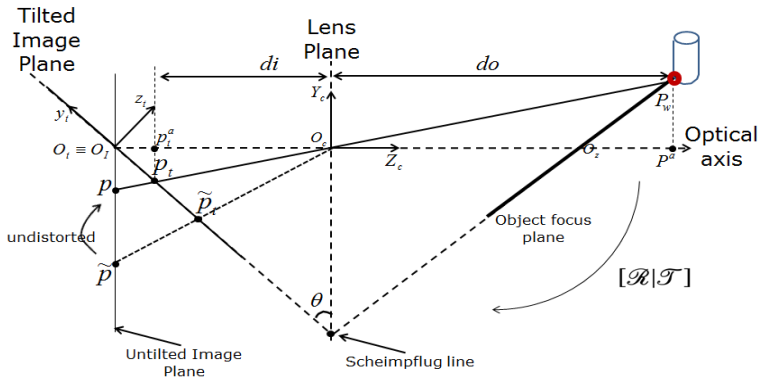

Figure 2.6: Scheimpflug camera model under lens distortion.

The common types of optical distortions are the radial, tangential [9] and thin prism [103]. In practice, radial lens distortion causes straight lines to be mapped as curved lines and appear more visible at the image edges where the radial distance is high. The most common types of radial distortion are (1) barrel that causes the image to bulge toward its center, and (2) pincushion that causes the image to shrink toward the center (see figure 2.7). The tangential distortion is due to the decentering of optical lens, while thin prism is due to the imperfection in lens construction. The thin prism model is generally used for cameras with very large distortions such as fish eye, and mostly neglected in the calibration of conventional cameras [97, 99, 104].

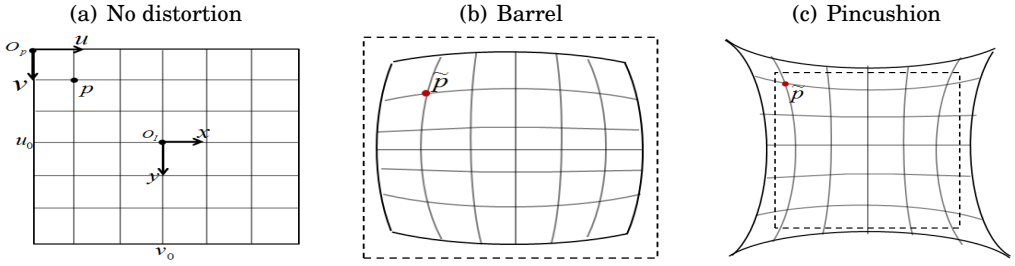

Figure 2.7: Illustration of the optical lens distortion.

As these optical distortions have been caused by the lens, they need to be modeled on the untilted image plane, which is parallel to the lens plane. The relation between distorted pixel $\tilde{p}(\tilde{u},\tilde{v})_p$ and undistorted $p(u,v)_p$ is shown in equation (2.15).

$$\begin{aligned}\tilde{u} &= u + (u-u_0)[k_1r^2 + k_2r^4 + k_3r^6] + [2t_2xy + t_1(r^2+2x^2)] + [s_1r^2] \\ \tilde{v} &= v + (v-v_0)[k_1r^2 + k_2r^4 + k_3r^6] + [2t_1xy + t_2(r^2+2y^2)] + [s_2r^2]\end{aligned} \tag{2.15}$$

where $r = \sqrt{(u-u_0)^2 + (v-v_0)^2}$ is the radial distance from the image center (u_0, v_0), the coefficients (k_1, k_2, k_3) are the radial distortions, (t_1, t_2) are the tangential coefficients, and (s_1, s_2) are the thin prism coefficients, respectively.

These non-linear distortions would be simplified independently from the camera parameters. Thanks to the proposed Scheimpflug model and known Scheimpflug angles, the distorted pixel $\tilde{p}_t(\tilde{u}_t, \tilde{v}_t)_p$ can first be projected back to its untilted pixel $\tilde{p}(\tilde{u}, \tilde{v})_p$ where the distortion coefficients will be determined according to the calibration method. The Scheimpflug calibration procedure under lens distortion will be detailed in section 2.2.

2.2 Intrinsic Camera Calibration

Camera calibration is mostly performed by using 2D planar target or 3D object that contains feature points. Depending on the calibration target, most of the methods use the centers of high contrast circular patterns [38, 43, 63], and corners of square patterns [29, 55, 111]. The feature pixels that correspond to these feature points can easily be identified through methods that combine image processing techniques such as edge detection, thresholding, and sub-pixel estimation. Finally, the projection matrix $\mathscr{A}$ (see equation 2.1) between the 3D coordinate feature points and coordinates of feature pixels in the image plane can be used to extract the camera parameters.

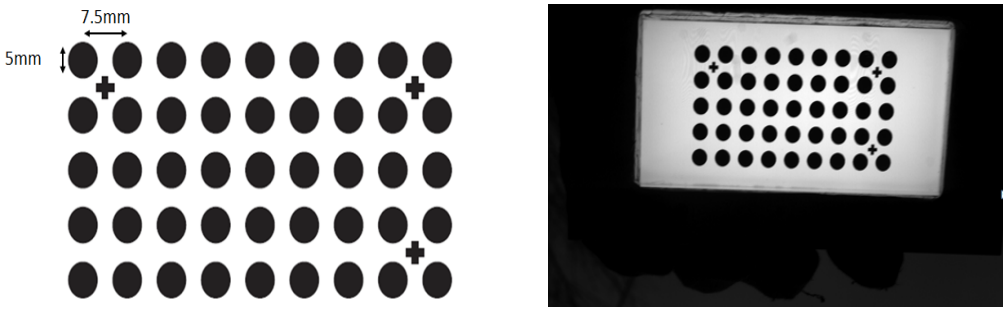

Figure 2.8: The camera calibration pattern.

We cannot use 3D calibration target due to limited depth of field in our present application. Therefore, we focus on the camera calibration methods that use 2D planar target. The dot-grid pattern shown in figure 2.8 has been used in this work. This is a small pattern that is possible to fit within the camera's field of view. It contains 45 tiny circular dots, whose centers are used as the feature points. The diameter of the dot grid is 5mm, and the distance between adjacent centers

is 7.5mm. The cross pattern between the dot-grids has been used to determine the pattern's orientation during the calibration procedure.

In the first part of this section, we summarize the state of art methods for classical camera calibration, and detail the planar based camera calibration method proposed by Zhang [111]. In the second part, we make a summarized review on present Scheimpflug calibration techniques, then we propose two new calibration methods for Scheimpflug device using the described Scheimpflug formation model (see section 2.1.2). This is because the pinhole model assumptions used by classical camera calibration techniques [1, 21, 33, 78, 93, 100, 104, 111] are not valid anymore for cameras under Scheimpflug set-up. The first method we proposed is based on optimally estimating the Scheimpflug angles needed to remove Scheimpflug distortions in the acquired images, while the second method is purely based on lens distortion models.

2.2.1 Classical Calibration

There is a very large literature on camera calibration, and the most influential works for geometric camera calibrations include DLT/Faugeras [1, 21], Tsai [93] and Zhang [111]. Determining camera parameters from known world points and their corresponding image projections is called the camera calibration problem, and the main goal is to find the linear projection matrix $\mathscr{A}$.

Since the relation between the 3D world and 2D image projections ($\mathbb{R}^3 \implies \mathbb{R}^2$) is linear, most of the calibration methods use Direct Linear Transformation (DLT) to extract the projection matrix. The aim of DLT is to solve linear equations using Linear Least Square (LLS) methods. Assuming we have at least 6 known feature points, an over determined system of linear equation is formed, and then solved by eigenvalue decomposition using the so called Singular Value Decomposition (SVD). The estimated matrix $\mathscr{A}$ using LLS can there-after be decomposed to camera intrinsic $\mathscr{K}$ and extrinsic parameters $[\mathscr{R}|\mathscr{T}]$, as in Faugeras, and Zhang [21, 111]. An alternative decomposition of the projection matrix is proposed by these authors [38, 63].

The perspective projection is a linear model of image formation that does not take into account the geometric distortions caused by the lens used. When one takes into account the lens distortion parameters in the camera calibration, the model becomes nonlinear. The best solution in the literature is to estimate the camera parameters independently, then refine the estimated camera parameters in a non-linear optimization technique with the addition of the lens distortion parameters. This is done using bundle adjustment with Levenberg-Marquardt iteration [98].

Zhang [111] search for an initial solution, followed by a nonlinear optimization based on the maximum likelihood. In the first step, an approximation of projection matrix is obtained based on DLT approach, followed by applying self calibration techniques to obtain absolute conic matrix that allows us to obtain the camera parameters. Subsequently, optical distortion coefficients

are modeled independently, before final optimization of all parameters (distortion and camera parameters) in a general framework.

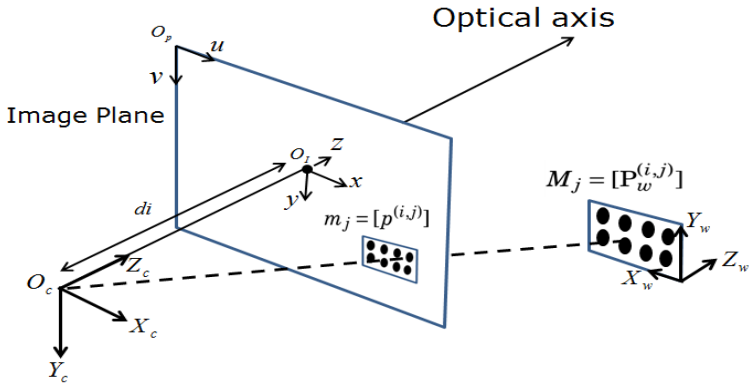

Figure 2.9: Planar based camera calibration.

Let's define an object model plane $\boldsymbol{M}$ containing n feature points, and $\mathbf{m}$ its corresponding image plane in pixel coordinate (see figure 2.9). At each pose $j = 1,\ldots,m$ of the object model plane, $\boldsymbol{M}_j(3\times n)$ feature points are projected to their corresponding target $\boldsymbol{m}_j(2\times n)$ pixels in the image, so that m number of $\mathscr{A}_{(j)}$ matrices can be estimated. Using homogeneous coordinates, we can write the relation as,

$$\boldsymbol{m}_j = \mathscr{A}_{(j)}\boldsymbol{M}_j \quad \text{where } \mathscr{A}_{(j)} = \mathscr{K}[r_1 \quad r_2 \quad r_3 \quad |\mathscr{T}]_{(j)} \tag{2.16}$$

and r_1, r_2, r_3 represents the columns of the rotation matrix $\mathscr{R}$. The matrix $\mathscr{K}$ that contains the intrinsic parameters is constrained to be the same for $j = 1,\ldots,m$. This will be fully explained later in the chapter.

The use of planar object for calibration in equation (2.16) means that we can assume $Z_w^{(i)} = 0$ in the world coordinate system. Therefore, the third column of $\mathscr{A}_{(j)}$ will be equal to zero. Hence, for a single pose j of a model plane, each feature points i, where $i = 1,\ldots,n$ respects:

$$\lambda_{(j)}\begin{bmatrix} u^{(i)} \\ v^{(i)} \\ 1 \end{bmatrix}_{(j)} = \mathscr{K}[r_1 \quad r_2 \quad 0 \quad |\mathscr{T}]\begin{bmatrix} X_w^{(i)} \\ \mathrm{Y}_w^{(i)} \\ \mathrm{Z}_w^{(i)} = 0 \\ 1 \end{bmatrix} \tag{2.17}$$

Without loss of generality, j is forgotten for the subsequent demonstration. Therefore, a model point $P_w(X_w, Y_w, Z_w)_w$ on a planar calibration object (i.e. $Z_w = 0$) and its corresponding image pixel $p(u,v)_p$ is related by a 3×3 homography $\mathscr{H}$ matrix. Therefore, the m poses of the target object plane give rise to m homographies.

In order to estimate the $\mathscr{H}$ matrix, we need at least 3 feature points on the calibration target (i ≥ 3) so that an over-determined system of linear equations is solved (See appendix 6.1 for the normalized homography estimation using Linear Least Square (LLS) [35]).

From the estimated homography matrix $\mathscr{H}$, Zhang [111] then proposed a method based on image of the absolute conic to extract the constrained intrinsic matrix $\mathscr{K}$ from the m poses of the calibration target. The author imposed two basic constraints on the $\mathscr{K}$ matrix to extract the image of absolute conic $\mathscr{B} = \mathscr{K}^{-T}\mathscr{K}^{-1}$ [35], and finally proposed a close form solution to extract the required camera intrinsic parameters $\mathscr{K}$. The full method is described in Appendix 6.2.

One way to deal with the lens distortion is the use of bundle adjustment technique. It should be estimated independently from the camera parameters. The idea is to optimize altogether the camera and distortion parameters in a single non-linear optimization procedure. The process of refining calibration parameters is known as bundle adjustment. The distortion and camera parameters are refined through minimizing reprojection error as shown in equation (2.18) using Levenberg-Marquardt method:

$$min \sum_{j=1}^{m}\sum_{i=1}^{n} \|\tilde{p}^{(i,j)} - \hat{p}^{(i,j)}(\hat{\mathscr{K}}, \hat{\mathscr{R}}_{(j)}, \hat{\mathscr{T}}_{(j)}, \hat{k}_1, \hat{k}_2, \hat{k}_3, \hat{t}_1, \hat{t}_2)\|^2 \tag{2.18}$$

where $\tilde{p}^{(i,j)}$ is the real coordinate of image pixels, and $\hat{p}^{(i,j)}$ denote those of the reprojected pixels using the estimated system parameters $(\hat{\mathscr{K}}, \hat{\mathscr{R}}_{(j)}, \hat{\mathscr{T}}_{(j)}, \hat{k}_1, \hat{k}_2, \hat{k}_3, \hat{t}_1, \hat{t}_2)$.

2.2.2 Scheimpflug Calibration

2.2.2.1 State of art

There are few papers about intrinsic calibration of Scheimpflug device. Haig et al. [32] proposed a mathematical model to compensate for lens inclination that is lower than 1°. The first method for larger tilt angle was proposed by Li et al. [53], and based on single Scheimpflug angle θ. The authors assumed that the tilt angle is perfectly known due to mechanical set-up, so the acquired images are directly rectified.

The issue of bundle adjustment for Scheimpflug calibration was first addressed by Louhichi et al. [54] using single angle θ. Legarda et al. [51] extend the method to two angles (θ, γ). The two methods used the same bundle adjustment technique on the tilted image plane, but the initialization of the Scheimpflug angles is different. Louhichi et al. [54] initialize the Scheimpflug angles with magnification factor, while Legarda et al. [51] uses the output result of classical Zhang method that is directly applied on the tilted image plane, in order to extract the initial Scheimpflug angles. Full experiments and detailed comparisons with pinhole methods are provided in the recent paper of Legarda et al. [52].

The main problem with the state of art methods is that the Scheimpflug angles have to be known precisely. However, it is not easy to accurately determine these angles by experimental adjustment. Therefore, we have proposed two calibration methods. The first method does not need accurate initial Scheimpflug angle estimation. This method works step by step, by first simplifying the distortion introduced by the Scheimpflug tilt effect, using the proposed formation model. Then, we extract camera parameters from the projected pixels on the untilted image plane using the same approach as Zhang [111]. Finally, a bundle adjustment technique based on Levenberg-Marquardt is used to refine the intrinsic camera parameters.

For the second method, we propose a method that can deal with introduced Scheimpflug distortions, without the need to estimate their optimal angles. Indeed, we propose an original strategy that consists in fitting Scheimpflug model framework into the lens distortion model. Finally, we compare the proposed methods with classical camera calibration and the state of art method of Legarda et al. [52].

2.2.2.2 Method based on Scheimpflug angle estimation

To calibrate the Scheimpflug device, we need to move the calibration pattern at different orientations (poses) from the camera to cover the whole camera's viewpoints. The pattern must be well oriented to avoid large image blur that is highly possible under Scheimpflug set-up.

The usual plane based calibration technique used in Zhang [111] is applied for the proposed Scheimpflug model. Recall $i = 1,..,n$ be the number of known featured points on a target plane and $j = 1,..,m$ be the number of target poses. Each point of the calibration target in the world coordinate system $P^{(i,j)}({X_w}^{(i,j)}, {Y_w}^{(i,j)} {Z_w}^{(i,j)})_w$ is matched to its corresponding pixel $\tilde{p}_t^{(i,j)}(\tilde{u}_t^{(i,j)}, \tilde{v}_t^{(i,j)})_p$ in the tilted image plane. The Scheimpflug device calibration involves three main steps as described below.

Projection onto the untilted image plane

As a result of distortion introduced by the tilt effect, we thereby propose to perform the calibration procedure on the untilted "virtual" image plane. This means that we are interested in projecting pixels $\tilde{p}_t^{(i,j)}(\tilde{u}_t^{(i,j)}, \tilde{v}_t^{(i,j)})_p$ to their untilted point $\tilde{p}^{(i,j)}(\tilde{X}_c^{(i,j)}, \tilde{Y}_c^{(i,j)}, di)_c$.

By simplifying the proposed Scheimpflug formation model in equation (2.14) (see Appendix 7.1.3 for the simplification), we extract $\tilde{p}^{(i,j)}(\tilde{X}_c^{(i,j)}, \tilde{Y}_c^{(i,j)}, di)_c$ or $\tilde{p}_t^{(i,j)}(\tilde{x}^{(i,j)}, \tilde{y}^{(i,j)}, 0)_I$ in the camera coordinate for all points $\tilde{p}_t^{(i,j)}(\tilde{u}_t^{(i,j)}, \tilde{v}_t^{(i,j)})_p$:

$$
\begin{aligned}
\tilde{x}^{(i,j)} = \tilde{X}_c^{(i,j)} &= \frac{di[s_x\ cos\ \gamma({\tilde{u}_t}^{(i,j)} - u_0) + s_y\ sin\ \gamma\ sin\ \theta({\tilde{v}_t}^{(i,j)} - v_0)]}{di - s_x\ sin\ \gamma({\tilde{u}_t}^{(i,j)} - u_0) + s_y\ sin\ \theta\ cos\ \gamma\ ({\tilde{v}_t}^{(i,j)} - v_0)} \\
\tilde{y}^{(i,j)} = \tilde{Y}_c^{(i,j)} &= \frac{di\ [s_y\ cos\ \theta({\tilde{v}_t}^{(i,j)} - v_0)]}{di - s_x\ sin\ \gamma\ ({\tilde{u}_t}^{(i,j)} - u_0) + s_y\ sin\ \theta\ cos\ \gamma\ ({\tilde{v}_t}^{(i,j)} - v_0)}
\end{aligned}
\tag{2.19}
$$

However, we need to give initial values for di, θ, γ, u_0, v_0, s_x and s_y in order to use equation (2.19). These values should be very close to the true ones to ensure fast convergence of the subsequent minimization steps. We can use the values given by the manufacturer for f as di, s_x, s_y, u_0 and v_0 respectively.

Finally, points $\tilde{p}_t^{(i,j)}(\tilde{x}^{(i,j)}, \tilde{y}^{(i,j)})_I$ can be expressed in their pixel coordinates $\tilde{p}_t^{(i,j)}(\tilde{u}^{(i,j)}, \tilde{v}^{(i,j)})_p$ using matrix $\mathcal{K}_b$ as shown below,

$$\begin{bmatrix} \tilde{u}^{(i,j)} \\ \tilde{v}^{(i,j)} \end{bmatrix} = \begin{bmatrix} 1/s_x & 0 & u_0 \\ 0 & 1/s_y & v_0 \\ 0 & 0 & 1 \end{bmatrix} \begin{bmatrix} \tilde{x}^{(i,j)} \\ \tilde{y}^{(i,j)} \\ 1 \end{bmatrix} \tag{2.20}$$

Target to image plane homography estimation

We can then extract the homography $\mathcal{H}_{(j)}$ between the feature points $P_w^{(i,j)}(X_w^{(i,j)}, Y_w^{(i,j)}, Z_w^{(i,j)})_w$, and their corresponding pixels $\tilde{p}^{(i,j)}(\tilde{u}^{(i,j)}, \tilde{v}^{(i,j)})_p$ on the untilted image plane, using the normalized DLT algorithm described in Appendix 6.1. The estimated homography $\mathcal{H}_{(j)}$ may not be accurate due to the presence of noise. This is because linear solutions like the DLT only minimize an algebraic error function, and do not consider geometric error.

Therefore, it is required to refine the homography by minimizing the reprojection error corresponding to the image distance between the reprojected pixels $\hat{p}^{(i,j)}$, and a measured/true ones $\tilde{p}^{(i,j)}$ as,

$$min \sum_{i=1}^{n} \|\tilde{p}^{(i,j)} - \hat{p}^{(i,j)})\|^2, \quad \text{where } \hat{p}^{(i,j)} = \hat{\mathcal{H}}_{(j)} P_w^{(i,j)} \tag{2.21}$$

The reprojection error in equation (2.21) is minimized based on maximum likelihood using Levenberg-Marquardt iterative method (see Appendix 6.1.1).

Scheimpflug angle estimation

We can estimate the constrained camera intrinsic parameter matrix $\mathcal{K}$ and extrinsic parameter matrix $[\mathcal{R}_{(j)} | \mathcal{T}_{(j)}]$ from the refined homography $\mathcal{H}_{(j=1,\ldots,m)}$ using Zhang's method (see Appendix 6.2).

From the proposed Scheimpflug image formation, we have shown that the tilt deformation is only possible on the tilted plane, therefore we omit the lens distortion simplification during the Scheimpflug angle estimation. Given an initial value of the tilted angles $\{\theta_0, \gamma_0\}$ coupled with the preceding estimated camera parameters, we propose a bundle adjustment technique to refine the tilt angles $(\hat{\theta}, \hat{\gamma})$ as:

$$\{\hat{\theta}, \hat{\gamma}\} = min_{\{\theta,\gamma\}} \sum_{j=1}^{m} \sum_{i=1}^{n} \|\tilde{p}^{(i,j)} - \hat{p}^{(i,j)}(\hat{\mathcal{K}}, \hat{\mathcal{R}}_{(j)}, \hat{\mathcal{T}}_{(j)}, \{\hat{\theta}, \hat{\gamma}\})\|^2 \tag{2.22}$$

where $\hat{p}^{(i,j)}$ are the estimated coordinates of the projected pixel that depend on $(\hat{\mathscr{K}}, \hat{\mathscr{R}}_{(j)}, \hat{\mathscr{T}}_{(j)}, \{\hat{\theta}, \hat{\gamma}\})$. We illustrate in Appendix 7.2 how the bundle adjustment optimization procedure is used to determine the optimal Scheimpflug angles.

Camera parameters refinement

Once the optimal tilt angles $(\hat{\theta}, \hat{\gamma})$ have been estimated, we project all tilted pixels $\tilde{p}_t^{(i,j)}$ to the optimal untilted plane pixels $\tilde{p}_{\{\hat{\theta},\hat{\gamma}\}}^{(i,j)}$. We can then minimize the reprojection error on the untilted plane as:

$$min \sum_{j=1}^{m} \sum_{i=1}^{n} \| \tilde{p}_{\{\hat{\theta},\hat{\gamma}\}}^{(i,j)} - \hat{p}^{(i,j)}(\hat{\mathscr{K}}, \hat{\mathscr{R}}_{(j)}, \hat{\mathscr{T}}_{(j)}, \hat{k}_1, \hat{k}_2, \hat{k}_3, \hat{t}_1, \hat{t}_2, \hat{s}_1, \hat{s}_2) \|^2 \tag{2.23}$$

$\hat{p}^{(i,j)}$ are the estimated coordinates of the projected pixel that depend on $\hat{\mathscr{K}}, \hat{\mathscr{R}}_{(j)}, \hat{\mathscr{T}}_{(j)}$ and the distortion coefficients.

Improvement with fronto-parallel approach

The accurate extraction of the feature pixels (dot-grid centers) impacts the calibration performance. Due to the manipulation of the target according to different poses, circular grids become ellipse-like shapes in the image as a result of the perspective projection. This makes it difficult to precisely locate the feature pixels. With the Scheimpflug device, these difficulties are even more accentuated, so that the circle grids appear blurred and low contrasted in the acquired images.

To improve the accuracy of the camera parameter estimation, we incorporate the fronto-parallel transformation method [14, 97]. An image is created which looks as if the planar calibration is perfectly orthogonal to the optical axis of the camera. This image, called frontal image, has been computed thanks to cubic interpolation [71] (See Appendix 7.3). Examples of fronto-parallel transformation have been displayed in figure 2.10.

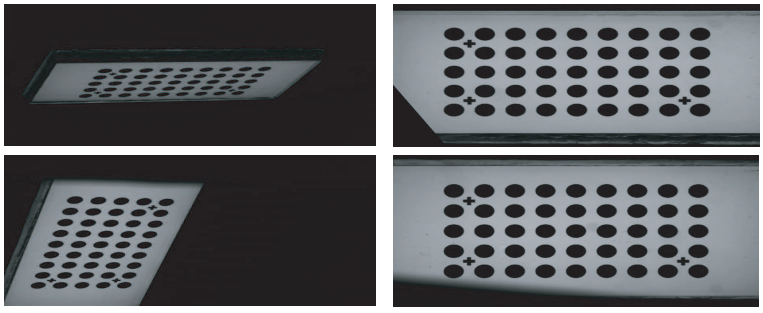

Figure 2.10: Examples of real and resulting frontal images.

Once the optimization in equation (2.23) has been achieved, we propose to compute the frontal images using the estimated system parameters at each iteration. The procedure is as follows,

1. Create the frontal images using earlier estimated camera parameters $\hat{\mathscr{K}}, \hat{\mathscr{R}}_{(j)}, \hat{\mathscr{T}}_{(j)}$, and lens distortion parameters $(\hat{k}_1, \hat{k}_2, \hat{k}_3, \hat{t}_1, \hat{t}_2, \hat{s}_1, \hat{s}_2)$,

2. Extract the feature pixels in the resulting frontal images,

3. Reproject the detected feature pixels on the frontal images back into the "untilted" image plane,

4. Perform bundle adjustment of all parameters as below,

$$min \sum_{j=1}^{m} \sum_{i=1}^{n} \| \tilde{p}^{(i,j)}_{\{\hat{\theta},\hat{\gamma}\}} - \hat{p}^{(i,j)}(\hat{\mathscr{K}}, \hat{\mathscr{R}}_{(j)}, \hat{\mathscr{T}}_{(j)}, \hat{k}_1, \hat{k}_2, \hat{k}_3, \hat{t}_1, \hat{t}_2, \hat{s}_1, \hat{s}_2) \|^2 \tag{2.24}$$

   $\tilde{p}^{(i,j)}_{\{\hat{\theta},\hat{\gamma}\}}$ is the real pixel on the "optimal" untilted image plane, and $\hat{p}^{(i,j)}$ is the estimated one from bundle adjustment.

5. Go back to step "1" until feature pixels mean variation is lower than a threshold (0.001px).

This improvement completes the first method for Scheimpflug device calibration that is based on the simplification of the distortions introduced by Scheimpflug tilt effect.

2.2.2.3 Method based on lens distortion model

This second Scheimpflug device calibration method does not require one to estimate the Scheimpflug tilt angles $\{\theta, \gamma\}$. We fit Scheimpflug framework into distortion model with the use of fronto-parallel approach, and iterative bundle adjustment scheme.

Analogy of Scheimpflug to distortion model

Note that it is geometrically incorrect to use the lens distortion equations on the tilted image plane since it has been formulated for the untilted one, but we will go ahead and write it for the following explications. As the images provided by the camera are the projection of the world points on the tilted image plane, we propose to write a classical lens distortion expression for tilted plane pixels $\tilde{p}_t$ as,

$$\begin{aligned} \tilde{u}_t &= u_t + (u_t - u_0)[k_1 r^2 + k_2 r^4 + k_3 r^6] + [2t_2 x_t y_t + t_1(r^2 + 2x_t^2)] + [s_1 r^2] \\ \tilde{v}_t &= v_t + (v_t - v_0)[k_1 r^2 + k_2 r^4 + k_3 r^6] + [2t_1 x_t y_t + t_2(r^2 + 2y_t^2)] + [s_2 r^2] \end{aligned} \tag{2.25}$$

By setting di to "1" in the proposed Scheimpflug image formation in equation (2.14), we can express the coordinates (x_t, y_t) of the point in the tilted image plane from those of coordinates (x, y) in the untilted image plane as:

$$x_t = \frac{x - y\ sin\ \gamma\ tan\ \theta}{x\ sin\ \gamma - y\ tan\ \theta + cos\ \gamma} + x_0$$
$$y_t = \frac{y\ cos\ \gamma}{cos\ \theta[x\ sin\ \gamma - y\ tan\ \theta + cos\ \gamma]} + y_0 \tag{2.26}$$

Our main goal here is to express the Scheimpflug formation model in a clearer form that allows better view of how the tilted point $\mathrm{p}_t(x_t, y_t)$ is deduced from the untilted one $\mathrm{p}(x, y)$. The required simplification is expressed as:

$$x_t = x\frac{1}{cos\ \gamma} - y\frac{sin\ \gamma\ tan\ \theta}{cos\ \gamma} + x_0 x\frac{sin\ \gamma}{cos\ \gamma} - x_0 y\frac{tan\ \theta}{cos\ \gamma}$$
$$y_t = y\frac{1}{cos\ \theta} - yy_0\frac{sin\ \theta}{cos\ \theta\ cos\ \gamma} + xy_0\ tan\ \gamma \tag{2.27}$$

Equation (2.27) shows that,

1. There is a scaling factor $\frac{1}{cos}$ on both x and y coordinates which can be handled in the camera matrix by the focal length coefficients $f_x \equiv \frac{di}{s_x}$ and $f_y \equiv a\frac{di}{s_y}$,
2. The y coordinate contributes individually to express x_t which will be taken into account by the camera matrix skew factor sk,
3. The $xy \equiv x_0 y$ or $y_0 x$ term contributes for both x_t and y_t, which is a non-linear quantity (meaning that the camera matrix can't handle it). This should be handled in a non-linear optimization technique.

   Solution : We propose to introduce two new coefficients c_1 and c_2 in the distortion model so that equation (2.25) is expressed as:

$$\tilde{u}_t = u_t + (u_t - u_0)[k_1 r^2 + k_2 r^4 + k_3 r^6] + [t_1(r^2 + 2x_t^2)] + [s_1 r^2] + c_1 x_t y_t$$
$$\tilde{v}_t = v_t + (v_t - v_0)[k_1 r^2 + k_2 r^4 + k_3 r^6] + [t_2(r^2 + 2y_t^2)] + [s_2 r^2] + c_2 x_t y_t \tag{2.28}$$

The difference between equations (2.25) and (2.28) is that we have removed the second order tangential ($2t_2$, $2t_1$), and replaced it by coefficients (c_1, c_2) that are independent of the tangential distortion. However, we will see later that we can initialize the coefficients (c_1, c_2) using the tangential ones.

Therefore, the use of non-linear optimization in the form of an "iterative" bundle adjustment should be able to estimate the coefficients (c_1, c_2), and at the same time be able to refine the other system parameters.

Calibration procedure

In summary, the calibration procedure for the new proposed method based on lens distortion model is as follows,

1. Detect the feature pixels $\tilde{p}_t^{(i,j)}$ on the tilted image plane that corresponds to feature points $P_w^{(i,j)}$, where $i = 1,\ldots,n$ and $j = 1,\ldots,m$,
2. Estimate the homography $\mathscr{H}_{(j)}$ between the feature pixels and points (see equation 2.21),
3. Extract the camera parameters using Zhang's method (see Appendix 6.2). The extracted parameters are $\hat{\mathscr{K}}$, $\hat{\mathscr{R}}_{(j)}$ and $\hat{\mathscr{T}}_{(j)}$,
4. Refine these parameters, with lens distortion through bundle adjustment based on Levenberg-Marquardt optimization technique (see appendix 7.2). The refined parameters are $\hat{\mathscr{K}}$, $\hat{\mathscr{R}}_{(j)}$, and $\hat{\mathscr{T}}_{(j)}$ and the lens distortion coefficients $(\hat{k}_1,\hat{k}_2,\hat{k}_3,\hat{t}_1,\hat{t}_2)$,
5. Initialize the "iterative" bundle adjustment scheme with the parameters estimated in step (4). Then, set the additional parameter $\hat{sk}$=0, coefficients $\hat{s}_1,\hat{s}_2 = 0$, $\hat{c}_1 = 2\hat{t}_2$, and $\hat{c}_2 = 2\hat{t}_1$,

   Start the iterative bundle adjustment

6. Create the frontal images using the parameters $(\hat{\mathscr{R}}_{(j)}, \hat{\mathscr{T}}_{(j)}, \hat{\mathscr{K}}, \hat{k}_1,\hat{k}_2,\hat{k}_3,\hat{t}_1,\hat{t}_2, \hat{s}_1,\hat{s}_2, \hat{c}_1,\hat{c}_2)$,
7. Extract the feature pixels on the frontal images, then project them back to the tilted image plane,
8. Optimize all the parameters directly on the tilted image plane using bundle adjustment procedure as below,

$$\min \sum_{j=1}^{m}\sum_{i=1}^{n} \|\tilde{p}_t^{(i,j)} - \hat{p}_t^{(i,j)}(\hat{\mathscr{K}},\hat{\mathscr{R}}_{(j)},\hat{\mathscr{T}}_{(j)},\hat{k}_1,\hat{k}_2,\hat{k}_3,\hat{t}_1,\hat{t}_2,\hat{s}_1,\hat{s}_2,\hat{c}_1,\hat{c}_2)\|^2 \tag{2.29}$$

9. Go back to step (6) until the feature pixel variation is lower than a threshold.

2.2.3 Experiments and Results

We have carried out various tests to evaluate the proposed Scheimpflug calibration methods. The experiments have been done on different sets of data acquired by an industrial system set-up where the calibration images are perturbed by large distortions. Moreover, the system is placed in a thick "plexi" glass housing.

The first part of the experiment was carried out on images acquired with the laboratory prototype, while the second part has been performed with images acquired by real system set-up. The main aim of these experiments is to compare the calibration results of classical calibration method to the new proposed Scheimpflug calibration methods.

In the experimental table of this section, we use the following nomenclature ("**Classical**, **Legarda**, **Method I**, **Method II**") to describe the calibration methods,

- **Classical**: The classical camera calibration using Zhang's method (see section 2.2.1),
- **Legarda**: The state of art Scheimpflug device calibration method presented by Legarda et al. [52],
- **Method I**: The new Scheimpflug calibration method that requires the optimal estimation of Scheimpflug angles (see section 2.2.2.2),
- **Method II**: The new Scheimpflug calibration method that is based on lens distortion model (see section 2.2.2.3).

2.2.3.1 Laboratory Experiment

This experiment was carried out with the laboratory prototype using a firewire camera equipped with a sensor of 1280×1024 pixels whose size is $0.0067mm \times 0.0067mm$. We use a canon TS-E focal 24mm Scheimpflug lens, whose tilt angles range between $\pm 8.5°$. The image set contains only 25 calibration images, since we ensure that they cover the whole field of view of the camera.

Comparison between all methods

For the first test, the Scheimpflug angle on the X-axis has been tilted to approximately θ = -1.4°. Since we have no information about its adjustment on Y-axis, angle γ has been set to 0°. Figure 2.11 shows few examples of the calibration images used for this experiment. The accuracy of the camera calibration methods has been determined by using the mean reprojection error between the true coordinates of the feature pixels and the reprojected ones using the estimated camera parameters over the whole calibration images.

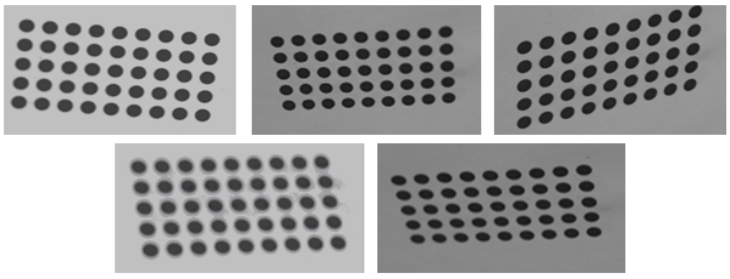

Figure 2.11: Scheimpflug calibration images at tilt angle -1.4°.

The experimental results are shown in table 2.1. We have used the same stopping criteria for the iterative bundle adjustment to avoid any bias between the compared methods. We have set the stopping criteria so that the iterative bundle adjustment procedure stops whenever the

mean variation of feature pixels between two successive steps is lower than (0.001px). The whole calibration procedure takes about 45 minutes, but the calibration results are already good at the third iteration. The fronto-parallel transformation procedure is time consuming since we need to create these frontal images and detect the feature pixels at each iteration. This procedure has been speed up under GPU, and the calibration time is lower than 7minutes.

	No Fronto-parallel			**Fronto-parallel**			
	Classical	**Legarda**	**Method I**	**Classical**	**Legarda**	**Method I**	**Method II**
$f_x, f_y(mm)$	25.59, 25.44	25.35, 25.40	25.50, 25.38	25.43, 25.45	25.54, 25.47	25.43, 25.39	25.54, 25.50
sk	-	-	-	-	-	-	19.98
$u_0, v_0(px)$	1100, 688	1038, 740	1190, 673	1034, 703	1141, 629	1016, 699	1115, 533
$\theta, \gamma(^\circ)$	-	-0.005, -1.385	-0.004, -1.399	-	-0.004, -1.382	-0.004, -1.399	-
k_1	-0.010	0.003	0.005	0.009	0.012	0.032	0.134
k_2	-5.727	-6.012	-4.384	-6.243	-5.321	-3.258	-2.0189
k_3	66.4455	52.015	40.011	58.124	54.614	45.321	31.589
t_1	0.003	0.027	0.003	0.004	0.0013	0.005	0.0052
t_2	-0.002	-0.017	-0.004	0.001	0.0031	0.006	0.0294
s_1	-	-	-	0.0015	-0.0059	0.0011	0.0032
s_2	-	-	-	0.0035	0.0034	0.0024	0.0029
c_1	-	-	-	-		-	0.0626
c_2	-	-	-	-		-	0.0065
mean err(px)	0.107	0.101	0.102	0.0553	0.054	0.0530	0.0500
std err(px)	0.023	0.022	0.023	0.0331	0.0319	0.0310	0.028

Table 2.1: Experimental intrinsic calibration comparison between all methods (Scheimpflug tilt angle is -1.4°).

In the calibration result table without fronto-parallel transformation, one can see that **Method I** performs better than the **Classical** (0.107 px → 0.102 px), and the Scheimpflug angles are well estimated. The fronto-parallel transformation improves the results obtained by these approaches, and the reprojection error is reduced by the factor of 2. **Method II** under the iterative bundle adjustment procedure provides the best calibration result compared to the other methods. In summary, the new proposed Scheimpflug calibration methods perform better than the classical calibration method in all cases (i.e. both with and without fronto-parallel transformation).

Larger Scheimpflug angle test

The aim of the second test is to verify the validity space of the **Method II** i.e. we want to verify that the assumptions made in **Method II** are still valid at large Scheimpflug angles. Therefore, experiments have been conducted with the same Scheimpflug device as earlier test, but with larger tilt angle close to 8.5°. In practice, any Scheimpflug angle that is greater than 8.5° is realistically impossible in our present application. Indeed, the camera-object distance has to be lower than 110mm in that case. Few examples of the calibration images for this experiment are shown in figure 2.12.

As the quality of the calibration images is very poor for this experiment, we increase the background lighting of the calibration pattern in order to get visible dot-grid patterns. Even with

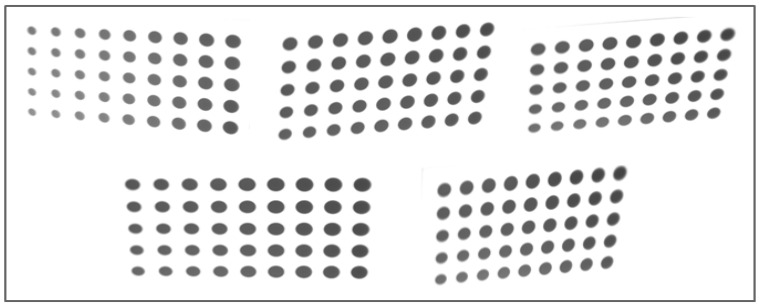

Figure 2.12: Calibration example images at Scheimpflug tilt angle 8.5°.

increased background lighting, one can still see that the quality of the images is degraded and the perspective distortion is highly visible in them. The calibration result is shown in table 2.2. The experimental result shows that our methods perform better than **Classical** one, and **Method II** provides the lowest reprojection error (0.0412px).

Parameters	**Fronto-parallel, angle 8.5°**		
	Classical	**Method I**	**Method II**
$f_x, f_y(mm)$	25.63, 25.59	25.58, 25.54	25.63, 25.50
sk	-	-	-30.65
$u_0, v_0(px)$	1017, 603	1082, 459	1065, 468
$\theta, \gamma(^\circ)$	-,-	8.321,0.009	-,-
k_1	-1.7104	-1.8069	-0.9980
k_2	7.2897	6.5230	3.8423
k_3	-15.5451	-32.124	-7.2740
t_1	-0.0072	-0.0072	0.0852
t_2	-0.0375	-0.0260	-0.0122
s_1	-0.1000	-0.0821	-0.2224
s_2	0.0584	0.0493	0.0281
c_1	-	-	-0.0493
c_2	-	-	0.0462
mean err(px)	0.0635	0.0461	0.0412
std err(px)	0.0443	0.0331	0.0291

Table 2.2: Experimental intrinsic calibration result at large Scheimpflug tilt angle 8.5°.

From our previous tests, the skew parameter sk has not been optimized under **Classical** and **Method I**. This is based on Zhang's assumption of skew parameters to be zero. We have decided to make additional test to verify the influence of the skew parameter sk. For this test, we add this parameter in the optimization procedure of **Classical** and **Method I**. The calibration results for this test are shown in table 2.3. We can see that the sk parameter has low influence in the accuracy of these methods in our application. Therefore, **Method II** is still the best of these methods.

Parameters	**Fronto-parallel, angle 8.5°** (with sk)		
	Classical	**Method I**	**Method II**
$f_x, f_y(mm)$	25.54, 25.47	25.49, 25.53	25.63, 25.50
sk	**15.71**	**12.31**	-30.65
$u_0, v_0(px)$	1141, 629	1109, 538	1065, 468
$\theta, \gamma(^\circ)$	-,-	8.321,0.009	-,-
k_1	-1.3816	-1.0814	-0.9980
k_2	3.9081	4.8812	3.8423
k_3	-5.895	14.0945	-7.2740
t_1	0.0253	-0.0053	0.0852
t_2	-0.0500	-0.06712	-0.0122
s_1	-0.2290	-0.1470	-0.2224
s_2	0.0619	0.0352	0.0281
c_1	-	-	-0.0493
c_2	-	-	0.0462
mean err(px)	0.0631	0.0463	0.0412
std err(px)	0.0451	0.0325	0.0291

Table 2.3: Experimental intrinsic calibration result at large tilt angle 8.5° (with sk).

The most important parameter under the Scheimpflug calibration using **Method II** is the proposed additional distortion coefficients c_1 and c_2. Indeed, the experimental results in this test show that **Method II** works well at large Scheimpflug tilt angles, and thus can be used to calibrate any Scheimpflug device.

2.2.3.2 Real System Experiment

We have carried out the calibration procedure on two sets of 25 images acquired outside the laboratory on the real system (see figure 2.13). The system to be calibrated uses a Basler camera with a resolution of 2040x1088 pixels, pixel size of $0.0055mm \times 0.0055mm$ and a Schneider-Kreuznach-f24mm adapter tilted to approximately $\theta_0 = 1.4^\circ$, $\gamma_0 = 0^\circ$ on X and Y-axis respectively. The experimental results are displayed in Table 2.4.

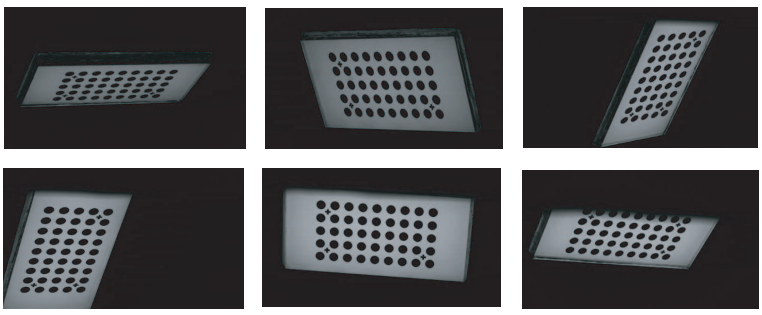

Figure 2.13: Calibration images captured using Scheimpflug camera.

Parameters	Set I (25 images)			Set II (25 images)		
	Classical	**Method I**	**Method II**	**Classical**	**Method I**	**Method II**
$f_x, f_y(mm)$	25.40, 25.39	25.54, 25.47	25.28, 25.36	25.40, 25.34	25.41, 25.34	25.52, 25.47
sk	-	-	26.63	-	-	-20.93
$u_0, v_0(px)$	1209, 672	1141, 629	1235, 647	1100, 602	1109, 572	1096, 623
$\theta, \gamma(^\circ)$	-,-	1.399, 0.004	-	-	1.390, 0.012	-
k_1	0.024	0.014	0.053	0.061	0.060	0.065
k_2	-4.235	-5.316	-4.120	-7.218	-7.013	-7.523
k_3	35.601	54.448	32.048	47.253	49.156	53.127
t_1	0.0107	0.0015	0.0133	0.0021	0.0052	0.0074
t_2	0.0113	0.0029	0.0115	0.019	0.0203	0.0214
s_1	-0.0122	-0.031	-0.0067	-0.0065	-0.0109	0.0009
s_2	-0.0135	-0.0148	-0.0085	-0.0090	-0.0087	0.0013
c_1	-	-	0.0278	-	-	0.0358
c_2	-	-	0.0385	-	-	0.0521
mean err(px)	0.0551	0.0525	0.0479	0.0543	0.0533	0.0481
std err(px)	0.0311	0.0309	0.0280	0.0321	0.0330	0.0280

Table 2.4: Experimental intrinsic calibration result with real system under fronto-parallel transformation.

By examining table 2.4 for the real system test, we can conclude that **Method II** provides the lowest mean reprojection error for the two sets of calibration images. Therefore, it has been chosen for further experiments in the next chapters of this PhD thesis to evaluate the 3D laser-camera system calibration.

2.2.4 Conclusion

We have proposed two calibration methods for any Scheimpflug device. The first method requires the optimal estimation of the Scheimpflug tilt angles, while the second method is based on lens distortion model by iterative bundle adjustment technique. With the second method, one does not need to estimate the optimal Scheimpflug angles. We have made detailed experimental comparison between the classical calibration method [111], state of art Scheimpflug method [52] and the proposed methods.

From the experimental results, we show that the proposed Scheimpflug calibration methods perform better than the state of art methods. Notably, the second method provides the best performance. We have also tested different methods for the extraction of feature pixels of the frontal image, such as digital image correlation [97], cross correlation, with sub-pixel detection methods. The choice of extraction method on the frontal images does not have any significant improvement on the calibration result.

Since these experiments have been carried out with a camera located inside a thick "plexi" glass housing, we assume that the proposed methods can be used for systems under moderate refractive distortions, thanks to the iterative bundle adjustment scheme.

2.3 Laser-Camera Calibration

The laser-camera system consists of a camera and a laser which projects a line stripe on the object to be measured (see figure 2.14). Let us consider the 3D point P_w that belongs to both the laser plane, and the object surface. The ray passing through the point P_w and the optical center O_c intersects the tilted image plane at point p_t and thus provides the coordinates of pixel corresponding to P_w in the scene. When the laser plane equation is known in the camera coordinate system $(O_c[X_c, Y_c, Z_c])_c$, the position of the 3D point P_w can be easily expressed in this coordinate system. Therefore, the laser-camera calibration consists in determining the equation of the laser plane in the camera coordinate system. See, for example the paper of Lanman et al. [50] on triangulation principles.

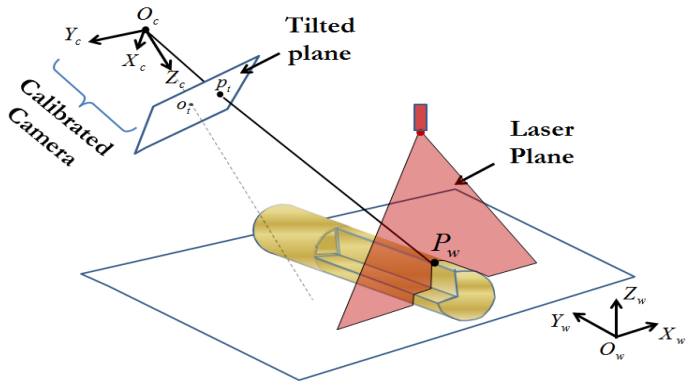

Figure 2.14: System laser-camera calibration.

From a well calibrated Scheimpflug device, the aim is to determine the transformation matrix between laser and tilted image plane. Since it is very difficult to determine the physical origin of the laser, one is required to place a calibration target/pattern with known coordinate system directly on the laser path. This target must contain enough non-collinear feature points in order to identify the laser plane equation.

2.3.1 Calibration Target

The choice of laser-camera calibration target depends on the application, expected accuracy and budget constraint. We classify calibration targets that have been used over the years in to planar and 3D targets. The planar targets are generally made from planar object, mostly using papers with printed patterns. These printed patterns are built so that feature pixels can be extracted from the images formed from the intersection of laser plane with these printed patterns. The planar target needs to be moved at various positions on the laser path in order to get enough non collinear points needed to represent the laser plane. Thereafter, the parameters from various poses are unified to obtain a single plane parameter using non-linear optimization techniques.

Few examples of planar target include grid pattern [107], square pattern [112], and chess pattern [84].

The use of 3D target is mostly common in industries where the cost of equipment is not a major factor. They use manufactured 3D targets that have been known to a reference coordinate with high accuracy. It is very difficult to obtain a relevant good laser-camera calibration from just one single pose of the 3D target (i.e. single-shot laser calibration technique) due to possible occlusion of the feature points from the viewing camera. Therefore, most of the laser-camera calibration methods still require minimum of two poses of the 3D target. This is done by coordinated translation of the pattern [109] or coordinated insertion for both ring step gauge [46] and puzzle-like gauge [40].

Other trends of inexpensive 3D targets are available. The targets are created with the use of two or three orthogonal planes from readily available planar patterns [41, 62, 110]. These methods avoid moving the pattern at different orientations by incorporating shape and geometric informations such as vanishing point [101], invariance of cross-ratio [11, 41, 102], and scattered point projection [6].

For an industrial application, 3D calibration target is the best choice to reach the expected accuracy. The main problem under Scheimpflug set-up is the low depth of field, which makes it difficult to use a full-scale 3D calibration target. Therefore, we have proposed a new laser-camera calibration target that is suitable to the scope of the project (see figure 2.15). The proposed pattern is suitable for a single-shot laser-camera calibration method, so that one can calibrate the system by the analysis of a single image representing the calibration target.

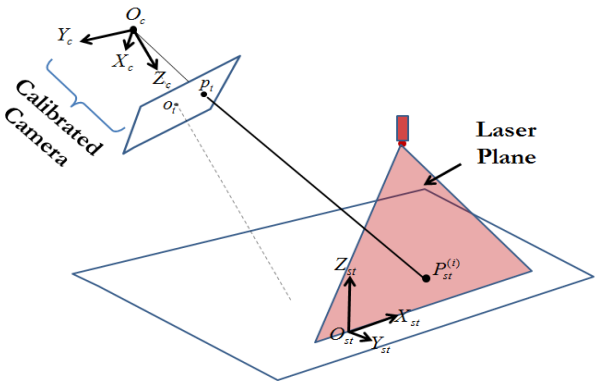

Figure 2.15: The laser-camera calibration set-up. The laser calibration target is "hidden" due to confidentiality constraint.

2.3.2 Calibration Procedure

In the laser-camera calibration set-up shown in figure 2.15, the coordinates of the feature points $P_{st}^{(i)}$ $(i = 1,\dots,n \geq 20)$ on the calibration target are known with reference to the coordinate system origin $(O_{st}[X_{st}, Y_{st}, Z_{st}])_{st}$ that has been placed at the target center. Our aim is to be able to represent any point formed by the camera ray intersection with the laser plane directly in reference to the O_{st} coordinate.

Feature pixel extraction

From a single image of the calibration target, we need to first extract the distorted tilted pixels $\tilde{p}_t^{(i)}(\tilde{u}_t^{(i)}, \tilde{v}_t^{(i)})_p$ that corresponds to the feature points $P_{st}^{(i)}$ on the calibration target. The calibration accuracy strongly depends on the accurate extraction of these feature pixels.

Thanks to the proposed Scheimpflug calibration method in section 2.2, the distorted tilted pixels $\tilde{p}_t^{(i)}(\tilde{u}_t^{(i)}, \tilde{v}_t^{(i)})_p$ are then transformed to their undistorted points $p_t^{(i)}(x_t^{(i)}, y_t^{(i)})_I$ in the tilted image plane.

Laser to camera homography estimation

We can determine the (3×3) homography $\mathscr{H}_{st}$ between the undistorted normalized image points $p_t^{(i)}(x_t^{(i)}, y_t^{(i)})_I$ and world feature points $P_{st}^{(i)}(X_{st}^{(i)}, Y_{st}^{(i)}, Z_{st}^{(i)})_{st}$. This is shown in equation (2.30), and can be solved using the normalized DLT method explained in Appendix 6.1.

$$\lambda \begin{bmatrix} x_t^{(i)} \\ y_t^{(i)} \\ 1 \end{bmatrix} = \mathscr{H}_{st} \begin{bmatrix} X_{st}^{(i)} \\ \mathrm{Y}_{st}^{(i)} \\ \mathrm{Z}_{st}^{(i)} \end{bmatrix} \tag{2.30}$$

As the perfect alignment of the calibration target is not always guaranteed, we propose to refine $\mathscr{H}_{st}$ using special bundle adjustment through minimizing symmetric transfer error [35, 81, 82, 92]. This is done by minimizing reprojection error on both the target plane O_{st} and the tilted image plane O_I as shown in equation (2.31). The minimization is performed with Levenberg-Marquardt iterative method, where $\hat{\mathscr{H}}_{st}$, $\hat{\mathscr{H}}_{st}^{-1}$ are the forward and backward estimated homographies.

$$\min \sum_{i=1}^{n} \|p_t^{(i)} - \hat{\mathscr{H}}_{st}\hat{P}_{st}^{(i)})\|^2 + \|P_{st}^{(i)} - \hat{\mathscr{H}}_{st}^{-1}\hat{p}_t^{(i)})\|^2, \tag{2.31}$$

Note: Further decomposition of the homography matrix to extract the laser plane parameters is detailed in the following papers [22, 79].

2.3.3 Experiments and Results

We have tested the laser-camera calibration method on both synthetic and real images. For the synthetic test, we have simulated the image acquisition thanks to the proposed Scheimpflug image formation model (excluding optical lens distortions). For the real test, we capture an image of the calibration target that has been illuminated by the laser. The Scheimpflug device used for this experiment has been calibrated in the real system experiment (see section 2.2.3.2).

The accuracy of the laser-camera calibration method has been determined using RMSE error in mm over n feature points. The laser calibration results are shown in table 2.5. Although the calibration procedure requires a single image of the target, we have captured three images with varying camera exposure time (exp. time) so that the best calibration result between these three images is retained.

		Synthetic Images			**Real Images**		
Camera Calibration	f_x, f_y (mm)	25.33, 25.33			25.28, 25.36		
	sk	-			26.63		
	u_0, v_0 (px)	1020, 512			1235, 647		
	θ, γ (°)	1.52, 0.00			-		
	k_1				0.053		
	k_2				-4.120		
	k_3				32.048		
	t_1				0.0133		
	t_2				0.0115		
	s_1				-0.0067		
	s_2				-0.0085		
	c_1				0.0278		
	c_2				0.0385		
	mean err. (px)	0.0000			0.0479		
	std err. (px)	0.0000			0.0280		
		Image 1	Image 2	Image 3	Image 1	Image 2	**Image 3**
Laser Calibration	exp. time	20	40	60	20	40	**60**
	nb. feat. (n)	20	20	20	22	22	**24**
	mean err. (mm)	0.045	0.050	0.041	0.030	0.025	**0.015**

Table 2.5: Laser-camera calibration result with both synthetic and real images.

The accuracy of the proposed laser-camera calibration method largely depends on the accuracy of the feature pixel extraction i.e. the pixels that correspond to the feature points of the proposed laser calibration target. The best result for the real images test has been obtained when the exposure time of the camera is high, while not producing saturated images. In this case, we were able to well extract a high number of feature pixels.

2.4 Conclusion

In this chapter, we have presented a two step calibration method for a 3D laser-camera system under Scheimpflug set-up. The method requires that we first calibrate the Scheimpflug camera independently, followed by determining the transformation matrix between the laser plane and the calibrated camera. We have proposed two intrinsic camera calibration methods for the Scheimpflug device. The first method is based on optimally estimating the Scheimpflug angles, while the second method is based on lens distortion model. The proposed methods use iterative bundle adjustment coupled with fronto-parallel transformation technique to improve the experimental results. The obtained reprojection error is lower than 0.050px. Indeed, the proposed second method using lens distortion model provides the best result to calibrate any Scheimpflug device. In the context of our application, we consider that the obtained error is satisfying since the camera depth of field is low and the image acquisition is corrupted by strong optical distortions.

The laser-camera calibration method has been proposed to fit to the scope and requirements of the project. It is a single shot calibration method where the calibration is performed using only a single image of the calibration target. This method is highly sensitive to the accuracy of extracted feature pixels, as well as the perfect alignment of the calibration pattern on the laser path. We have proposed to use a symmetric bundle adjustment, which helps to compensate for slight misalignment of the pattern on the laser path. The laser-camera calibration procedure has been tested on synthetic and real image acquisitions, and the lowest mean reprojection error is close to 0.015mm.

The obtained error is lower than those provided by state of art calibration methods. Indeed, the 3D laser-camera system under Scheimpflug set-up defined by Li et al. [53] provides higher error of (0.060mm) at a working distance largely less than in our present application. Under classical calibration with less working distance as us, Zhang et al. [109] provides calibration error close to (0.050mm). Based on these results, the performance reached by our proposed calibration procedure outperforms the state of art methods. Once the system has been calibrated, images are analyzed to estimate the cross-section of contact wires.

CHAPTER 3

CROSS-SECTION MEASUREMENT

The aim of our 3D measurement system is to estimate the cross-section of different contact wires (with or without wear). In this chapter, we describe the procedure for estimating cross-section of contact wires. For readers clarity, the successive processing steps for the cross-section measurements have been grouped in the following sections:

- Profile Determination
- Profile Analysis

3.1 Profile Determination

The goal of the profile determination is to extract the 3D profile of the contact wire directly from acquired images. The profile determination procedure is divided into three steps shown in figure 3.1. First, a pre-processing step extracts the region of interest (ROI) using simple image thresholding [34]. The second step estimates the coordinates of pixels that correspond to the laser stripe centers. Finally, from these stripe centers, the 3D profile is determined using the laser-camera triangulation method that is explained in section 2.3.

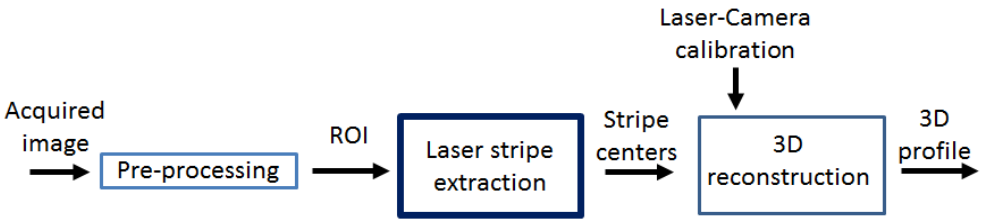

Figure 3.1: Profile determination step, from acquired images to 3D profile determination.

3.1.1 Laser Stripe Extraction

Apart from the laser-camera calibration method explained in the previous chapter, the measurement performances reached by the system also depend on the accuracy of the laser stripe center extraction [36]. Laser stripe extraction consists in determining the coordinates of pixels that correspond to the center of the line representing the laser projected on the contact wire [61].

Figure 3.2 is an example image of a laser stripe projected on the contact wire. Let us denote (u,v) as the spatial coordinates of pixels in the region of interest (ROI) whose size is $n \times m$. The goal of the laser stripe extraction is to determine the coordinate $S(v)$ that corresponds to the center of the laser line for each column v. One can see that the image in figure 3.2 is largely perturbed by specular reflection and speckle noise. This is due to the surface aspect of the contact wire as well as the imperfection of the laser source.

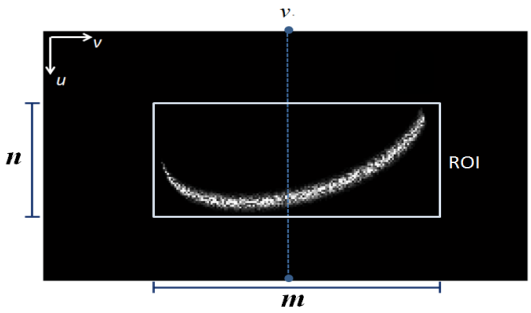

Figure 3.2: An example laser stripe image.

These perturbations modify the grey-level profile as illustrated in figure 3.3a. Past authors assumed an ideal Gaussian form with no noise perturbation [72], as shown in figure 3.3b. In that case, it is relatively easy to localize the laser peak that corresponds to the stripe center at each column.

(a) Acquired

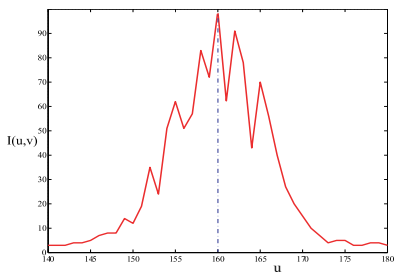

(b) Gaussian model

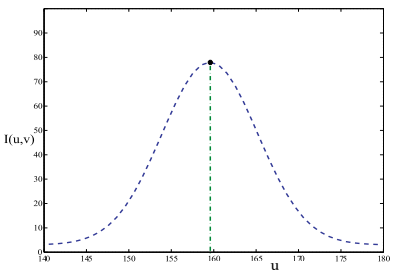

Figure 3.3: Grey-level profile along a column v.

Due to the spatial discretization of the image, it is necessary to extract the laser stripe center location S(v) with sub-pixel accuracy, since the accuracy of 3D estimation is affected by the

resolution of the acquired images. Assuming that the grey-level profile $I(u,v)$ along the column v presents a regularized peak (see figure 3.3b), we denote the coordinate pixel u_0 whose grey-level intensity I_0 is the highest along column v (see figure 3.4). Then, we number the neighboring row pixels before and after u_0 as (u_{-1}), and (u_{+1}), with their grey-level intensities I_{-1} and I_{+1}, respectively.

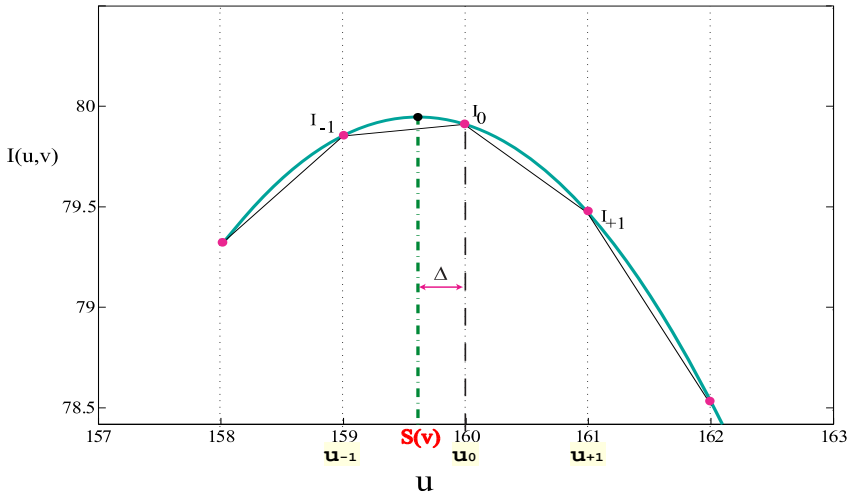

Figure 3.4: Zoomed of profile peak along column v.

From these three pixels near the regularized profile peak, the solution will be to find the displacement Δ, so that the true extrema is located at the displacement Δ from position u_0,

$$S(v) = u_0 + \Delta \quad \text{where } \Delta \in [-0.5, 0.5]. \tag{3.1}$$

Generally, the laser stripe extraction is done in the following way. The region of interest is first determined by distinguishing laser stripe projected on the background from that projected on the object [96]. Then, images should be first filtered to remove the grey-level irregularity of neighboring pixels, which makes the peak identification more robust [89]. Then, the center is determined thanks to a sub-pixel approach applied to the peak of the filtered profile [4, 65].

Once centers have been determined for each column, Sun et al. [90] proposed to apply a smoothing spline algorithm to obtain a continuous curve of centers across successive columns of the image. As such a post-processing step is time consuming, it cannot be integrated in a real-time 3D measurement system that analyses $\approx$ 1800 images per second. Therefore, we focus only on one dimensional extraction methods, i.e. laser stripe extraction methods that analyze each image column v independently. This strategy allows real-time laser stripe extraction. The

methods described in this section, are based on sub-pixel interpolation applied to grey-level profile regularized by adapted Gaussian filter.

3.1.1.1 Image filtering

The assumption to use a Gaussian filter comes from the Gaussian profile followed by the laser light source. Therefore, noisy images can be transformed to the Gaussian form thanks to filter $g(.)$ expressed as,

$$g(u) = e^{-\frac{u}{2\sigma^2}} \tag{3.2}$$

where σ is the standard deviation of the Gaussian function. The choice of the σ parameter is very important and its empirical value will be shown later in the experimental section of this chapter.

Let $\tilde{I}(u,v)$ represent the convolution response using the Gaussian filter in equation (3.2). The response $\tilde{I}(u,v)$ should give a regularized and/or distinct peak that follows a Gaussian law. Therefore, we can determine first the location u_0 of the peak, followed by using the sub-pixel interpolation methods to extract the stripe center $S(v)$.

3.1.1.2 Sub-pixel interpolation algorithm

We have retained three sub-pixel methods that are well suited to our application. Several authors attempt to fit the grey-level profile with a parabolic function [4, 65]. The center can also be estimated thanks to a linear approximation [24] or by computing the center of gravity of grey-level [36].

Parabolic fitting

Given that the grey-level profile around the peak is smooth, the sub-pixel location can be determined using the parabolic estimator,

$$S(v) = u_0 + \frac{\tilde{I}_{+1} - \tilde{I}_{-1}}{4\tilde{I}_0 - 2(\tilde{I}_{+1} + \tilde{I}_{-1})}. \tag{3.3}$$

Fischer et al. [24] have also proposed a Gaussian approximation method which is indeed the same as parabola fitting if we exempt the "log" operator. Indeed, this log operator is ineffective in our present application.

Linear Approximation

Linear interpolation can also be used to represent the spread of intensity around the laser peak locations (u_{-1}), u_0 and (u_{+1}), so that the laser stripe center sub-pixel $S(v)$ is,

$$S(v) = \begin{cases} u_0 + \frac{\tilde{I}_{+1} - \tilde{I}_{-1}}{2\tilde{I}_0 - 2\tilde{I}_{-1}}, & \text{if } (\tilde{I}_{+1} > \tilde{I}_{-1}) \\ u_0 + \frac{\tilde{I}_{+1} - \tilde{I}_{-1}}{2\tilde{I}_0 - 2\tilde{I}_{+1}}, & \text{else.} \end{cases} \tag{3.4}$$

Assumption about dispersion constancy may lead to inaccurate results when the laser line width varies. When the grey level distribution around the peak of the profile is largely uneven, Qi et al. [72] proposed the use of modified Gaussian function.

Center of Gravity

The Centre of Gravity (CoG) algorithm also known as "Center-of-Mass" has been used for laser stripe center determination using a simple weighted average as,

$$S(v) = u_0 + \frac{\tilde{I}_{+1} - \tilde{I}_{-1}}{\tilde{I}_{-1} + \tilde{I}_0 + \tilde{I}_{+1}}. \tag{3.5}$$

3.1.1.3 Experiments and Results

For industrial application purposes, we have compared the performances reached by three presented approaches when the image resolution changes and when the laser width varies along the image column (see figure 3.2). In the experimental set-up, several cylindrical objects (whose diameter is 14.50mm) that are directly illuminated by a laser, are aligned in the Field of View (FOV) of the Scheimpflug camera at three different horizontal and vertical positions, denoted **Positions [11 to 33]**, across the measurement area in the scene described by $O_{st}(X_{st}, Y_{st}, Z_{st})$ plane in the scene (see figure 3.5). We can evaluate the robustness of the tested approaches against the spatial resolution of the image since the camera-object distance varies with respect to these positions.

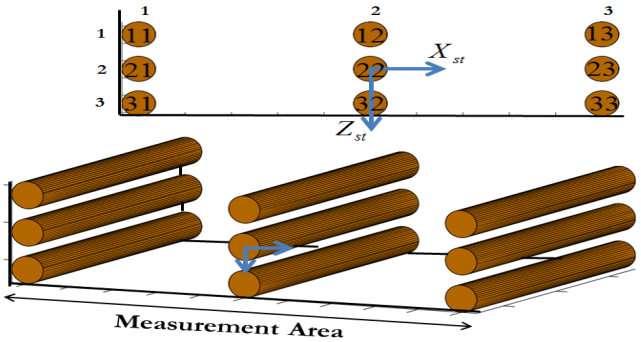

Figure 3.5: Experimental set-up with cylindrical objects arranged on the measurement area.

The objects have been aligned in the FOV to cover the extreme limits of the depth of field locations related to Scheimpflug system set-up. Due to the curve nature of the measured objects, the location of the cylindrical object in the scene and the Scheimpflug tilt effect, the width of the laser w varies between 2 to 20 pixels across each column of the image ROI.

We have developed a tool to simulate the experimental set-up in figure 3.5. To obtain the ground truth, we have applied the laser stripe extraction methods on synthetic images that have

been generated by our simulation tool. The images were created, thanks to Scheimpflug formation model described in chapter 2.1.2. We have tested the algorithms on simulated images of the cylindrical object corrupted by speckle noise with density whose variance has been set to 0.04 [89]. The variance value has been set to well represent the moderate level of noise perturbation in acquired images of the cylindrical object. The performance of each method is measured by using the distance between the estimated stripe center and that of the ground-truth, along each column of the image.

Robustness against spatial resolution

The accuracy of the stripe extraction method is estimated thanks to the error measure $\bar{d}$ expressed in equation (3.6), where $(S^t(v)^{(i)}, S(v)^{(i)})$ are the ground-truth and the determined laser stripe centers, respectively, along the m columns of the ROI.

$$\bar{d} = \frac{1}{m}\sum_{i=1}^{m} |S^t(v)^{(i)} - S(v)^{(i)}| \tag{3.6}$$

The full experimental evaluation for the three described methods is shown in table 3.1. The images have been filtered, thanks to the Gaussian filter of equation (3.2) where σ is set to 4. At each **position [11 - 33]**, the minimum error between the three methods is written in bold font and we display the number m of columns where the laser stripe is inside the ROI. This table first shows that m varies according to the position of the object observed by the camera. It also shows that parabolic fitting outperforms CoG and linear methods for all object positions.

Position	m	**Mean error $\bar{d}$(pixel)**		
		Parabolic	**Linear**	**CoG**
11	124	**0.0498**	0.0661	0.2345
12	124	**0.0506**	0.0697	0.2354
13	110	**0.0731**	0.0931	0.2371
21	153	**0.0599**	0.0844	0.2208
22	131	**0.0672**	0.0799	0.2535
23	113	**0.0655**	0.0821	0.2498
31	158	**0.0700**	0.0877	0.2353
32	133	**0.0618**	0.0812	0.2378
33	116	**0.0634**	0.0775	0.2432

Table 3.1: Comparison between the laser stripe extraction methods using mean error $\bar{d}$.

We can also notice that errors provided by the linear method are close to but higher than those provided by parabolic method. However, several other tests (not presented in this thesis report) reveal that CoG method provides good results only when the grey-level profile is Gaussian-like so that u_0 is guaranteed to be very close to the center sub-pixel location S(v). An example of laser stripe extraction provided by the parabolic fitting method is shown in figure 3.6.

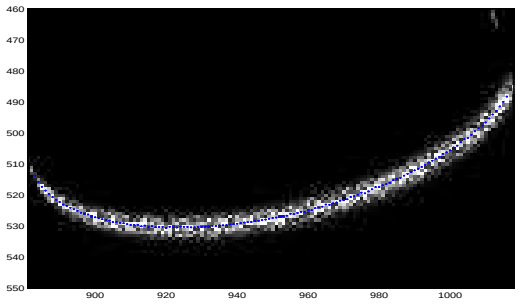

Figure 3.6: Stripe extraction result provided by parabolic fitting in the ROI.

Robustness against laser width

The accuracy of the center determination depends on the performance of image Gaussian filtering. We have made several experiments to determine the empirical $\hat{\sigma}$ parameter that is well suited to our application. For the experiment, we simulate the cylindrical object at **Position [22]** (see figure 3.5), then we determine the error $\bar{d}$ over all the column m in the ROI. We plot in figure 3.7 the mean error $\bar{d}$ against σ parameter ranging from 1 to 35. The plot shows that the $\hat{\sigma}$ parameter for parabolic fitting and linear approximation methods ranges between 10 and 15.

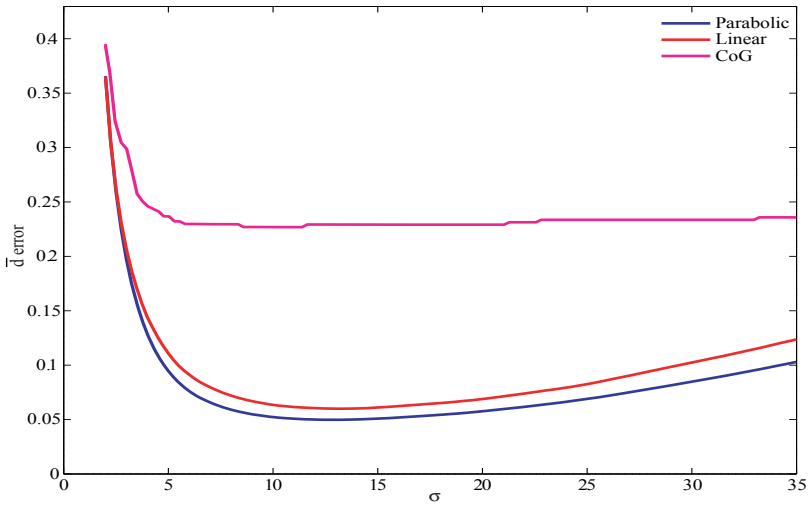

Figure 3.7: Error measure $\bar{d}$ vs σ , for the three tested methods.

Based on Stegger [87] formulations, the relation between the laser width w expressed in pixels and the optimal $\hat{\sigma}$ parameter for a Gaussian profile is shown in equation (3.7). If we look closer at our earlier experiment result shown in figure 3.7, we will see that equation (3.7) is experimentally verified. The laser width w has approximately 18 pixels across the image column (except at the extreme ends of the image profile) so that the computed $\hat{\sigma}$ should be higher than 10, and close to the local minimum.

$$\hat{\sigma} \geq w/\sqrt{3}. \tag{3.7}$$

The ROI in this application contains the laser stripe projection on the contact wire that is acquired by the camera. The ROI contains $i = 1,\ldots,m$ number of columns, so that a set of centers $\{v^{(i)}, S(v)^{(i)}\}$ has been determined. Indeed, for the laser stripe extraction task, we obtain the stripe centers $S(v)^{(i)}$ for all the m columns present in the ROI.

3.1.2 3D Reconstruction

From the laser stripe extraction explained in the previous section, the method that uses the parabolic fitting is the best choice. It is well suited to our application where the acquired images of the contact wire are corrupted by noise. This method has been used to determine the laser stripe center $S(v)$.

Thanks to the camera parameters given by the calibration procedure, the m stripe centers $\{v^{(i)}, S(v)^{(i)}\}$ are first transformed to their undistorted normalized tilted image points $p_t^{(i)}(x_t^{(i)}, y_t^{(i)})_I$, that is denoted as **Image profile** in figure 3.8. Then, we determine the **2D profile** of the contact wire using the inverse of homography $\mathscr{H}_{st}^{-1}$ as shown in equation (3.10). The 2D profile results from the projection of the image profile to the laser plane.

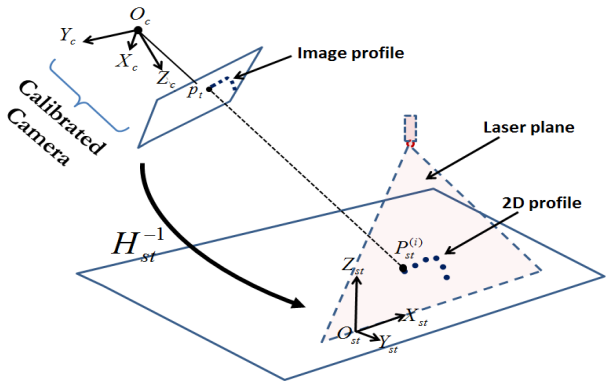

Figure 3.8: Illustration of the 3D reconstruction that gives 2D profile.

We will detail in the next part of this section the full 3D reconstruction procedure under our laser-Scheimpflug device system set-up.

3.1.2.1 Removal of distortions

The extracted stripe centers $\{v^{(i)}, S(v)^{(i)}\}$ are distorted pixels $\tilde{p}_t^{(i)}(\tilde{u}_t^{(i)}, \tilde{v}_t^{(i)})_p$ that are located on the tilted image plane. Thanks to earlier camera calibration, we transform these pixels to their corresponding distorted normalized points $\tilde{p}_t^{(i)}(\tilde{x}_t^{(i)}, \tilde{y}_t^{(i)})_I$ using equation (3.8).

$$\begin{bmatrix} \tilde{x}_t^{(i)} \\ \tilde{y}_t^{(i)} \end{bmatrix} = \mathscr{K}_b^{-1} \begin{bmatrix} \tilde{u}_t^{(i)} \\ \tilde{v}_t^{(i)} \\ 1 \end{bmatrix} \quad \text{where} \quad \mathscr{K}_b = \begin{bmatrix} 1/s_x & sk & u_0 \\ 0 & 1/s_y & v_0 \\ 0 & 0 & 1 \end{bmatrix} \tag{3.8}$$

Using the distortion parameters from earlier camera calibration, we can determine the undistorted normalized tilted points $p_t^{(i)}(x_t^{(i)}, y_t^{(i)})_I$ by removing the distortions. The removal of these distortions depends on the proposed calibration method. In this chapter, we use the second method that is based on lens distortion model (see section 2.2.2.3). These distortions are the radial, tangential, thin prism and the proposed Scheimpflug ones (c_1, c_2). By simplifying the proposed distortion model in equation (2.28), we can remove the distortions using equation (3.9).

$$
\begin{aligned}
x_t &= \frac{(\tilde{x}_t - [t_1(r^2 + 2x_t^2)] + [s_1 r^2] + c_1 x_t y_t)}{1 + k_1 r^2 + k_2 r^4 + k_3 r^6} \\
y_t &= \frac{(\tilde{y}_t - [t_2(r^2 + 2y_t^2)] + [s_2 r^2] + c_2 x_t y_t)}{1 + k_1 r^2 + k_2 r^4 + k_3 r^6}
\end{aligned} \tag{3.9}
$$

We need to remove these lens distortions in an iterative manner. From our experiments, the number of iteration steps has been empirically set to the value of 10.

3.1.2.2 Triangulation using homography

Once the undistorted normalized coordinate points $p_t^{(i)}(x_t^{(i)}, y_t^{(i)})_I$ denoted as **Image profile** in figure 3.8 have been determined, we can then use the inverse of homography from earlier laser calibration (see section 2.3) to get the reconstructed profile as shown in equation (3.10), where $(X_{st}^{(i)}, Y_{st}^{(i)}, Z_{st}^{(i)})$ are coordinates of the system associated with the laser plane.

$$
\begin{bmatrix} X_{st}^{(i)} \\ \mathrm{Y}_{st}^{(i)} \\ \mathrm{Z}_{st}^{(i)} \end{bmatrix} = \mathscr{H}_{st}^{-1} \begin{bmatrix} x_t^{(i)} \\ y_t^{(i)} \\ 1 \end{bmatrix} \tag{3.10}
$$

As the $\mathrm{Y}_{st}^{(i)}$ of the reconstructed profile is very close to zero, we set its value to zero so that $(X_{st}^{(i)}, Y_{st}^{(i)} = 0, Z_{st}^{(i)})$ for every reconstructed points. Therefore, we propose to use the term **2D profile** for the reconstructed profile rather than **3D profile**. This means that the reconstructed profile in this work is actually a (2D) curve that represents the wire profile.

Few examples of reconstructed 2D profiles of round and oval contact wires are shown in figures 3.9 and 3.10, respectively. The proposed laser-camera system is placed at one side from the wire to be inspected, so it can only inspect (at a single time) half profile instead of the full contact wire profile. Figure 3.9a shows a round wire profile with no wear while figure 3.9b shows a round wire profile with an early stage of wear. Likewise, figure 3.10a shows an oval wire profile with no wear but with a slight rotation, while figure 3.9b shows an oval wire that has a wear. One should note that the reconstructed points that belong to the notch of the contact wire have been removed in the pre-processing step.

(a) No wear (b) Worn-out

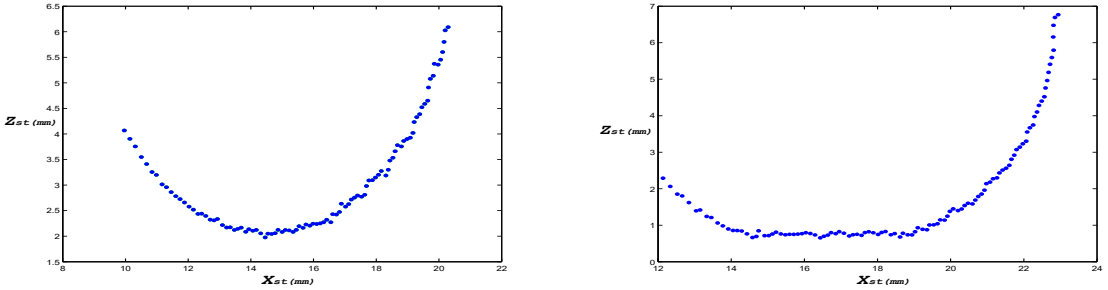

Figure 3.9: The reconstructed 2D profile for round wires.

(a) No wear (rotation) (b) Worn-out

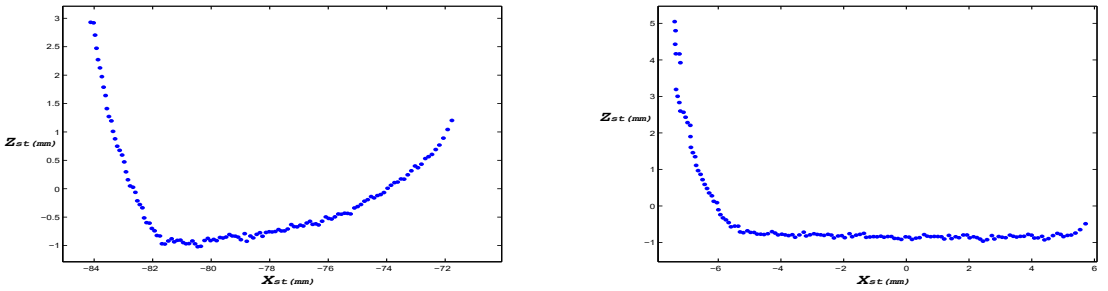

Figure 3.10: The reconstructed 2D profile for oval wires.

3.1.3 Summary and Conclusion

In the first part of this section, we have proposed the combination of image filtering and sub-pixel interpolation methods to accurately extract the laser stripe centers in images corrupted by speckle and Gaussian noise. This method is well suited to environments where conditions about the laser source, and object types cannot be controlled, such as in 3D measurements of steels, metals, and irons. We have shown that parabolic fitting provides the best accuracy for laser stripe center extraction while being suitable for real-time implementation. Thanks to this analysis of the extracted stripe centers, we are able to provide a reconstructed 2D profile that will facilitate relevant estimation of the contact wire cross-section.

Although the proposed laser stripe center extraction has been effective for moderate noise perturbation of the contact wire images, the reconstructed 2D profiles are still noisy and have irregular shape (see figures 3.9 and 3.10), compared to real contact wire profile without any form of perturbations. Moreover, only half of the wire profile is available to estimate the cross-section. So, these problems make it difficult to directly extract meaningful information required to estimate the cross-section from the 2D profile. To deal with these problems, we have proposed a profile analysis method that will be described in the next section.

3.2 Profile Analysis

For the profile analysis (see figure 3.11), the reconstructed 2D profile is pre-processed to remove noisy isolated points and points that belong to the contact wire notch. Next, we use non-parametric regression method to smooth the 2D profile. Indeed, its irregular shape results from the contact wire surface aspect and possible grease deposit.

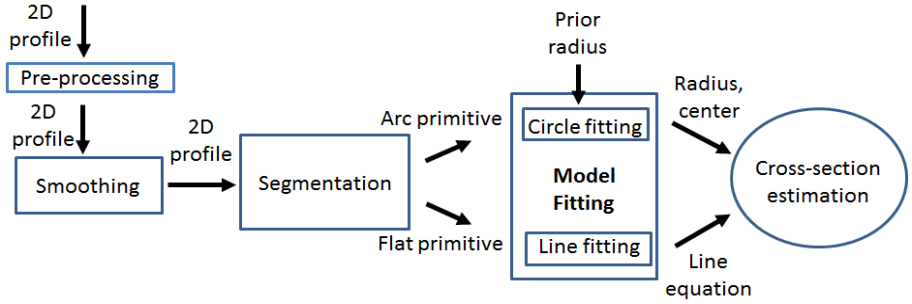

Figure 3.11: Illustration of the profile analysis procedure.

During the segmentation step, we combine various point analysis algorithms to partition the 2D profile into the arc and flat primitives that represent the basic geometric shapes of contact wire as shown in figure 3.12. This step labels the profile points to either the arc or the flat primitives of the contact wire. Finally, we fit a circle to the points that belong to the arc primitives and lines to those that belong to the flat primitives. This will contribute to the cross-section estimation of the contact wire profile.

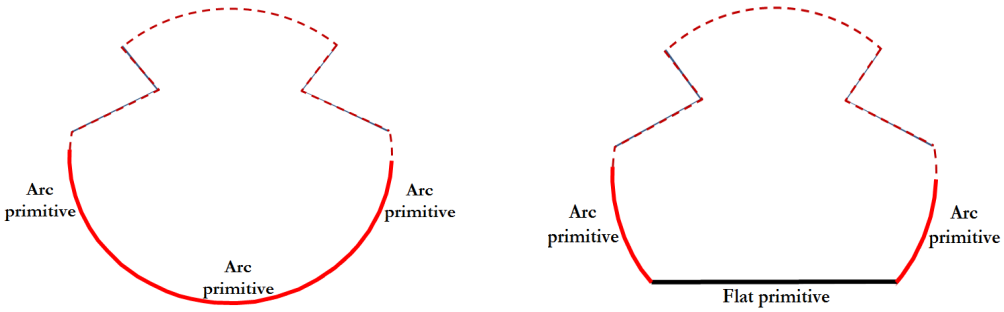

Figure 3.12: Primitive representation of the contact wire profiles.

3.2.1 Regularization by Smoothing

Our main objective is to smooth the reconstructed 2D profile represented as $P_{st}^{(i)}(X_{st}^{(i)}, Y_{st}^{(i)} = 0, Z_{st}^{(i)})$ from section 3.1.2. Linear regression is a simple way to model the relationship between these data points. This is done with model equation (3.11), where ϵ is random error due to noise present in the data, while a and b are parameters of the model line equation. This is a simple model that

can be used as a form of linear regression on any given data points. Although the model is easy to interpret, it still uses a very restrictive assumption about the linear relationship between the data points.

$$Z_{st}^{(i)} = a.X_{st}^{(i)} + b + \epsilon \qquad \text{i=1,...,m} \tag{3.11}$$

In our present case, we need to use a more complex model, which better reflects the unknown relationship between the data points. This is mostly done with polynomial regression. However, as there are many possibilities of wear profile shapes, finding the right relationship on their points becomes challenging. Therefore, we propose to use non-parametric regression methods. The most common methods are the Kernel Smooth Regression (KSR) and Smoothing Spline [19, 95]. We have tested these two methods, and KSR provides the best results for our application and thus is explained in this section.

The non-parametric regression is written as a form of linear equation given by equation (3.12), where $f(.)$ is the regression/smoothing function, and ϵ_i are the random errors.

$$Z_{st}^{(i)} = f(X_{st}^{(i)}) + \epsilon_i \qquad i = 1,\ldots,m \tag{3.12}$$

The aim is to estimate the underlying regression function $\hat{f}(X_{st}) = E(Z_{st}|X_{st})$ that smooths the sample data to obtain a function that falls between the pure parametric regression and interpolation between each point of the data.

3.2.1.1 Smoothing by Kernel Regression

Kernel Smooth Regression (KSR) is a non-parametric way for regression task. The most common method is proposed by Nadaraya-Watson [68]. The method is based on locally weighted average between the neighborhood of data points using kernel $\mathbb{K}$ as a weighting function. The regression function $\hat{f}(X_{st})$ at X_{st} is then given as:

$$\hat{f}(X_{st}) = \frac{\sum_{i=1}^{m} \mathbb{K}(X_{st}, X_{st}^{(i)}) Z_{st}^{(i)}}{\sum_{i=1}^{m} \mathbb{K}(X_{st}, X_{st}^{(i)})}, \qquad \text{where } \mathbb{K}(X_{st}, X_{st}^{(i)}) = exp(-\frac{(X_{st} - X_{st}^{(i)})^2}{2h^2}) \tag{3.13}$$

In this application, the kernel used is in form of Gaussian weighted average filter and is centered on a neighborhood distribution determined by bandwidth size h (see appendix 6.3.1 for further description).

We have applied the described kernel smooth regression method on example reconstructed profile using two different bandwidths $h = [0.1, 0.5]$, and the results are shown in figures 3.13 and 3.14, respectively. The KSR result is drawn with **"line plot"** in the figure in order to well illustrate the interpolation between the data points. The fitted line follows all the data points when the bandwidth $h = 0.1$, whereas we have a smoother fits at bandwidth $h = 0.5$.

(a) $h = 0.1$ (b) $h = 0.5$

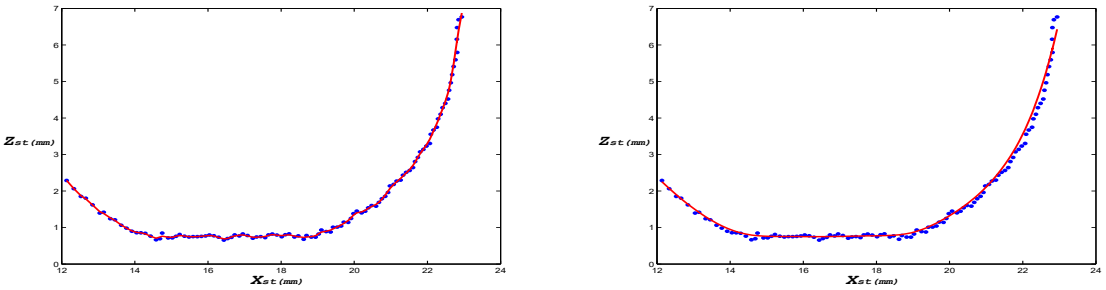

Figure 3.13: Kernel smoothing on 2D profile of the round wire with wear (see figure 3.9b).

(a) $h = 0.1$ (b) $h = 0.5$

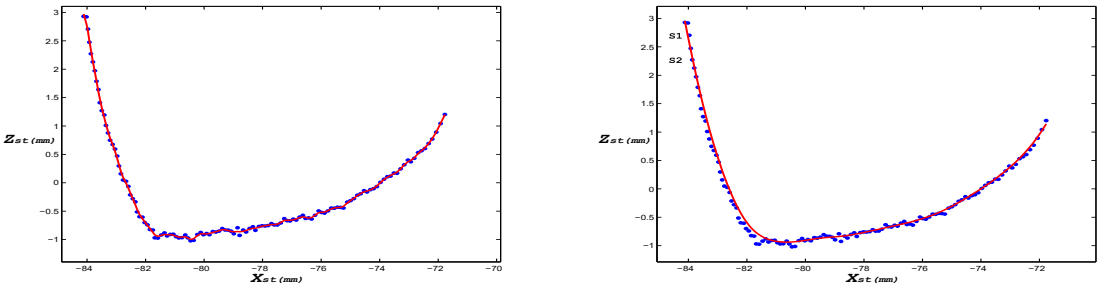

Figure 3.14: Kernel smoothing on 2D profile of the oval wire with no wear (see figure 3.10a).

Indeed, we see from earlier figures that the result is suitable for our application at $h = 0.5$ because it properly smooths the flat primitive of the 2D profile, even at the expense of the modification of arc primitive. In the ideal case, the smoothing output of the flat primitive should be perfectly straight (i.e. exhibit line property). This is a strong assumption here, and must be respected in order to well distinguish the arc from the flat primitives.

3.2.2 2D Profile Segmentation

The objective of the profile segmentation is to decompose the 2D profile into the arc and flat primitives, as illustrated in figures 3.15 and 3.16. From these two basic primitives, we can represent all the contact wire types, with or without wear. We assume that flat primitive contains

points that correspond to the wear while arc primitive contains the remaining points. These will be further explained in the remaining part of this section.

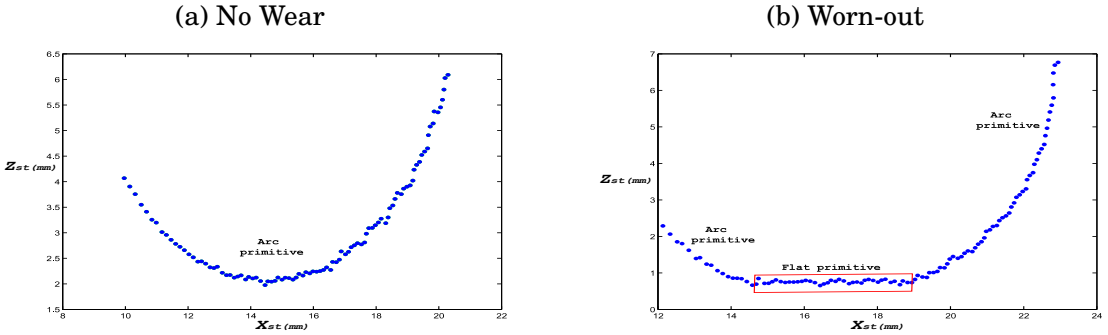

Figure 3.15: Primitive illustration for round 2D profiles.

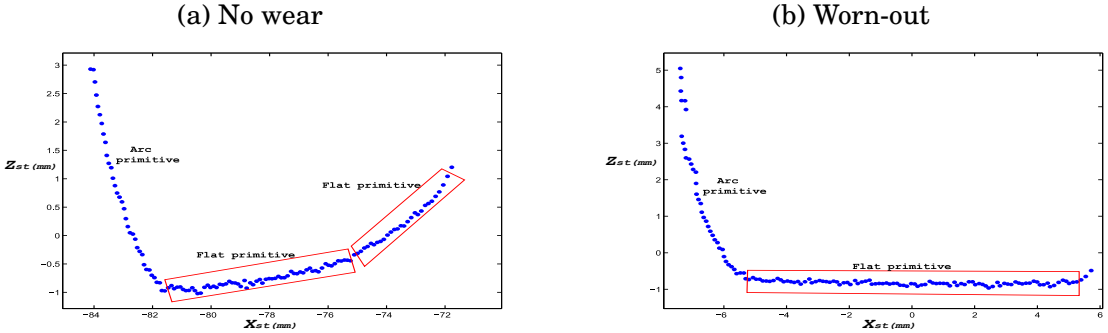

Figure 3.16: Primitive illustration for oval 2D profiles.

We have combined point analysis and pattern recognition methods to determine the arc and flat primitives. We present next the segmentation procedure followed by the estimation of the wire's cross-section area.

3.2.2.1 Profile decomposition into segments

First, we propose to decompose the 2D profiles into linked segments, thanks to polygonal approximation scheme. Polygonal approximation also known as curve simplification has been used to approximate the 2D profile. There are vast literature on this subject and have been used in various applications such as shape analysis and matching, compression for cartography, and real-time visualization [37, 105].

The goal of polygonal approximation in this application is to represent the 2D profile with fewer points denoted as "knot" points. The problem is to find the set of knot points which decompose the 2D profile into disjoint segments that link the first to the last points of the profile.

Kramer-Douglas-Peucker Algorithm [74]

To decompose the 2D profile into segments, a curvature criterion is used. The curvature criterion is based on the orthogonal distance d between the segment and the farthest point as shown in figure 3.17. The output segment is a good approximation of the profile if this distance d remains less than a threshold.

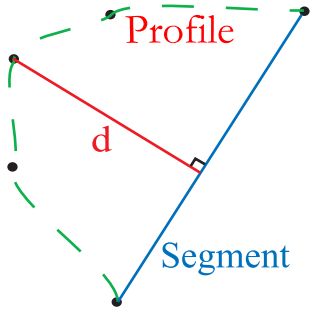

Figure 3.17: Curvature criterion

The Kramer-Douglas-Peucker algorithm is simple, efficient and responds to our requirements in this application. At first iteration the first and last points of the 2D profile are "knots" points, and also set the starting segment to this point. The orthogonal distance d from this segment to the farthest point is searched. If the distance d is less than a threshold d_{tol}, the present points is now a new knot point and the first segment is divided into two new segments at this point. This procedure is performed recursively until all the distances d are less than d_{tol}. This method provides set of N knot points linked by $N-1$ segments.

The result of the polygonal approximation applied to the smoothed example 2D profiles is shown in figures 3.18 and 3.19, respectively. The procedure produces **"at least"** one long segment at the flat primitive in figures 3.18b and 3.19.

(a) No wear

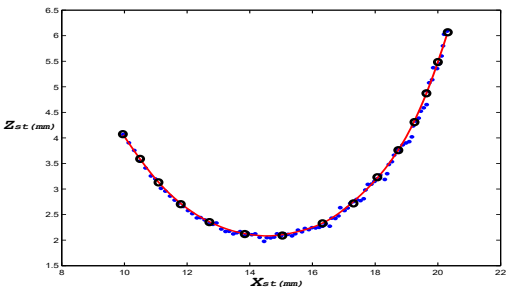

(b) Worn-out

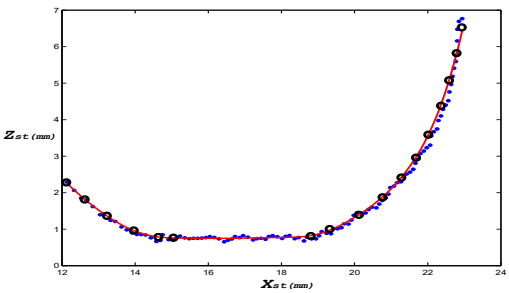

Figure 3.18: Polygonal approximation on the smoothed 2D profile for round wires.

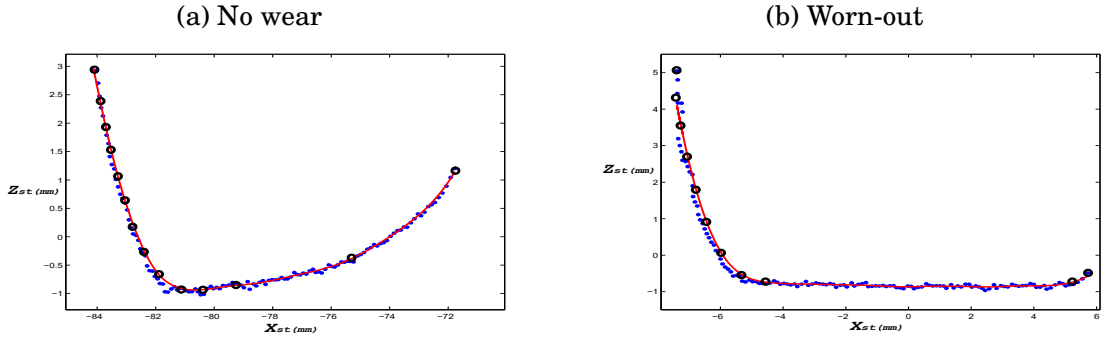

Figure 3.19: Polygonal approximation on the smoothed 2D profile for oval wires.

Let us describe the symbols displayed in table 3.2 that will be used in the rest of this section. We consider N knot points κ where $\kappa_{k=1,\ldots,N}$. The knot points are linked together by line segments S_k so that $S_{k=1,\ldots,N-1}$, and the angle between two consecutive segments is denoted as α_k. A segment S_k is bounded by two extreme knot points κ_k and κ_{k+1}.

Symbol	Description
κ_k	$k-$th knot point, where $k = 1,\ldots,N$
S_k	$k-$th segment, where $k = 1,\ldots,N-1$
α_k	angle between two consecutive segments S_k and S_{k+1}

Table 3.2: Summary of symbols under 2D profile segmentation.

3.2.2.2 Segment regroupement using region growing

We propose to regroup sets of connected segments into regions, thanks to region growing method based on angle criteria. Let us denote two connected line segments S_k and S_{k+1} as shown in figure 3.20. Using the coordinates of their knot points $\{(\kappa_k,\kappa_{k+1})\}$, and $\{(\kappa_{k+1},\kappa_{k+2})\}$, we can determine the angle α_k.

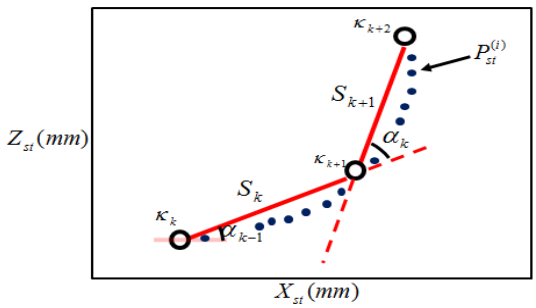

Figure 3.20: Illustration of the symbols under 2D profile segmentation.

The angle α_k is used to group these segments into region R. The region growing criteria states that "if the angle α_k between two consecutive segments is less than a tolerance angle α_{tol}, then these two segments are grouped into the same region". For the example shown in figure 3.20 using S_k, the segment S_{k+1} is grouped into the same region R_j if the criteria is valid. The pseudo code for the region growing method is shown in **Algorithm 1**.

$j = 1, \quad k = 1;$
$S_k \in R_j;$
for *all* S_k, *where* $k \rightarrow 1,\ldots,N-2$ **do**
  determine α_k between S_k and S_{k+1};
  if $(\alpha_k < \alpha_{tol})$ **then**
    $S_{k+1} \in R_j;$
  else
    $j = j + 1;$
    $S_{k+1} \in R_j;$
  end
end
M = j;

Algorithm 1: Region growing of connected segments using angle criteria.

The experimental results on example 2D profiles are shown in figures 3.21 and 3.22. The region growing provides four regions on round profile shown in figure 3.21b, and five regions for the oval profile shown in figure 3.22b. As at present, we do not know if these regions belong to either the arc or flat primitives. The aim of next section will be to determine the identity of these regions using a length criteria.

(a) Before region growing

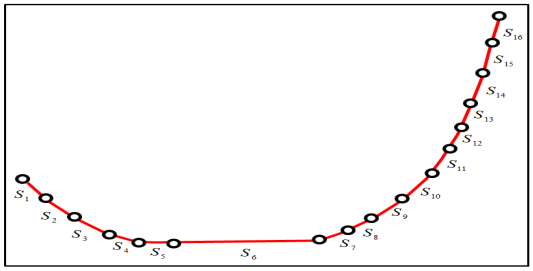

(b) After region growing

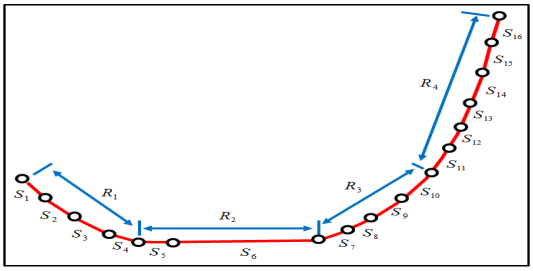

Figure 3.21: Region growing of round 2D profile segments using angle criteria.

(a) Before region growing (b) After region growing

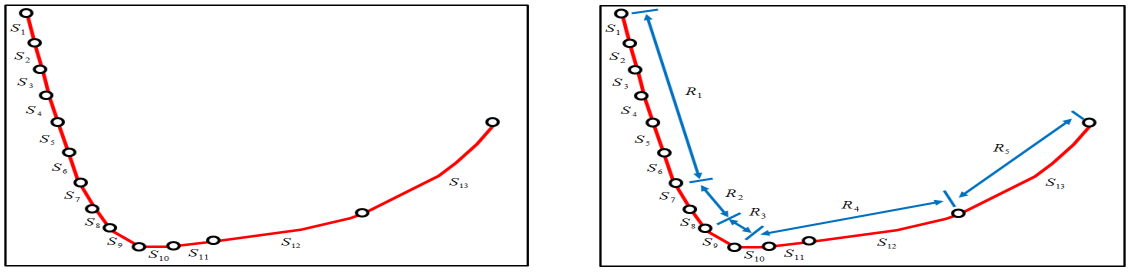

Figure 3.22: Region growing of oval 2D profile segments using angle criteria.

3.2.2.3 Region labeling using length criteria

The objective of this task is to determine the label of the regions. Indeed, any region R_j that contains at least one segment whose length is greater than a threshold value {*dist (mm)*} is labeled as the flat primitive, and therefore considered as the region with the contact wire wear. Whenever there is no segment whose length is greater than {*dist (mm)*}, the region is labeled as arc. The pseudo code for the region labeling procedure using length criteria is shown in **Algorithm 2**. For a particular segment S_k, length $|S_k|$ is the distance between the knot points {κ_k and κ_{k+1}.

```
i=1;
for R_j, where j = 1,...,M do
    for all S_k ∈ R_j do
        if any |S_k| > dist then
            label(R_j) ← Flat;
        else
            label(R_j) ← Arc;
        end
    end
end
```

Algorithm 2: Region labeling using length criteria.

By applying region labeling to round wire example in figure 3.21, all regions $\{R_1, R_3, R_4\}$ are labeled as arc while $\{R_2\}$ is labeled as flat. Likewise for oval wire example in figure 3.22, all regions $\{R_1, R_2, R_3\}$ are labeled as arc while $\{R_4, R_5\}$ are labeled as flat.

Note : For the round wire example in figure 3.21, one can see that the length of segment S_5 is short (i.e $|S_5| < dist$) but has been labeled as flat, thanks to S_6 (with $|S_6| \geq dist$}) which lies in the same region R_2.

3.2.2.4 Point labeling

Once the regions have been labeled, we use these labels to regroup the points into arc and flat sets. Thanks to earlier region labeling procedure, we then use the knot points coordinate that delimit each segment to determine the corresponding point label. At the end of this task, the arc points that belong to both left and right parts of the 2D profile must have the same label, while the flat points will have multiple labels depending on the total number of regions that correspond to the flat region.

In summary, we determine arc points **AP**$\{ (X_{st}^{(i)}, Z_{st}^{(i)}) \}_{i=1}^{m_{arc}}$, where m_{arc} is the total number of arc points. This set contains both the points in the left and right parts of the 2D profile. The flat points are grouped separately since the different regions correspond to different wears. Therefore, flat points **FP** that belong to a flat region R_j are denoted as **FPRj**$\{ X_{st}^{(i)}, Z_{st}^{(i)} \}_{i=1}^{m_{FPRj}}$, where m_{FPRj} is the total number of points in a flat region R_j. The whole segmentation procedure in this section is summarized mathematically as below:

2D profile	$P_{st}^{(i)} = \{ X_{st}^{(i)}, Z_{st}^{(i)} \}_i^m$
$\Downarrow$	
Knot point κ	$\kappa_{k=1,\ldots,N} = \{ X_{st}^{(k)}, Z_{st}^{(k)} \}$ where $N \leq m$ and $\kappa \subset P_{st}$
$\Downarrow$	
Segment S_k	S_k is between (κ_k, κ_{k+1})
$\Downarrow$	
Region R_j	$S_k \in R_j$, where $j = 1,\ldots,M$ $label(S_k) = label(R_j)$
$\Downarrow$	
Point label	$label(X_{st}^{(i)}, Z_{st}^{(i)}) = label(S_k)$, where $X_{st}^{(k)} \leq X_{st}^{(i)} < X_{st}^{(k+1)}$
$\Downarrow$	
Arc points **AP**	**AP**$\{ X_{st}^{(i)}; Z_{st}^{(i)} \}_{i=1}^{m_{arc}}$
Flat points **FP** for R_j,	**FPRj**$\{(X_{st}^{(i)}; Z_{st}^{(i)})\}_{i=1}^{m_{FPRj}}$

The point label result on a round 2D profile is shown in figure 3.23. For this example, we can assume that the points located in the **Flat region** R_2 correspond to the contact wire wear. For the oval profile example shown in figure 3.24, the points located in the **Flat regions** R_4 and R_5 are not the contact wire wear. Indeed, this profile example represents an oval wire with no wear. Due to the weak curvature of the bottom-end of the new oval wire, our cross-section estimation method will regard these regions as wear. This is just a special case that occurs only with oval wire that has no wear.

(a) Arc points (b) Flat points

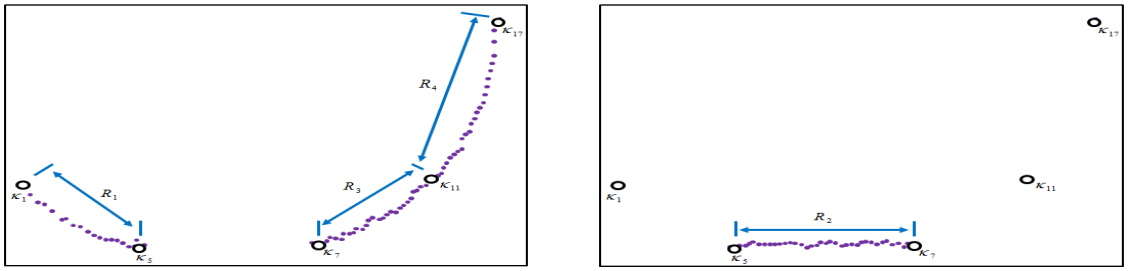

Figure 3.23: Point labeling for round 2D profile.

(a) Arc points (b) Flat points

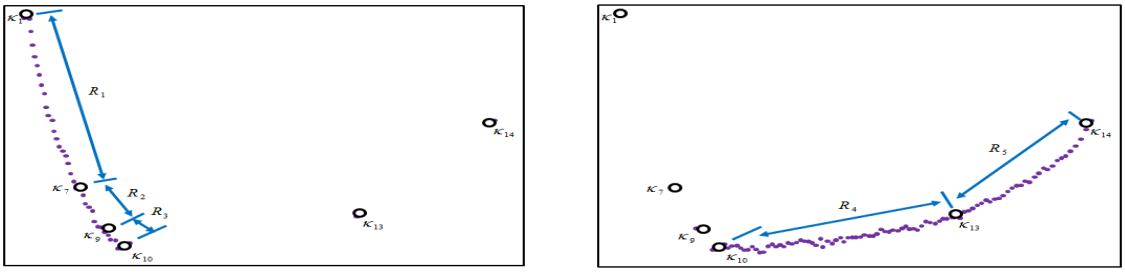

Figure 3.24: Point labeling of oval 2D profile.

3.2.3 Model Fitting

To estimate the cross-section of the wire, we need to fit specific model to the primitive points using circle and line. Therefore, we propose to model the wire by a circle thanks to the arc points and to model each flat region by a line. Figure 3.25 illustrates a circle fit to the arc points of the 2D profile, and two lines fit to the flat points.

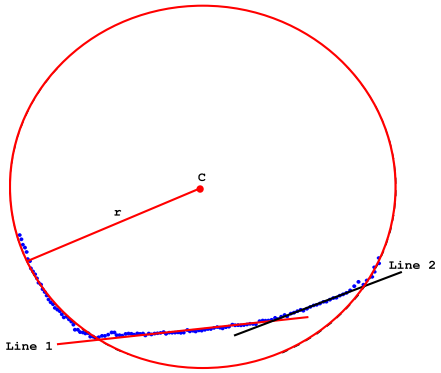

Figure 3.25: Model fitting (Circle and Lines) on the 2D profile points.

3.2.3.1 Circle fitting on arc points

Let us denote the points that belong to the arc region as $\mathbf{AP}(X_{st}^{(i)}; Z_{st}^{(i)})_{i=1}^{m_{arc}}$. We model the wire by a circle thanks to the arc points. The circle model needs 2 parameters, the center coordinate of the circle $c(c_x, c_z)$, and the radius r. The equation of a virtual circle passing through these points is,

$$(X_{st}^{(i)} - c_x)^2 + (Z_{st}^{(i)} - c_z)^2 = r^2 \tag{3.14}$$

To determine the best circle fit on these points, one need to minimize the function $f(.)$, in order to estimate the optimal circle parameters (c_x, c_z, r) as shown below,

$$\begin{aligned} \hat{f}(c_x, c_z, r) &= min \sum_{i=1}^{m_{arc}} \|d^{(i)} - r\|^2 \\ \text{where} \quad d^{(i)} &= \sqrt{(X_{st}^{(i)} - c_x)^2 + (Z_{st}^{(i)} - c_z)^2} \end{aligned} \tag{3.15}$$

$d^{(i)}$ is a (signed) distance from all the points. We need to minimize the above function, i.e. iteratively reduce the distance between the circle and the complete set of points. This is done with the use of Levenberg-Marquardt method (see appendix 7.2.1).

The underlying principle of the circle fitting method with LM is to first determine an initial guess for the circle center (c_x, c_z), and radius r parameters. Although, the r parameter can be initialized using a prior knowledge (also taking into account the wire radius tolerance r_{tol} which is an optional factor in our application), the center parameters (c_x, c_z) are indispensable and can not be known a prior. Therefore, we need to find a way to determine their initial values.

The simplest way to determine these initial circle parameters is by the use of triangle circumcircle theorem method proposed by Maisonobe [60]. In the method, many circles were created using sets of three non-aligned points. The averaging of all the created circles gives the required circle center and radius. One can also use the Landau circle fitting method [49] to initialize the LM minimization procedure. The author uses a fixed-point iterative scheme to solve the nonlinear equations generated from the function $f(.)$ [12, 85].

3.2.3.2 Line fitting on flat points

We need to determine the best line fit to the points located in each flat region. The total number of flat region will determine the number of line fittings required for this task. The equation of a line that passes through these points is given as,

$$Z_{st}^{(i)} = a^{(j)}.X_{st}^{(i)} + b^{(j)} \tag{3.16}$$

where $i = 1,\ldots,m_{FPRj}$, recall that j depends on the number of flat regions. The best fit in the least square sense is to determine the optimal line equation parameters a and b. This is done by minimizing the cost function in equation (3.17).

$$\hat{f}(a,b) = \sum_{i=1}^{m_{FPRj}} \|Z_{st}^{(i)} - (a^{(j)}.X_{st}^{(i)} + b^{(j)})\|^2 \tag{3.17}$$

The result of the model fitting using the circle (c_x, c_z, r) and line parameters $(a^{(j)}, b^{(j)})$ is shown in figure 3.25. In the next sub-section, we will explain in detail the cross-section estimation procedure from the 2D profiles using the optimal circle and line fittings.

3.2.4 Cross-section Estimation

Once the circle representing the wire and the lines associated to the flat regions have been determined, we can estimate the cross-section of the wire. Using the estimated circle parameters (c_x, c_z, r), we determine an optimal virtual circle fitting on the arc points. Likewise, using the line parameters $(a^{(j)}, b^{(j)})$, we determine an optimal line fittings for each flat regions. We have used these line parameters to determine an "infinite" line fits, with start and end point of each fitted line set at infinity.

In order to determine the unimportant part of the circle which has been denoted as "Cut-off" in figure 3.26, we propose to scan a line defined by S_c all along the "Lower circle region" using increasing "step" angle (ρ). At each step angle (ρ), we determine the point of intersection P_p that corresponds to the shortest distance from the circle center c. At the end of this operation, we have m_p number of $P_p(X_p^{(i)}; Z_p^{(i)})_{i=1}^{m_p}$ points that formed the remaining points of the lower circle region (see figure 3.26b).

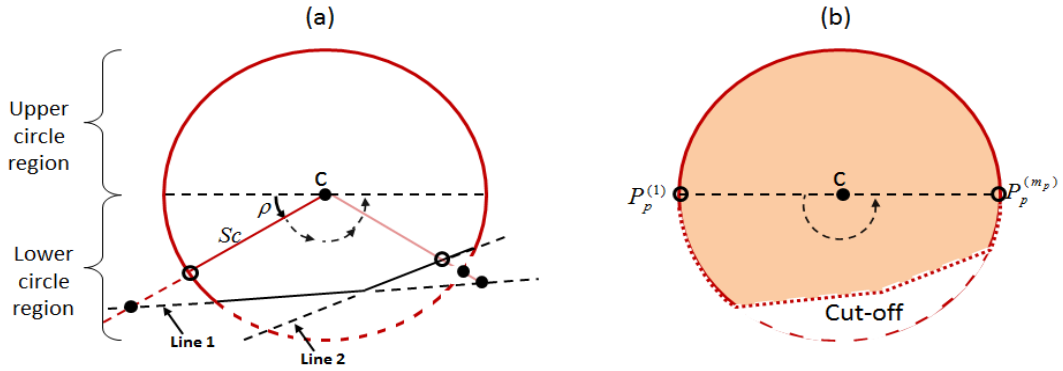

Figure 3.26: Illustration of cut-off circle region under cross-section estimation.

Note that these points P_p have been ordered, and m_p is defined by the increasing step angle ρ. We can determine the upper circle region area using $Area1 = (\pi r^2)/2$, thanks to the estimated radius r in section 3.2.3.1. To determine the area of the lower circle region, we use the determined

coordinate points P_p that have been well ordered. The area of this lower region ($Area2$) is given in equation (3.18). Finally, the cross-section area of the 2D profile is determined using the summation of the upper and lower circle region areas (i.e. CSA = $Area1 + Area2$).

$$Area2 = \| \frac{(X_p^{(1)} Z_p^{(2)} - Z_p^{(1)} X_p^{(2)}) + (X_p^{(2)} Z_p^{(3)} - Z_p^{(2)} X_p^{(3)}) \ldots + (X_p^{(m_p)} Z_p^{(1)} - Z_p^{(m_p)} X_p^{(1)})}{2} \| \tag{3.18}$$

The method used for the cross-section estimation of the lower circle region in equation (3.18) is based on popular approach used to estimate the area of complex polygons. This method will fail when the lower circle region represents a self-intersecting polygon (such as convex polygon). In our application, we do not have to worry about this problem because we are guaranteed to always have a concave polygon, thanks to the proposed cross-section estimation method.

The full algorithm to estimate the cross-section area of the contact wire from its 2D profile is summarized as follows,

1. **Pre-processing :** Eliminate isolated noisy points and possible points that belongs to the notch part of the contact wire,
2. **Smoothing :** Smooth the 2D profile using the Kernel Smooth Regression (optimal bandwidth h parameter),
3. **Segmentation :** Classify the 2D profile points into the arc and flat labels,
   - Approximate the 2D profile by segments using Kramer-Douglas-Peucker method (optimal d_{tol} parameter),
   - Group the segments into regions R using angle criteria (optimal α_{tol} value),
   - Label the regions using length criteria,
   - Assign the points into arc or flat labels.
4. **Model fitting :** Fitting of lines and circle on the geometry primitives of the wire profile,
   - Fit a virtual circle on the arc points,

     Note : For the **optional case** where the prior value of the radius is given, the LM algorithm is adjusted to optimize the radius between a given tolerance value r_{tol} that is given by the user,
   - Fit lines to the flat points depending on the total number of flat regions
5. **Cross-section :** Estimate the cross-section of the contact wire,
   - Determine the points P_p that form the remaining circle points at the "lower circle region" (see figure 3.26),

- Estimate the cross-section area of the upper circle region using $(\pi r^2)/2$, and the lower circle region using equation (3.18)

3.3 Experiments and Results

The experiments have been performed on synthetic 2D profiles that have been generated with the use of a software tool developed under the project. This tool is based on Scheimpflug set-up, and simulates various tasks such as the creation of different wire profiles, the laser calibration pattern, as well as their image formation, with and without speckle noise addition.

We have only simulated BC-150 round wire type for this experiment. The wires have been placed in the center of the camera's focus plane O_{st}. We generate four different cases of the wear profile shown in figure 3.27. Figures (a-c) are the wires with no wear, horizontal wear, and inclined wear that has been rotated at approximately 7.5°. Figure (3.27)d shows the wire with two wear segments, which we denote as double wear.

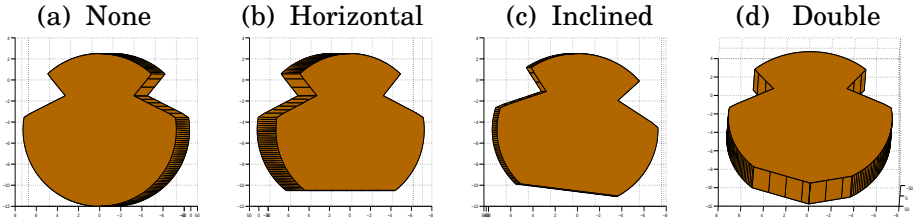

Figure 3.27: Generated wire profiles using the simulation tool.

3.3.1 Evaluation Condition

In order to evaluate the system capability, we have generated different sources of error in the software tool, through **speckle noise** addition and **reprojection error** from simulated laser-camera calibration. The speckle noise has been added in the simulated images to represent the perturbations of contact wire surface aspect (see section 3.1.1.3).

To simulate the **reprojection error**, we have generated the synthetic laser calibration target, then applied the laser calibration technique that gives mean reprojection errors ($err =$ 0.015 and 0.060mm). The error proportion ($err = 0.060mm$) corresponds to the error from the state of art calibration method [109] under classical calibration method, while the error proportion ($err = 0.015mm$) has been reached by our application. Indeed, we added a constant value to each coefficient of the laser-camera homography $\mathscr{H}_{st}$ (see section 2.3) so that the mean reprojection error computed using the feature points of the simulated target is equal to 0.015 and 0.060 respectively, as shown in equation (3.19). Thus for the case of perfect calibration, the mean reprojection error is zero so that ($err = 0mm$).

$$\sum_{i=1}^{n} \|p_t^{(i)} - \hat{\mathscr{H}}_{st}\hat{P}_{st}^{(i)})\|^2 + \|P_{st}^{(i)} - \hat{\mathscr{H}}_{st}^{-1}\hat{p}_t^{(i)})\|^2 = 0.015 \text{ and } 0.060mm \tag{3.19}$$

3.3.2 Results

We have made two separate tests for the cross-section estimation. For the first test, we do not include a prior knowledge of the contact wire radius in the optimization procedure. Furthermore, we include this information in the second test to show the importance of this parameter. Table 3.3 shows the full parameters of the proposed cross-section method that have been used for the subsequent experimental tests.

	Symbol	**Value**	**Description**
Profile determination	-	1	To remove background noise
	σ	12	Gaussian filter
Profile analysis	h	0.3	KSR bandwith
	d_{tol}	0.05	Douglas Peucker threshold
	α_{tol}	13 (°)	Region growing angle criteria
	$dist$	2.5 (mm)	Length (Wear) criteria
	r_{tol}	0.2 (mm)	Wire fabrication tolerance

Table 3.3: The cross-section estimation parameters.

3.3.2.1 Without prior

We estimate the cross-section without any prior knowledge of the contact wire radius, and the outcome is shown in table 3.4. Although ($err = 0$) assumes a perfect calibration, there is addition of speckle noise, and the system only identifies a small arc of the full wire profile. This is because the proposed system does not observe the full wire.

Wear type	**True** CSA (mm^2)	**CSA Estimation** (mm^2) (err**=0mm**)	(err**=0.015mm**)	(err**=0.060mm**)
None	164.9852	165.4331	165.9895	**172.8922**
Horizontal	155.9946	157.6635	158.2785	**161.6090**
Inclined	156.0601	157.7593	157.1029	**174.2254**
Double	160.2345	161.9024	162.7839	**169.3124**

Table 3.4: Experimental result for CSA estimation in the presence of laser-camera calibration error, and without prior wire radius knowledge.

We have defined a measurement tolerance value of 3mm^2, and is used to evaluate the system. From the result table, we can see that the difference between the true and estimated CSAs is lower than 3mm^2, at table columns with ($err = 0mm$) or ($err = 0.015mm$). The cross-section

estimation results for the column ($err = 0.060mm$) are outside the 3mm^2 tolerance value, and thus unacceptable. Indeed, the reconstructed 2D profiles have been largely deformed as a result of the larger calibration reprojection error.

3.3.2.2 With prior

For the second test, we have decided to include the prior knowledge of the radius (r_{cw}) and the tolerance (r_{tol}) given by the wire's manufacturer ($r_{cw} \pm r_{tol}$). With the use of Levenberg-Marquardt optimization, we are able to better fit a circle on the arc points. This is done by optimizing the circle parameters within the wire's radius tolerance. Using this prior radius information, the method is able to improve the quality of the CSA estimation as shown in table 3.5.

Wear type	**True** CSA (mm^2)	**CSA Estimation** (mm^2)		
		(err=0mm)	**(err=0.015mm)**	**(err=0.060mm)**
None	164.9852	165.0679	165.2691	**166.5947**
Horizontal	155.9946	156.4317	156.5748	**157.9381**
Inclined	156.0601	156.0273	155.5954	**157.3299**
Double	160.2345	161.6704	161.5415	**163.2014**

Table 3.5: Experimental result for CSA estimation in the presence of laser-camera calibration error, and with prior wire radius knowledge.

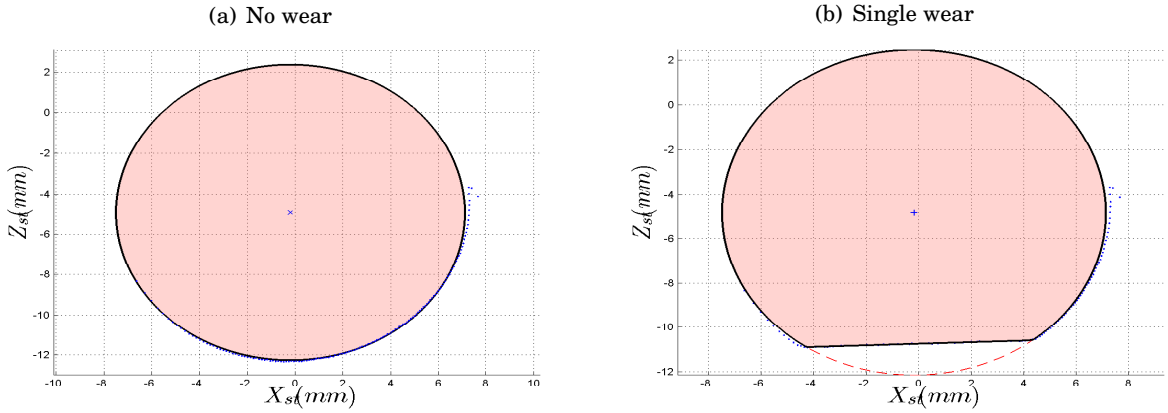

Figure 3.28: Cross-section estimation on synthetic 2D profile with prior radius. The profile has been perturbed with speckle noise, and calibration reprojection (**err=0.060mm**). The raw points are in blue "dot" color (.), while the approximated CSA plot is in black "line plot" (-). The approximated cross-section area plot does not pass through all the 2D profile points (see between X_{st} $6.5-8.5mm$) due to reprojection error.

With large calibration error ($err = 0.060mm$), the use of prior radius information is required. This is because the 2D profiles have been largely deformed and possibly lost some of its circular properties, especially at the two extreme ends of the curve as shown in figures 3.28 and 3.29

respectively (see between X_{st} $6.5-8.5mm$). The use of this prior information allows to reach a better fit that converges to the prior radius knowledge ($r_{cw} \pm r_{tol}$).

(a) Single wear (rotation)

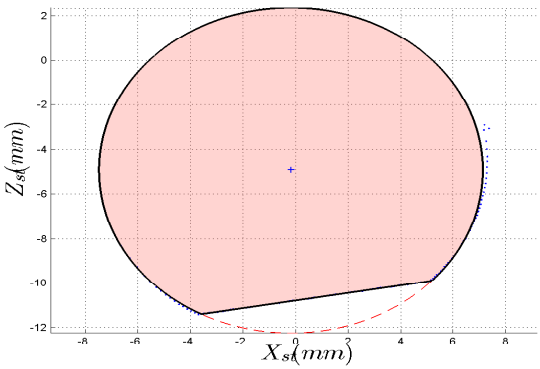

(b) Double wear

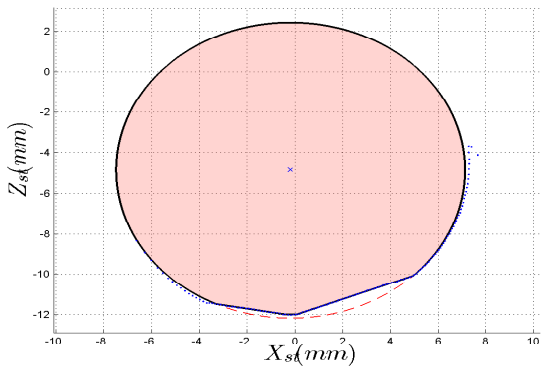

Figure 3.29: Cross-section estimation on synthetic 2D profile with prior radius. The profile has been perturbed with speckle noise, and calibration reprojection (*err*=**0.060mm**). The raw points are in blue "dot" color (.), while the approximated CSA plot is in black "line plot" (-). The approximated cross-section area plot does not pass through all the 2D profile points (see between X_{st} $6.5-8.5mm$) due to reprojection error.

3.4 Conclusion

In this chapter, we have introduced a new method to determine the cross-section of contact wires. The procedures are grouped into two main successive steps, which are the profile determination and profile analysis. Profile determination consists in determining the reconstructed profile, called 2D profile. This is done by extracting the laser stripe centers from the image, followed by transforming these stripe centers to the reconstructed 2D profile using triangulation technique. The profile is modeled by a set of segments that are classified into arc and flat primitives. The points that delimit arc segments are used to fit a circle that represents the contact wire. The flat segments are used to identify possible wear which finally contributes to the estimation of the contact wire's cross-section.

For the laser stripe extraction, we have combined the use of Gaussian filter and sub-pixel interpolation techniques. This combination provides the possibility to deal with speckle and Gaussian noises that corrupt the acquired images of the contact wire. Experimental tests have shown that the use of Gaussian filter with parabolic fitting is the best choice for our application. We have only focused on one dimensional laser stripe extraction technique whose processing time is low.

The resulting 2D profile from laser-camera triangulation technique is mostly noisy and irreg-

ular due to the noise perturbations of the contact wire images. The proposed system placement in this work does not allow us to analyze the full contact wire profile (incomplete profile). The main idea of the proposed profile analysis method is to approximate these irregular and incomplete profiles in order to get meaningful information that will help in the cross-section estimation. For this task, we use a smoothing method to eliminate some irregularities in the 2D profile, followed by a polygonal approximation method to represent the profile by segments. Next, we proposed a region growing method based on angle criteria to regroup these segments into regions. This allows to separate the arc and flat regions, and we consider that any long segment (e.g. $dist >$ 2.5mm) is regarded as a wear.

We have experimentally verified the proposed method using a software tool developed under the project. The software tool completely simulates the Scheimpflug image formation as well as the proposed system placement in this work. Few error quantities have been added on the camera -laser plane homography. Indeed, this experiment allows us to globally analyze the influence of calibration error in this work. An important conclusion from this test is that in the case of large calibration error (err= $0.060mm$), the cross-section estimation results are very bad. Therefore, it is important to use prior knowledge of the contact wire radius so that the solution searches for better radius in the given tolerance.

The cross-section estimation accuracy is also influenced by the number of arc points. The higher the number of arc points, the more accurate the cross-section estimation. Another important observation is that the cross-section estimation result is better when arc points are available in the left and right parts of the 2D profile. These experimental tests have allowed us to validate the system, from calibration to cross-section estimation using the software tool. In the next chapter, we will show more experiments of the system applied to plug gauges, and real contact wires.

CHAPTER 4

EXPERIMENTS AND RESULTS

In this chapter, we present our experimental test in an orderly organization. For each experiment, we describe encountered problem and the proposed adjustment on the system prototype, before continuing with the subsequent experiments. This form of experimental organization helps the reader to understand various issues of cross-section estimation under Scheimpflug set-up.

The experiments have been divided into two kinds of test, validation and contact wire tests. For the first test, we validate the prototype by inspecting a full and worn plug gauges, that have been placed along the measurement area. For the second test, the system inspects real contact wires with various challenging conditions. These wires have been chosen by SNCF representatives.

4.1 Validation Test

To determine the system accuracy, the CSA of two known plug gauges placed in the measurement area has been estimated. The first gauge does not have any wear, while the second one contains a simple (horizontal) wear. The plug gauge has been fixed at each position [**11, . . . , 45**] in the measurement area shown in figure 4.1. Position [**33**] corresponds to the focus plane of the camera, which is the origin O_{st} of the laser calibration target. The system is located somewhere to the downward-left of the measurement area, which means that position [**41**] is the closest to the system while position [**15**] is the furthest. This experimental set-up allows us to cover the depth of field extremities at the boundaries of the measurement area.

For each position, we acquire several images, from which we estimate the CSA of the observed

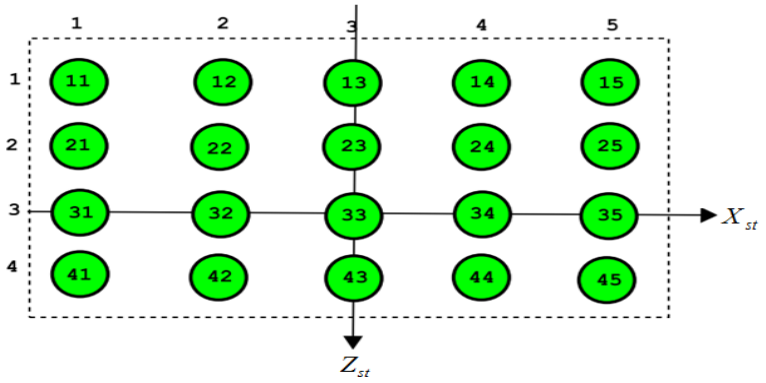

Figure 4.1: Experimental set-up for the system validation test.

plug gauge. Let us denote S_μ and S_σ as the mean and standard deviation of measured CSAs, respectively. According to the project specification, the standard deviation of the CSA estimation error should be lower than $3mm^2$ for 95% of the cases. Let us define CSA as the true section of an object (e.g. full plug gage has a CSA of 134.3709 mm^2), and the tolerance error $\sigma_{tol} = 3mm^2$ defined by SNCF. The **tolerance interval** on the cross-section estimation for the full plug gauge is given as follows,

$$\begin{aligned} S_\mu - 2S_\sigma \geq CSA - \sigma_{tol} \quad \text{and} \quad S_\mu + 2S_\sigma \leq CSA + \sigma_{tol} \\ S_\mu - 2S_\sigma \geq 131.3709mm^2 \quad \text{and} \quad S_\mu + 2S_\sigma \leq 137.3709mm^2 \end{aligned} \tag{4.1}$$

4.1.1 Full gauge

The first test object is a full gauge without any wear, whose radius is $6.54mm$, and gives a nominal section (ground-truth) of $134.3709mm^2$. In this experiment, we have painted the head of the gauge undergoing inspection in order to avoid surface aspect problem (see figure 4.2).

Figure 4.2: Painted plug-gage head to eliminate surface aspect problem.

We make acquisition of the gauge at every position [**11, . . . , 45**] on the measurement area as shown in figure 4.1. We have approximately 150 reconstructed profiles at each position. The

experimental results are summarized in table 4.1, using the mean cross-section S_μ, and the standard deviation S_σ of the measures.

L \ C	**1**	2	3	4	5
1	(S_μ) 134.2933	135.7635	135.5388	134.7756	136.4004
	(S_σ) 0.2135	0.2531	0.1872	0.2997	0.5298
2	135.0144	133.8339	136.1882	135.4257	136.0150
	0.1879	0.1942	0.0986	0.1611	0.3589
3	135.1398	134.6263	134.8745	134.8215	135.6103
	0.0981	0.0575	0.0767	0.0928	0.1718
4	134.1915	134.3212	134.7269	134.6850	135.2124
	0.2279	0.1454	0.2100	0.0858	0.1409

Table 4.1: Full gage - Experimental result table of S_μ and S_σ for each gauge positions. The measurement at position [**15**] (in red font) is outside of the tolerance interval.

By analyzing the result in table 4.1, one can see that the cross-section measure at position [**15**] is clearly outside of the tolerance interval, while position [**25**] is just slightly inside of it. This problem has been analyzed, and it is due to low depth of field at these positions on the measurement area, which leads to blurry images of the plug gauge. Thanks to the outcome of this test, we refocus the camera so that the depth of field plane is re-positioned to cover the positions [**15**], and [**25**]. This will improve the images of the plug gauge at these positions, and thus improve the cross-section estimation.

4.1.2 Worn gauge

The outcome of earlier full gauge test has allowed us to move the camera's focalization plane so that the images of the gauge acquired at positions [**15**] and [**25**] are less blurred. This has been done under prototype adjustment task of the Camescat project. For this new test, we use a worn-out gauge with a simple wear that is homogeneous all along the gauge surface. The gauge has a radius of 6.42±0.08mm, wear width of 3mm, which gives a cross-section (Ground-truth) of approximately 120.1217mm^2. We have followed the same experimental procedure under **Full gauge** test, but with a re-positioned camera's focus plane. From the experimental result shown in table 4.2, we can see that all the measures at positions [**11, . . . , 45**] fall within the tolerance interval.

L \ C	1	2	3	4	5
1	119.4289	120.1438	122.2315	121.6541	122.3588
	0.1735	0.1623	0.1955	0.1952	0.2423
2	120.2001	119.9023	119.9213	120.2146	121.9562
	0.0851	0.0815	0.0902	0.1023	0.1891
3	120.1856	119.5689	119.9128	119.9502	120.2145
	0.0612	0.0547	0.0605	0.0756	0.0914
4	119.2564	119.4859	119.7589	119.5698	120.1852
	0.1012	0.0953	0.1059	0.1332	0.1789

Table 4.2: Worn gage - Experimental result table of S_μ and S_σ for each gage positions after system adjustment. All measurements are in the tolerance interval.

4.2 Contact Wire CSA Measurement

Ten contact wire samples have been used for this experimental test. Few examples of the contact wire samples are shown in figure 4.3. Figures (a-b) show new contact wires that still maintain their high reflectance property. However, figures (c-d) show old wires with small and large wears, respectively. These wires have been darkened as a result of their daily use on the SNCF network.

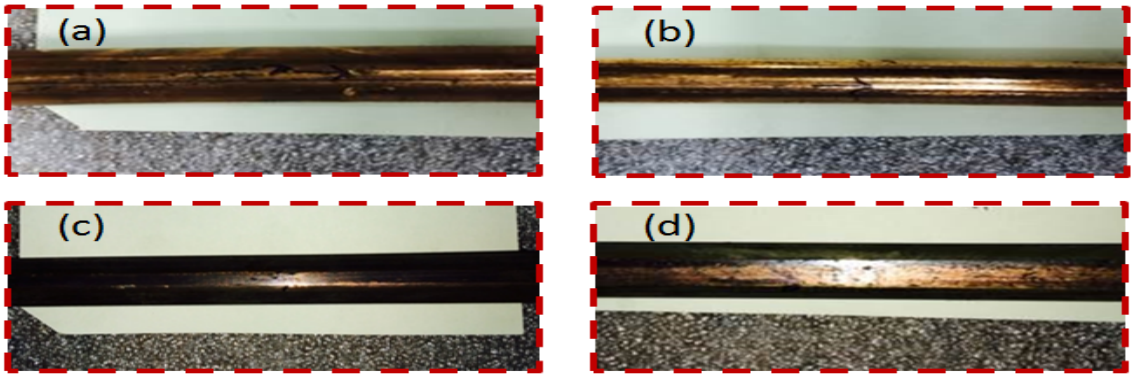

Figure 4.3: Few examples of the contact wire samples for dynamic test(a-b) Shiny BC-150 and 107, (c) dark pitted BC-120, and (d) greasy BC-120.

The contact wire samples used in this experiment have been numbered by their name ($Wire\ 30,\ldots,39$). For each contact wire samples, the true thickness T_{cw} and the wear width W (if any) have been determined by SNCF representatives, with the use of independent measurement tool (digital vernier caliper) with measurement tolerance of ± 0.08mm. The ground-truth cross-section areas have been estimated without excluding the notch area. The contact wire characteristics are summarized in table 4.3. They consist of contact wires with different surface aspects and presence of moderate grease.

				Values		
			Aspect	W (mm)	T_{cw} (mm)	CSA (mm^2)
Round	BC-150	Wire 30	shiny	-	14.50	166.27
		Wire 33	dark	-	14.59	167.18
		Wire 34	dark	-	14.52	165.58
	BC-120	Wire 35	dark	4	12.54	117.2841
		Wire 36	grease	11	9.73	111.2716
		Wire 37	grease	<2	12.76	123.1435
	BC-107	Wire 31	shiny	-	12.3	118.82
		Wire 32	shiny	-	12.12	115.37
Flat	BC-107	Wire 38	grease	-	11.35	≈119
		Wire 39	grease	-	11.35	≈119

Table 4.3: Characteristics of the contact wire samples used for the measurement.

For the experimental test, we allow the contact wires to move freely in the measurement area (No fixed placement), and the camera acquires the images of the contact wire that has been directly illuminated by the system laser.

4.2.1 Results and Discussions

We calibrate the system, and our procedure determines the cross-section of the wires. The system is evaluated using the mean S_μ, maximum S_{max}, minimum S_{min}, and standard deviation S_σ of the system measures. The experimental results are summarized in table 4.4. The second column of the table corresponds to the total number of profiles analyzed for the tested contact wire sample.

	nb. profiles	**CSA (mm^2)**	**Estimation (mm^2)**			
			S_μ	S_σ	S_{min}	S_{max}
Wire 30	421	166.2700	167.301	0.740	164.31	171.813
Wire 33	515	167.1800	167.184	1.025	159.892	174.509
Wire 34	303	165.5800	166.741	1.397	154.314	175.481
Wire 35	424	117.2841	119.916	1.223	115.194	128.194
Wire 36	333	111.2716	112.113	1.328	102.973	118.099
Wire 37	433	123.1435	124.3698	0.734	119.912	127.678
Wire 31	539	118.8200	118.245	0.891	113.275	124.758
Wire 32	511	115.3700	118.161	0.936	112.262	124.481
Wire 38	412	≈119.0000	118.312	1.177	119.121	125.012
Wire 39	230	≈119.0000	118.512	1.355	118.951	125.223

Table 4.4: Measurement result using the contact wire samples.

The outcome of this test on these contact wire samples is encouraging. For all the wires tested, the standard deviation $2 * S_\sigma$ is well below the 3mm^2 defined in the project specifications. It is a

decent result considering that these wires are under challenging conditions. These experimental results help to validate the system prototype from calibration to cross-section estimation.

We show in figure 4.4 and 4.5 some cases where the cross-section are well estimated, and thus in the given radius tolerance. This is the case where the estimated cross-section is very close to the mean section S_μ in earlier table 4.4. Indeed, we can see that the reconstructed profile points are not very noisy. This ensures that the proposed cross-section estimation procedure works well on these profiles. For each profile in the figures, we plot the notch point (if visible), the virtual circle passing through the profile points, and also the estimated circle center (i.e. wire center).

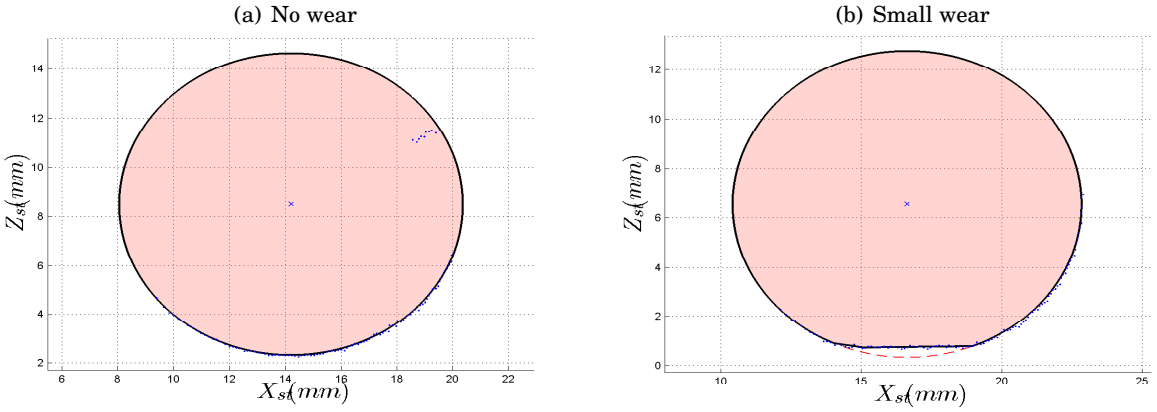

Figure 4.4: Cross-section estimation on round contact wire samples. The CSA is well estimated for these example profiles.

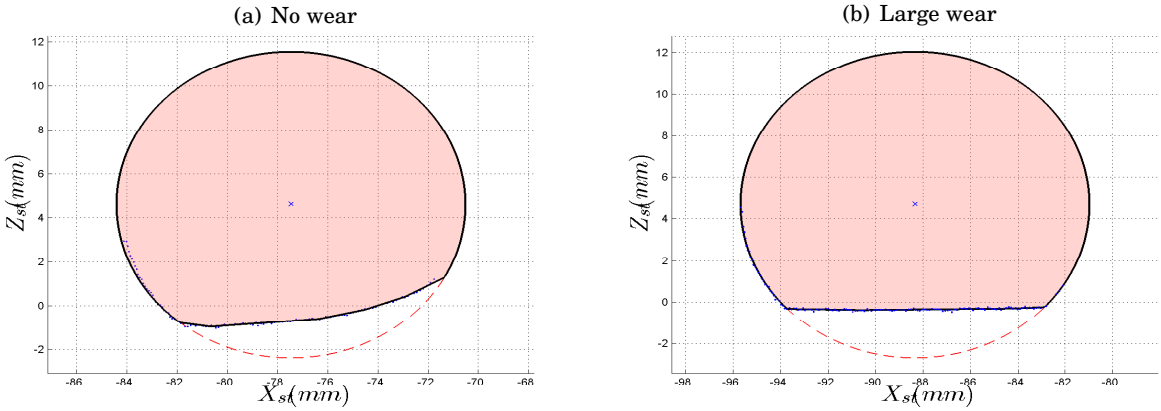

Figure 4.5: Cross-section estimation on oval contact wire samples. The CSA is well estimated for these example profiles.

We show in figure 4.6-4.7 some cases where the estimated cross-section is bad. For these cases, the estimated cross-section is either larger or smaller than the cross-section of the sample contact wire (for example maximum S_{max} or minimum S_{min} in earlier table 4.4). The method

gives bad result mainly because the proposed 2D profile segmentation procedure (see section 3.2.2) does not provide satisfying result. This leads to wrong determination of the arc and flat primitives, which eventually affects the accuracy of the cross-section estimation.

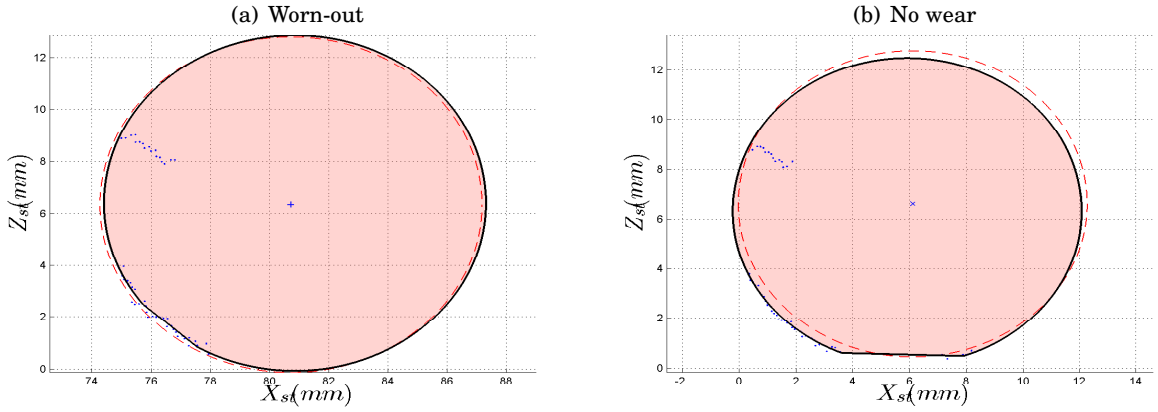

Figure 4.6: Bad Cross-section estimation on the contact wire samples with noisy 2D profile.

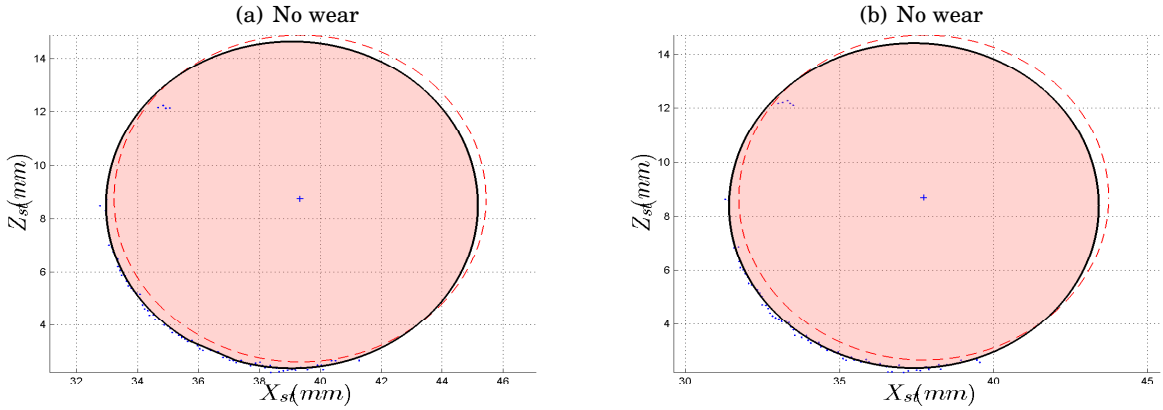

Figure 4.7: Bad Cross-section estimation on the contact wire samples with noisy 2D profile.

The unacceptable cross-section estimation is caused by the grease deposit that deforms the contact wire shapes, and other form of perturbations from its surface aspect. Whenever the laser is projected on the contact wire with very challenging surface aspect, they produce weak reflection which leads to low signal to noise ratio. The end result of these problems is a very noisy 2D profile as shown in figures 4.6 and 4.7. We summarize the problems in those figures as below,

Figure 4.6a : In reality, the contact wire sample used for this test has a wear. From the figure, the wear should be at position (X_{st} : **78 - 84**). However, due to the weak reflection of the projected laser to the viewing camera, the very noisy reconstructed profile that deforms the expected wear location. Therefore, the cross-section estimation method assumes that the contact wire has no wear.

Figure 4.6b : In reality, the contact wire sample used for this test has no wear. Due to weak reflection of illumination on the wire's surface, there is missing reconstructed points at position (X_{st} : **3.5 - 7.2**). Our cross-section estimation method thus deduces that there is a wear at this position. This leads to a smaller cross-section area than it really is.

Figure 4.7a : In reality, the contact wire sample used for this test has no wear. As a result of noisy profile points, it is difficult to accurately determine the arc and flat points. Therefore, our cross-section estimation method deduces that there is a tiny wear at position (X_{st} : **35.2 - 38.2**), which leads to estimated smaller cross-section area compared to the ground-truth.

Figure 4.7b : The contact wire sample used for this test has no wear, and has a better surface aspect compared to the wires used in the earlier figures (4.6a-b, 4.7a). Due to very noisy profile points, the cross-section estimation method does not succeed in fitting optimal circle to these points. This leads to a larger estimated circle radius, and thus larger cross-section.

4.3 Conclusion

In this chapter, we have made various tests to evaluate and validate the proposed measurement system. The system calibration has also been evaluated directly from the cross-section estimation outcome using plug gauge with known cross-section area. The outcome of these tests has allowed proper adjustment of the system prototype to regulate the depth of field problem in order to reach an accurate system placement.

For the validation test, we use plug gauges (with and without wear) that are placed in a static manner along the measurement area. The CSA measured by the proposed system is closer to the true one, and the estimated CSA is in the tolerance defined by SNCF. For the tests on contact wires, we use real wire samples that have challenging aspect surface problems. The wires move freely in measurement area during the image acquisition. The CSA results are in the measurement tolerance, which is sufficient to quantify a contact wire 3D measurement system.

For all the experiments in this section, the laser illumination has been fixed and made homogeneous stripe all along the measurement area. The source of possible failures in the proposed cross-section estimation method results from the contact wire's surface aspect. Too much grease on the wire surface completely deforms the 2D profile shapes, highly dark pitted surfaces have weak reaction to the system laser and thus produce low intensity images. Also, frequent change of the contact wire's position in the measurement area provides specular and speckle effect so that signal to noise ratio in the acquired image is very low. Moreover, when these perturbations are too strong, the method does not succeed in correctly determining the wear.

The experimental results using the contact wire samples provided by the SNCF representa-

tives show that the proposed system is able to reach the goal of measurement tolerance defined in the project specifications. So, the measurement result is acceptable for measurements under metrology application.

CHAPTER 5

CONCLUSION AND PERSPECTIVES

5.1 Contributions

In this PhD thesis, we have demonstrated through various studies and experiments our contribution about computer vision approach for measuring the cross-section area of the contact wires. The major drawback of the state of art Contact Wire Wear Measurement Systems is that they measure the wire wear using 2D image processing. Therefore, we have proposed a Contact Wire Wear Measurement System that measures the cross-section of any contact wire using 3D computer vision technique. We have proposed a system that is composed of laser planes and cameras. In order to reach the measurement accuracy of the specifications, the spatial resolution of the acquired images has to be high. So, we require high number of cameras to cover the whole of the contact wire displacement in the measurement area. However, the number of cameras is limited because of the weight constraint, cost factor, and other security reasons. In order to avoid this problem, an industrial member of the CaMeSCat project has proposed the use of Scheimpflug optical device to increase the field of view of the cameras while reducing their Depth of field. The Scheimpflug device is made up of a camera and a special optical lens which ensures that the sensor plane is tilted at double angles with reference to the camera's optical axis, to form a non-classical optical set-up. This has been explained in the chapter 1 of the thesis.

To provide relevant dimensional measures of contact wire, the developed system has to be calibrated. The system calibration process under Scheimplug set-up is detailed in Chapter 2. It is a two-step calibration procedure that first estimates the intrinsic parameters of the Scheimpflug device, then determines the laser plane parameters in the calibrated camera coordinate system. We have proposed two methods for the intrinsic calibration. The first method is based on estimating the optimal Scheimpflug angle that causes the distortions, and finally removes them

before performing the calibration. The second method uses lens distortion model to deal with the Scheimpflug angle distortions, and this approach provides the best result from experimental tests. For the laser calibration, we have proposed a method that determines the laser plane parameters from just a single image of the calibration target. The accuracy of the system calibration has been evaluated on both synthetic and real data acquired with a Scheimpflug device. The calibration result for the real data test provides a mean reprojection error between 0.020mm and 0.015mm. This is a significant improvement on the calibration error compared with those provided by the state of art laser-camera triangulation system.

Our method that estimates the cross section of contact wires directly from their acquired images is fully described in Chapter 3. First, we use a laser stripe extraction method to determine the pixels that correspond to the laser line profile projected onto the contact wire. Thereafter, these pixels are transformed to the 3D profile by triangulation. Finally, a profile analysis method is proposed to determine the cross-section of the contact wire. The proposed laser stripe extraction method can process large number of images in one second, which is suitable for real-time implementation. In Chapter 4, we demonstrate the capability of our system on real conditions. We have tested the full system on plug gauge and challenging contact wire samples. The experimental results show that the proposed system is suitable for 3D measurement under railway application, and thus validate our contribution.

5.2 Perspectives

To get a full representation of the contact wire profile, full industrial system is composed of several cameras and lasers. A sub-system has 2 cameras (left and right cameras) and 2 lasers (left and right lasers), and each camera observes the contact wire from two different sides (left and right sides). This means that a sub-system provides two images at a time instance and hence 2 half profiles in order to form a multiple view representation of the observed contact wire. Presently, the results presented in this report are based only on the analysis of 1 half profile of the sub-system. In the remaining part of this section, we discuss the issues of merging the two half profiles and other issues that can arise in the future deployment of the system on the railway network.

5.2.1 Profile Merging

By combining the 2 half profiles from the different views of the sub-system, we expect to improve the accuracy of the cross-section estimation. The main question is how to develop the best profile merging approach. Thanks to the proposed laser calibration procedure, we can determine a transformation matrix between the left and right cameras that provide the 2 half profiles. This transformation matrix is used to rectify the right image plane so that it lies in the same coordinate system as the left image plane.

As the operating speed of the train will be increased to 120km/h in the future, the image plane rectification may not necessarily solve other external vibration problems that will impact the alignment of the two half profiles. In the future research aspect, one will need to propose a robust **profile rectification** on the two half profiles. The idea will be to determine a slight rotation and translation needed to improve the alignment of these profiles. The 2D profile segmentation step that has been proposed under the system cross-section estimation method will be an indispensable information for this future work.

For future work, one will need to explore a suitable strategy for merging the two half profiles. This can be considered as a problem of the fusion of data provided by different sensors. One can expect that the fusion procedure may deal with noisy or incomplete half profiles. Moreover, the overhead system contains several contact wires that may hide or be close to the inspected one. Therefore, a multi-view analysis should avoid contact wire occlusion.

5.2.2 Large Scale Measurement

The real measurement tests have been performed on railway test zone with homogeneous wear. To prepare for the future deployment of the system on the railway network where large scale measures will be accumulated for a long time. We will need to address engineering issues related to measurement loss due to possible image loss or laser power fluctuations, aberrant measures and image compression method.

Under large scale measurement, the contact wire wear is assumed to be homogeneous all along the railway network undergoing inspection. Whenever there is a too strong variation between successive dimensional measures, the system should filter them thanks to approach such as Kalman and particle filters.

5.3 Generalization to other applications

The concepts presented in this dissertation are not only applicable to the railway industry, but can also be generalized to other applications. The intrinsic camera calibration method can be used for calibration problem in close range inspection under Particle Image Velocimetry (PIV), and can inspire any other non-classical geometric system calibration. Our work has demonstrated, and analyzed the depth of field issues under Scheimpflug set-up. We have done various experiments and comparison between state of art calibration methods dedicated to 3D reconstruction system. We also deal with the issue of moderate refractive distortion since the cameras are embedded in a thick glass housing. From various experimental tests and outcome, we assume that the idea of iterative bundle adjustment using fronto-parallel seems as a relevant way to deal with moderate refractive distortions.

The proposed system is suitable for accurate 3D measurement (Metrology) of objects with disturbing surface aspects. The proposed system can be further generalized to other industrial

applications such as automotive and aerospace for dimensional measurement and quality control tasks.

CHAPTER 6

APPENDIX A

6.1 Homography estimation

For n number of points for a pose of the calibration target, we can estimate the homography $\mathscr{H}$ using Direct Linear Technique (DLT). However, a data normalization step before applying the DLT technique is required so that the result will be invariant with respect to arbitrary choices of the scale and coordinate origin. This is known as normalized DLT in [35].

In the subsequent explanations, we assume that the feature points P_w in the world coordinate and pixels p in the image coordinate have been normalized. The direct transformation is then,

$$\lambda p = \mathscr{H} P_w$$

$$\lambda \begin{bmatrix} u^{(i)} \\ v^{(i)} \\ 1 \end{bmatrix} = \begin{bmatrix} h_{11} & h_{12} & h_{13} \\ h_{21} & h_{22} & h_{23} \\ h_{31} & h_{32} & h_{33} \end{bmatrix} \begin{bmatrix} X_w^{(i)} \\ Y_w^{(i)} \\ 1 \end{bmatrix} \tag{6.1}$$

To solve for the homography, we need to have n number of features ($n \geq 3$) for a single pose of the calibration target. One can then write linear equation so that "$Lb = 0$" as shown in equation (6.2).

$$\begin{bmatrix} X_w^{(1)} & Y_w^{(1)} & 1 & 0 & 0 & 0 & -u^{(1)}X_w^{(1)} & -u^{(1)}Y_w^{(1)} & -u^{(1)} \\ 0 & 0 & 0 & X_w^{(1)} & Y_w^{(1)} & 1 & -v^{(1)}X_w^{(1)} & -v^{(1)}Y_w^{(1)} & -v^{(1)} \\ \cdot & \cdot & \cdot & \cdot & \cdot & \cdot & \cdot & \cdot & \cdot \\ \cdot & \cdot & \cdot & \cdot & \cdot & \cdot & \cdot & \cdot & \cdot \\ X_w^{(n)} & Y_w^{(n)} & 1 & 0 & 0 & 0 & -u^{(n)}X_w^{(n)} & -u^{(n)}Y_w^{(n)} & -u^{(n)} \\ 0 & 0 & 0 & X_w^{(n)} & Y_w^{(n)} & 1 & -v^{(n)}X_w^{(n)} & -v^{(n)}Y_w^{(n)} & -v^{(n)} \end{bmatrix} b = 0 \tag{6.2}$$

The aim is to solve for vector $b = [h_{11}, h_{12}, h_{13}, h_{21}, h_{22}, h_{23}, h_{31}, h_{32}, h_{33}]^T$ in equation (6.2). This is a linear least square method problem and is done using Singular Value Decomposition.

6.1.1 Homography Optimization

Due to the presence of noise in the estimated homography from DLT [35], there is need for a non-linear optimization of the homography. This is done through minimization of reprojection error on the image using Levenberg Marquardt algorithm.

For simplicity, let us rewrite the homography as $h = (h^1, h^2, h^3)^T$, where each entry is a 3D vector that represents a row in $\mathscr{H}$. From equation (6.1), we can rewrite estimated $(\hat{u}, \hat{v}, 1)^T$ in its inhomogeneous coordinates as,

$$(\hat{u}, \hat{v}) = (\frac{h^1 P_w}{\lambda}, \frac{h^2 P_w}{\lambda})^T \quad \text{where} \quad \lambda = h^3 P_w \tag{6.3}$$

The optimization method requires parameter vector $\mathscr{H}_{(j)} = [h_{11}, ..., h_{33}]$ for each pose "j", and the function $\mathbf{F}(\mathscr{P}) : (\hat{p}^{(i,j)}, ..., \hat{p}^{(n,m)})$ that contains the reprojected pixels. Next, we need the matrix representation of the first derivative of the function (i.e $[J_h = \frac{f(\mathscr{P})}{\partial \mathscr{H}}]_{(j)}$) known as Jacobian matrix for each pose of the calibration target.

$$\lambda \begin{bmatrix} \hat{u} \\ \hat{v} \\ 1 \end{bmatrix} = \begin{bmatrix} h_{11} & h_{12} & h_{13} \\ h_{21} & h_{22} & h_{23} \\ h_{31} & h_{32} & h_{33} \end{bmatrix} \begin{bmatrix} X_w \\ Y_w \\ 1 \end{bmatrix} \tag{6.4}$$

For the optimization, we need to derive the Jacobian matrix J_h of the homography function. This is done by expressing the derivative of the projected point $\hat{p}$ with respect to $\mathscr{H}$ using quotient rule for derivation as shown below,

$$\begin{aligned} \frac{\partial \hat{p}}{\partial h} &= \frac{\partial(\hat{u}, \hat{v})}{\partial(h^1, h^2, h^3)} = \frac{\partial(\frac{h^1 P_w}{h^3 P_w}, \frac{h^2 P_w}{h^3 P_w})}{\partial h} = \begin{pmatrix} \frac{\partial(\frac{h^1 P_w}{h^3 P_w})}{\partial(h^1)} & 0 & \frac{\partial(\frac{h^1 P_w}{h^3 P_w})}{\partial(h^3)} \\ 0 & \frac{\partial(\frac{h^2 P_w}{h^3 P_w})}{\partial(h^2)} & \frac{\partial(\frac{h^2 P_w}{h^3 P_w})}{\partial(h^3)} \end{pmatrix} \\ &= \begin{pmatrix} \frac{P_w^T}{h^3 P_w} & 0 & \frac{-P_w^T h^1 P_w}{(h^3 P_w)^2} \\ 0 & \frac{P_w^T}{h^3 P_w} & \frac{-P_w^T h^2 P_w}{(h^3 P_w)^2} \end{pmatrix} = \frac{1}{\lambda} \begin{pmatrix} X_w & Y_w & 1 & 0 & 0 & 0 & -X_w \hat{u} & -Y_w \hat{u} & -\hat{u} \\ 0 & 0 & 0 & X_w & Y_w & 1 & -X_w \hat{v} & -Y_w \hat{v} & -\hat{v} \end{pmatrix} \end{aligned} \tag{6.5}$$

Therefore, for a pose j of a calibration target containing n numbers of feature points, we should have a Jacobian of $(2n \times 9)$ dimension, as shown below,

$$J_h = \begin{pmatrix} \frac{\partial \hat{p}^{(i)}}{\partial h} \\ \cdot \\ \cdot \\ \frac{\delta \hat{p}^{(n)}}{\delta h} \end{pmatrix} \equiv \begin{pmatrix} \frac{\partial \hat{u}^{(i)}}{\partial h} \\ \frac{\partial \hat{v}^{(i)}}{\partial h_{11}} \\ \cdot \\ \cdot \\ \frac{\delta \hat{u}^{(n)}}{\delta h_{11}} \\ \frac{\delta \hat{v}^{(n)}}{\delta h_{11}} \end{pmatrix} \tag{6.6}$$

Finally, using the evaluated Jacobian matrix, we can refine the estimated homography with Levenberg-Marquardt iterative using the update equation below,

$$(J_h^T J_h + \lambda I)\Delta = -J_h^T \epsilon \tag{6.7}$$

where ϵ is a 2n-dimensional vector containing the reprojection error to be minimized, I is a (9x9) identity matrix, λ_h is a scale factor that moves the function towards convergence, and Δ (1x9) contains the update values to be added to the initial homography parameters at each iteration steps.

6.2 Zhang extraction

From the estimated homographies $\mathscr{H}_j$ where $j = 1,\ldots,m$ number of poses. We can use the method of Zhang to extract the constrained intrinsic parameter $\mathscr{K}$ unified from all the target poses. The unification of the homography is based on image of the absolute conic [35].

Let us denote h_1, h_2, h_3 as the columns of an homography $\mathscr{H}$ so that,

$$[h_1\ h_2\ h_3] = \lambda \mathscr{K} [r_1\ r_2\ \mathscr{T}] \tag{6.8}$$

Using the orthonormal basis of columns r_1 and r_2 of rotation matrix $\mathscr{R}$, where λ is an arbitary scale, we have

$$0 = r_1^T r_2 = \lambda^2 (\mathscr{K}^{-1} h_1)^T \mathscr{K}^{-1} h_2 \tag{6.9}$$

Hence for $\lambda \neq 0$, equation (6.10) holds where $\mathscr{K}^{-T}$ denotes $(\mathscr{K}^T)^{-1}$

$$0 = h_1^T \mathscr{K}^{-T} \mathscr{K}^{-1} h_2 \tag{6.10}$$

Also, with $r_1^T r_1$=$r_2^T r_2$=1, we obtain

$$h_1^T \mathcal{K}^{-T} \mathcal{K}^{-1} h_1 - h_2^T \mathcal{K}^{-T} \mathcal{K}^{-1} h_2 = 0 \tag{6.11}$$

Equations (6.10) and (6.11) are the two basic constraints imposed on the intrinsic parameters. Since homography has 8 degrees of freedom, then we have 6 extrinsic parameters (3 rotations and 3 translations). We can only obtain two constraints on the intrinsic parameters. Note that $\mathcal{K}^{-T}\mathcal{K}^{-1}$ actually describes the image of the absolute conic $\mathcal{B} = \mathcal{K}^{-T}\mathcal{K}^{-1}$ so that we write,

$$\begin{aligned} h_1^T B h_2 &= 0 \\ h_1^T B h_1 - h_2^T B h_2 &= 0 \end{aligned} \tag{6.12}$$

Using close form solution, we can extract camera intrinsic parameters $\mathcal{K}$ from the image of the absolute conic $\mathcal{B}$. But first we need to solve for $\mathcal{B}$ in the equation (6.12), which is done by rewriting earlier equation in form of sets of linear $Lb = 0$ (LLS) as shown in equation below for all the m homographies,

(6.13)

$$\begin{bmatrix} (h_{11}h_{12} & h_{12}h_{21}+h_{22}h_{11} & h_{22}h_{21} & h_{12}h_{31}+h_{32}h_{11} & h_{22}h_{31}+h_{32}h_{21} & h_{32}h_{31})_{(1)} \\ (h_{11}^2-h_{12}^2 & 2h_{11}h_{21}-2h_{12}h_{22} & h_{21}^2-h_{22}^2 & 2h_{11}h_{31}-2h_{12}h_{32} & 2h_{21}h_{31}-2h_{22}h_{32} & h_{31}^2-h_{32}^2)_{(1)} \\ . & . & . & . & . & . \\ . & . & . & . & . & . \\ (h_{11}h_{12} & h_{12}h_{21}+h_{22}h_{11} & h_{22}h_{21} & h_{12}h_{31}+h_{32}h_{11} & h_{22}h_{31}+h_{32}h_{21} & h_{32}h_{31})_{(m)} \\ (h_{11}^2-h_{12}^2 & 2h_{11}h_{21}-2h_{12}h_{22} & h_{21}^2-h_{22}^2 & 2h_{11}h_{31}-2h_{12}h_{32} & 2h_{21}h_{31}-2h_{22}h_{32} & h_{31}^2-h_{32}^2)_{(m)} \end{bmatrix} \begin{pmatrix} B_{11} \\ B_{12} \\ B_{22} \\ B_{13} \\ B_{23} \\ B_{33} \end{pmatrix} = 0$$

where $b = [B_{11}, B_{12}, B_{22}, B_{13}, B_{23}, B_{33}]^T$ is 6 dimensional vector, L is a $2m \times 6$ matrix. Finally, we can minimize the function to obtain the vector $\hat{b}$.

Indeed, the matrix $\mathcal{B}$ is symmetric and is expresses as below,

$$\mathcal{B} = \begin{bmatrix} B_{11} & B_{12} & B_{13} \\ B_{12} & B_{22} & B_{23} \\ B_{13} & B_{23} & B_{33} \end{bmatrix} = \begin{bmatrix} \frac{1}{f_x^2} & -\frac{\gamma}{f_x^2 f_y} & \frac{v_0\gamma - u_0 f_y}{f_x^2 f_y} \\ -\frac{\gamma}{f_x^2 f_y} & \frac{\gamma^2}{f_x^2 f_y^2} + \frac{1}{f_y^2} & -\frac{\gamma(v_0\gamma - u_0 f_y)}{f_x^2 f_y^2} - \frac{v_0}{f_y^2} \\ \frac{v_0\gamma - u_0 f_y}{f_x^2 f_y} & -\frac{\gamma(v_0\gamma - u_0 f_y)}{f_x^2 f_y^2} - \frac{v_0}{f_y^2} & \frac{(v_0\gamma - u_0 f_y)^2}{f_x^2 f_y^2} + \frac{v_0^2}{f_y^2} + 1 \end{bmatrix} \tag{6.14}$$

We can compute the contents of the $\mathcal{K}$ matrix from $\mathcal{B}$ as,

$$\begin{aligned} v_0 &= \frac{B_{12}B_{13} - B_{11}B_{23}}{B_{11}B_{23} - B_{12}^2} & \lambda &= B_{33} - \frac{B_{12}^2 + v_0(B_{12}B_{13} - B_{11}B_{23})}{B_{11}} \\ f_x &= \sqrt{\frac{\lambda}{B_{11}}} & f_y &= \sqrt{\frac{\lambda B_{11}}{B_{11}B_{22} - B_{12}^2}} \\ \gamma &= -\frac{B_{12} f_x^2 f_y}{\lambda} & u_0 &= \frac{\gamma v_0}{f_y} - \frac{B_{13} f_x^2}{\lambda} \end{aligned} \tag{6.15}$$

Another way to obtain the intrinsic parameters from the matrix $\mathscr{B}$ is given by Cholesky factorization or QR decomposition.

6.3 Regularization by Smoothing

6.3.1 Kernel Smooth Regression (KSR)

Let (x_i, y_i) define set of points where $i = 1,\ldots,n$ number of points. The common method for regression task is the KSR, and done using the Nadaraya-Watson estimator $\mathbb{K}$. It is given in equation (6.16). In the equation, Gaussian form of averaging kernel has been used.

$$\hat{f}(x) = \frac{\sum_{i=1}^{n} \mathbb{K}(x,x_i) y_i}{\sum_{i=1}^{n} \mathbb{K}(x,x_i)}, \text{ where } \mathbb{K}(x,x_i) = exp(-\frac{(x-x_i)^2}{2h^2}) \tag{6.16}$$

If we look closely in the Nadaraya-Watson estimator, we will see that it is indeed a special case of linear polynomial estimator with (pth degree = 0), which we will show next.

We can write the set of linear equation using the Nadaraya kernel $\mathbb{K}$, weight parameter $\beta = (\beta_0,\ldots,\beta_m)$, and linear polynomial basis "$1,(x-x_i),\ldots,(x-x_i)^p$". Then we have,

$$y_i = \mathbb{K}(.)\beta_0 + \mathbb{K}(.)\beta_1(x-x_i) + \ldots + \mathbb{K}(.)\beta_m(x-x_i)^p \tag{6.17}$$

The solution to equation (6.17) is to determine the optimal $\hat{\beta}$ parameter using linear least square method as,

$$\hat{\beta} = \min \sum_{i=1}^{n} [y_i - \mathbb{K}(.)\beta_0 + \mathbb{K}(.)\beta_1(x-x_i) + \ldots + \mathbb{K}(.)\beta_p(x-x_i)^p] \tag{6.18}$$

This is done using weighted least square [7] and the solution is shown in equation (6.19), where **P** is a (n×1+p) matrix, and **B** is a (n×n) matrix that is constructed using the kernel $\mathbb{K}$. One can see that the unknown mean function for the distribution has been assumed to be locally well approximated with Gaussian averaging on neighbors using the Nadaraya kernel.

$$\hat{\beta} = (\mathbf{P}^T\mathbf{B}\mathbf{P})^{-1}\mathbf{P}^T\mathbf{B}y$$

$$\text{where } \mathbf{B} = \begin{bmatrix} \mathbb{K}(x,x_1) & 0 & \ldots & 0 \\ 0 & \mathbb{K}(x,x_2) & \ldots & 0 \\ \vdots & \vdots & \ddots & \vdots \\ 0 & 0 & \ldots & \mathbb{K}(x,x_n) \end{bmatrix}, \mathbf{P} = \begin{bmatrix} 1 & (x-x_1) & \ldots & (x-x_1)^p \\ 1 & (x-x_2) & \ldots & (x-x_2)^p \\ \vdots & \vdots & & \vdots \\ 1 & (x-x_n) & \ldots & (x-x_n)^p \end{bmatrix} \tag{6.19}$$

6.3.2 Spline

Another way to represent the unknown function for the data points distribution is by using spline basis. Suppose various knot points are chosen between the data points, then spline is a piecewise polynomial function that is continuous and has continuous derivatives at these knot points. The knot points are generally chosen in the data at location of rapid changes and/or well spaced in the data points. Splines are naturally parametrized by the use of truncated power basis, but B-spline basis [15] has been shown to provide the best result in terms of implementation, and numerical stability.

Suppose that $j = 1,\dots,m$ number of knots has been well chosen in the data points, $b_j(x) = (b_1,...,b_m)(x)$ are the B-spline basis, and $\beta_j(x) = (\beta_1,...,\beta_m)(x)$ are their associated weights. The linear equation for the regression task with B-spline is :

$$y = \sum_{j=1}^{m} \beta_j b_j(x) + \epsilon \tag{6.20}$$

The solution to the regression using B-spline basis in equation (6.20) is to determine the optimal β parameter that minimize the equation as,

$$\hat{\beta} = min \sum_{i=1}^{n} [y_i - \sum_{j=1}^{m} \beta_j b_j(x)]^2 \tag{6.21}$$

Equation (6.21) is solved using linear least square, and the solution is given in equation (6.22), where the basis $b_j(x)$ has been arranged to form a matrix $\mathbf{B}$. Indeed, $\mathbf{B}$ is a sparse matrix due to the compact support of B-spline basis function, and thus evicts numeric instability.

$$\hat{\beta} = (\mathbf{B}^T\mathbf{B})^{-1}\mathbf{B}^T y$$
$$\mathbf{B} = \begin{bmatrix} b_1(x_1) & \dots & b_m(x_1) \\ \vdots & \ddots & \vdots \\ b_1(x_n) & \dots & b_m(x_n), \end{bmatrix} \tag{6.22}$$

Penalized smoothing spline [17]

Knot placement is an important problem for Spline method, especially under this application where we do not have prior information of the expected 3D profile shape. The solution proposed under penalized smoothing spline is to use every point of the data as a knot point. Thereafter, a parameter λ is introduced to provide desirable smoothing result. The smoothing solution is to extract the optimal $\hat{\beta}$ by minimizing equation (6.23),

$$\hat{\beta} = min \sum_{i=1}^{n} [y_i - f(x_i)]^2 + \lambda \int_{\mathbf{a}}^{\mathbf{b}} [f''(x)]^2 dx \quad \text{where } f(x) = \sum_{j=1}^{m} \beta_j b_j(x) \tag{6.23}$$

If we compare equation (6.23) to (6.21), a roughness penalty term ($\lambda \int [f''(x)]^2 dx$) has been introduced, where "**a**" and "**b**" coefficients are the smallest and largest x values.

$$\lambda \int_{\mathbf{a}}^{\mathbf{b}} [f''(x)]^2 dx \equiv \lambda \beta^T \mathbf{D} \beta \tag{6.24}$$

Thanks to the work of Reinsch [17], the penalty term can be written as a quadratic form in equation (6.24), where **D** is the second moment matrix of **B**. The least square solution to equation (6.23) is given as,

$$\beta = (\mathbf{B}^T \mathbf{B} + \lambda \mathbf{D})^{-1} \mathbf{B}^T y \tag{6.25}$$

The experimental result with different λ values is shown in figure 6.1. This means that at λ equal to 1 ($\lambda = 1$), we end up with a very close fit that follows every detail in the data points, whereas lesser value of λ ($\lambda = 10.5$) produce a smoother fit that is desirable in our application. This is because we prefer to have a curve that is fairly smooth, with less variability.

(a) $\lambda = 0.5$ (b) $\lambda = 1$

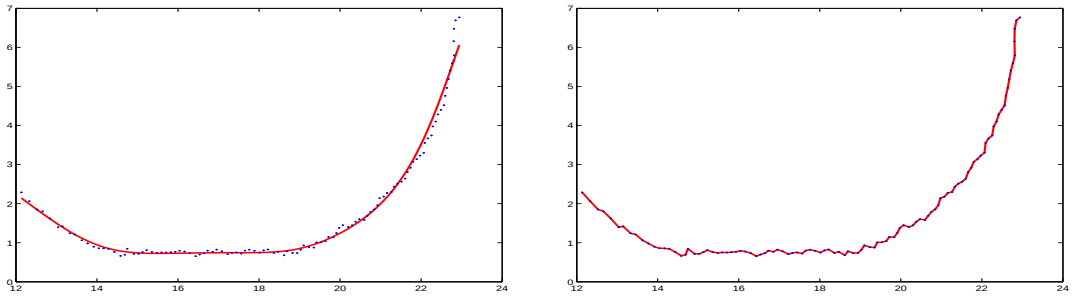

Figure 6.1: Smoothing spline on 3D profile.

6.3.3 KSR vs Spline

We have tested the two smoothing methods (KSR and Spline) on several 2D profiles from our system. An optimal smoothing parameter has been determined through various experiment on different set of 2D profiles. Only the KSR method provides good result in all cases tested.

It respects our earlier assumption that the smoothing output of the flat primitive have to be straight (see figure 6.2). For the spline method, the smoothing result of the line primitive does not conform with our earlier assumption. It is "curve-like", and not straight. It thus requires tuning of parameters every time in order to have acceptable result for different profiles.

(a) KSR

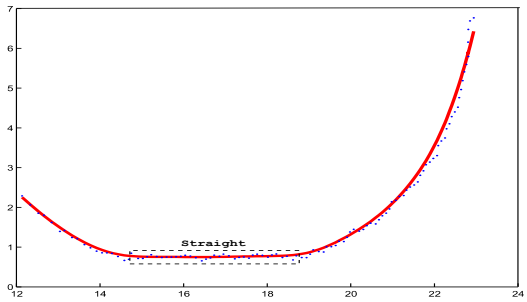

(b) Spline

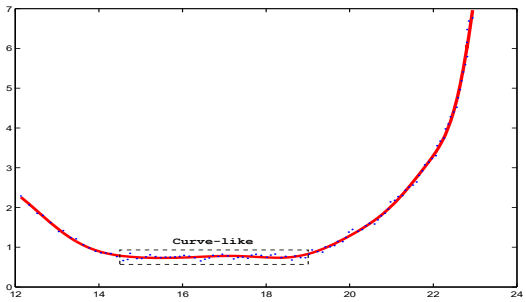

Figure 6.2: KSR vs Spline: Situation where Spline method fails.

CHAPTER 7

APPENDIX B - SCHEIMPFLUG

7.1 Scheimpflug Image Formation

We describe in detail the mathematical description for the Scheimpflug formation model. Under Scheimpflug model, the image plane is first tilted at given angles θ and γ around the axis parallel to the X_c and Y_c but in O_I (see figure 2.5).

7.1.1 Projection Matrix $\mathcal{K}_c^t$

The matrix $\mathcal{K}_c^t$ transform untilted camera coordinate points $p_c(X_c, Y_c, di)_c$ to its tilted camera coordinate points $p_c^t(X_c, Y_c, Z_c)_c$. In figure 7.1, $\vec{n}_I$ is the normal vector to the untilted image plane, while $\vec{n}_t$ is the normal vector to the tilted image plane.

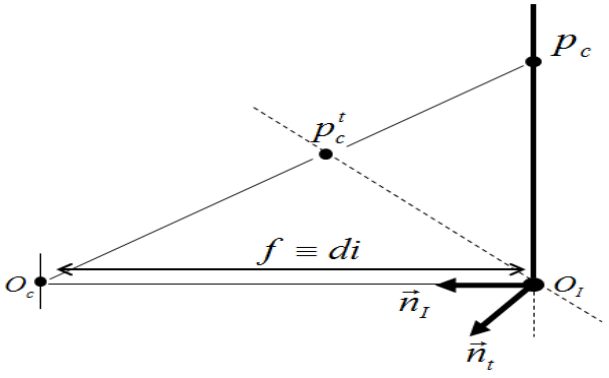

Figure 7.1: Projection in the camera coordinate.

The normal vector $\vec{n}_I$ is perpendicular to the lens plane that is defined by origin $O_c(X_c, Y_c, Z_c)_c$,

and thus written as,

$$\vec{n}_I = [0,0,1]^T \tag{7.1}$$

We can derive the normal vector $\vec{n}_t$ to the tilted image plane by rotating normal $\vec{n}_I$ using rotations through angles θ and γ as shown below,

$$\begin{aligned} \vec{n}_t &= \mathscr{R}_\gamma \mathscr{R}_\theta \, \vec{n}_I \\ \vec{n}_t &= \begin{bmatrix} cos\,\gamma & 0 & sin\,\gamma \\ 0 & 1 & 0 \\ -sin\,\gamma & 0 & cos\,\gamma \end{bmatrix} \begin{bmatrix} 1 & 0 & 0 \\ 0 & cos\,\theta & -sin\,\theta \\ 0 & sin\,\theta & cos\,\theta \end{bmatrix} \begin{bmatrix} 0 \\ 0 \\ 1 \end{bmatrix} \\ \vec{n}_t &= \begin{bmatrix} sin\,\gamma\,cos\,\theta \\ -sin\,\theta \\ cos\,\gamma\,cos\,\theta \end{bmatrix} \end{aligned} \tag{7.2}$$

Using the equation of plane, any tilted camera coordinate points $p_c^t(X_c, Y_c, Z_c)_c$ can be written as in equation (7.3) where d is the signed distance for the plane equation.

$$\vec{n}_t.(X_c, Y_c, Z_c)^T = -d, \tag{7.3}$$

In order to determine the signed distance d, one require a point on the tilted plane. Origin $O_I(0,0,di)_c$ is a point on the tilted plane (see figure 7.1). Therefore, we can solve for d as,

$$\begin{aligned} d &= -\vec{n}_t O_I \\ d &= -di\,cos\,\gamma\,cos\,\theta, \end{aligned} \tag{7.4}$$

Our main aim is to determine the scalar parameter τ of a line equation that passes through two points p_c^t and p_c. It is shown in equation (7.5) where $\overrightarrow{O_c p_c}$ is a vector.

$$\tau = \frac{-d - \vec{n}_t O_c}{\vec{n}_t \overrightarrow{O_c p_c}} \tag{7.5}$$

$$\begin{aligned} \tau &= \frac{di\,cos\,\gamma\,cos\,\theta}{X_c\,sin\,\gamma\,cos\,\theta - Y_c\,sin\,\theta + Z_c\,cos\,\gamma\,cos\,\theta} \\ &= \frac{di}{X_c\,tan\,\gamma - Y_c\,\frac{tan\,\theta}{cos\,\gamma} + Z_c}, \end{aligned} \tag{7.6}$$

Finally, the matrix $\mathcal{K}_c^t$ is shown in equation (7.7). If we change the value of angle γ to zero, we will obtain $\mathcal{K}_c^t$ as a result of single rotation on the axis parallel to the X_c axis alone.

$$\mathcal{K}_c^t = \begin{bmatrix} di & 0 & 0 \\ 0 & di & 0 \\ 0 & 0 & di \\ tan\ \gamma & -\frac{tan\ \theta}{cos\ \gamma} & 1 \end{bmatrix} \tag{7.7}$$

7.1.2 Scheimpflug Rotation

The matrix $\mathcal{K}_s$ contains Scheimpflug rotation matrix $\mathcal{R}_s$ and translation $\mathcal{T}_s$ required to finally lay the points from the lens/camera coordinate to the tilted coordinate:

$$\mathcal{K}_s = \begin{bmatrix} \mathcal{R}s & \mathcal{T}_s \\ 0^T & 1 \end{bmatrix} = \begin{bmatrix} 1 & 0 & 0 & 0 \\ 0 & cos\ \theta & sin\ \theta & 0 \\ 0 & -sin\ \theta & cos\ \theta & 0 \\ 0 & 0 & 0 & 1 \end{bmatrix} \begin{bmatrix} cos\ \gamma & 0 & -sin\ \gamma & 0 \\ 0 & 1 & 0 & 0 \\ sin\ \gamma & 0 & cos\ \gamma & 0 \\ 0 & 0 & 0 & 1 \end{bmatrix} \begin{bmatrix} 1 & 0 & 0 & 0 \\ 0 & 1 & 0 & 0 \\ 0 & 0 & 1 & -di \\ 0 & 0 & 0 & 1 \end{bmatrix}$$

$$\mathcal{K}_s = \begin{bmatrix} cos\ \gamma & 0 & -sin\ \gamma & di\ sin\ \gamma \\ sin\ \theta\ sin\ \gamma & cos\ \theta & sin\ \theta\ cos\ \gamma & -di\ sin\ \theta\ cos\ \gamma \\ cos\ \theta\ sin\ \gamma & -sin\ \theta & cos\ \theta\ cos\ \gamma & -di\ cos\ \theta\ cos\ \gamma \\ 0 & 0 & 0 & 1 \end{bmatrix} \tag{7.8}$$

Next, the transformation of the tilted image points to pixel coordinates is done with Matrix $\mathcal{K}_b$ as shown in equation (7.9). The pixel size s_z can be changed to one since it will finally be canceled out later in the full equation.

$$\mathcal{K}_b = \begin{bmatrix} 1/s_x & 0 & 0 & u_0 \\ 0 & 1/s_y & 0 & v_0 \\ 0 & 0 & 1/s_z & 0 \\ 0 & 0 & 0 & 1 \end{bmatrix} \tag{7.9}$$

Hence, the full formulation to determine the point $p_t(u_t, v_t)_p$ from $p_c(X_c, Y_c, Z_c = di)_c$ is shown in equation (7.11), where where C represent cosine, and S for sine.

$$\lambda\ p_t = \mathcal{K}_b \mathcal{K}_s \mathcal{K}_c^t p_c \tag{7.10}$$

(7.11)
$$\lambda \begin{bmatrix} u_t \\ v_t \\ 1 \end{bmatrix} = \begin{bmatrix} 1/s_x & 0 & 0 & u_0 \\ 0 & 1/s_y & 0 & v_0 \\ 0 & 0 & 1/s_z & 0 \\ 0 & 0 & 0 & 1 \end{bmatrix} \begin{bmatrix} C\,\gamma & 0 & -S\,\gamma & di\,S\,\gamma \\ S\,\gamma\,S\,\theta & C\,\theta & C\,\gamma\,S\,\theta & -di\,C\,\gamma\,S\,\theta \\ S\,\gamma\,C\,\theta & -S\,\theta & C\,\gamma\,C\,\theta & -di\,C\,\gamma\,C\,\theta \\ 0 & 0 & 0 & 1 \end{bmatrix} \begin{bmatrix} di & 0 & 0 & 0 \\ 0 & di & 0 & 0 \\ 0 & 0 & di & 0 \\ tan\,\gamma & -\frac{tan\,\theta}{cos\,\gamma} & 1 & 0 \end{bmatrix} \begin{bmatrix} X_c \\ Y_c \\ Z_c \\ 1 \end{bmatrix}$$

Next, we will simplify equation (7.11) in to a clearer version as in the following,

(7.12)
$$\lambda \begin{bmatrix} u_t \\ v_t \\ 1 \end{bmatrix} = \begin{bmatrix} 1/s_x & 0 & 0 & u_0 \\ 0 & 1/s_y & 0 & v_0 \\ 0 & 0 & 1 & 0 \\ 0 & 0 & 0 & 1 \end{bmatrix} \begin{bmatrix} di(\frac{X_c}{cos\,\gamma} - Y_c\,tan\,\gamma\,tan\,\theta) \\ \frac{di\,Y_c}{cos\,\theta} \\ 0 \\ X_c\,tan\,\gamma - Y_c\frac{tan\,\theta}{cos\,\gamma} + Z_c \end{bmatrix}$$

(7.13)
$$u_t = u_0 + \frac{di(X_c - Y_c\,sin\,\gamma\,tan\,\theta)}{s_x(X_c\,sin\,\gamma - Y_c\,tan\,\theta + Z_c\,cos\,\gamma)}$$

(7.14)
$$v_t = v_0 + \frac{di\,Y_c\,cos\,\gamma}{s_y cos\,\theta(X_c\,sin\,\gamma - Y_c\,tan\,\theta + Z_c\,cos\,\gamma)}$$

7.1.3 Backprojection to the untilted image plane

In order to determine the untilted point directly from the tilted pixels, we backproject equation (7.13) and (7.14) as follows,

(7.15)
$$\frac{s_x\,cos\,\gamma(u_t - u_0)}{s_y\,cos\,\theta(v_t - v_0)} = \frac{X_c}{Y_c} - tan\,\theta\,sin\,\gamma$$
$$\text{so that, } X_c = Y_c(tan\,\theta\,sin\,\gamma + \frac{s_x\,cos\,\gamma(u_t - u_0)}{s_y\,cos\,\theta(v_t - v_0)})$$

From equation (7.14)

(7.16)
$$X_c\,sin\,\gamma - Y_c\,tan\,\theta + Z_c\,cos\,\gamma = \frac{di\,cos\,\gamma}{s_y cos\,\theta(v_t - v_0)} Y_c$$

Rewrite equation (7.15) and (7.16) such that $X_c = X_c$

$$
\begin{aligned}
(\frac{di}{s_y\ cos\ \theta\ tan\ \gamma(v_t - v_0)} + \frac{tan\ \theta}{sin\ \gamma})Y_c - \frac{Z_c}{tan\ \gamma} &= Y_c(tan\ \theta\ sin\ \gamma + \frac{s_x\ cos\ \gamma(u_t - u_0)}{s_y\ cos\ \theta(v_t - v_0)}) \\
\frac{Z_c}{Y_c} = tan\ \gamma(\frac{di}{s_y\ cos\ \theta\ tan\ \gamma(v_t - v_0)} + \frac{tan\ \theta}{sin\ \gamma} - tan\ \theta\ sin\ \gamma - \frac{s_x\ cos\ \gamma(u_t - u_0)}{s_y\ cos\ \theta(v_t - v_0)}) & \\
= \frac{di - s_x\ sin\ \gamma(u_t - u_0)}{s_y\ cos\ \theta(v_t - v_0)} + tan\ \gamma\ tan\ \theta(\frac{1 - sin^2\gamma}{sin\ \gamma}) & \\
= \frac{di - s_x\ sin\ \gamma(u_t - u_0)}{s_y\ cos\ \theta(v_t - v_0)} + tan\ \theta\ cos\ \gamma & \\
Y_c = \frac{Z_c}{cos\ \gamma\ tan\ \theta + \frac{di - s_x\ sin\ \gamma(u_t - u_0)}{s_y\ cos\ \theta(v_t - v_0)}} &
\end{aligned}
\tag{7.17}
$$

Therefore, with $Z_c = di$

$$
Y_c = \frac{di\ s_y\ cos\ \theta(v_t - v_0)}{di - s_x\ sin\ \gamma\ (u_t - u_0) + s_y\ sin\ \theta\ (v_t - v_0)\ cos\ \gamma} \tag{7.18}
$$

To solve for X_c , substitute Y_c in to equation (7.15),

$$
\begin{aligned}
X_c &= Y_c(tan\ \theta\ sin\ \gamma + \frac{s_x\ cos\ \gamma(u_t - u_0)}{s_y\ cos\ \theta(v_t - v_0)}) \\
X_c &= \frac{di(s_x\ cos\ \gamma(u_t - u_0) + s_y\ sin\ \gamma\ sin\ \theta(v_t - v_0))}{di - s_x\ sin\ \gamma(u_t - u_0) + s_y\ sin\ \theta\ cos\ \gamma(v_t - v_0)}
\end{aligned}
\tag{7.19}
$$

7.2 Scheimpflug camera calibration

7.2.1 Levenberg Marquardt

The Levenberg Marquardt iteration method is a slight variation on the Gauss-Newton optimization method, so that it transforms to gradient descent method whenever the Gauss-Newton updates fail. This is done by replacing the Gauss Newton normal equation $J^T J\Delta = -J^T\epsilon$ by an augmented normal equation given below,

$$
(J^T J + \lambda I)\Delta = -J^T\epsilon \tag{7.20}
$$

J is the Jacobian matrix, ϵ is the cost (error) determined by the distance between the measured pixels $\tilde{p}^{(i)}$ and reprojected ones $\hat{p}^{(i)}$, I is an identity matrix, and λ is a form of step-scale that varies from iteration to iteration. A typical initial value of λ is 10^{-3} times the average of the diagonal elements of Hessian matrix $\mathbf{He} = J^T J$.

If the value of Δ obtained by solving the augmented normal equation (7.20) leads to a reduction in the error, then the increment is accepted and λ is divided by a factor (typically 10) before the next iteration. On the other hand if Δ leads to an increased error, then λ is multiplied by the same factor, and the augmented normal equation is solved again. This process continues until

a value of Δ is found that gives rise to a decreased error. The process of repeatedly solving the augmented normal equation for different values of λ until an acceptable Δ is found constitutes one iteration of the LM algorithm. An implementation of the LM algorithm can be seen in the book of Press [98].

One should note that whenever λ is very small, the method is essentially the same as Gauss-Newton iteration, and the process will converge fast to the minimum value. However, if λ is large then the normal equation matrix is approximated by λI, so that the normal equation becomes $\lambda\Delta = -J^T\epsilon$ which is is simply the gradient vector of $\|\epsilon\|^2$, as in gradient descent method. Thus, the LM algorithm transforms between Gauss-Newton iteration, which will cause rapid convergence in the neighbourhood of the solution, and a gradient descent approach, which will guarantee a decrease in the cost function when far from convergence.

7.2.2 Bundle Adjustment

Bundle adjustment [92] can be defined as the problem of simultaneously refining camera parameters that describes a scene geometry, and/or refining 3D estimates of the scene based on an optimization criterion involving the corresponding image projections of all points. The bundle adjustment technique used in this report employs the Levenberg Marquardt (LM) iteration method to minimize the reprojection error.

In order to optimize the Scheimpflug camera parameters in equation (7.21) using the bundle adjustment technique, one need to determine the Jacobian matrix J of the error function, and parameter vector $\mathscr{P}$.

$$min \sum_{j=1}^{m}\sum_{i=1}^{n} \|\tilde{p}^{(i,j)} - \hat{p}^{(i,j)}(\hat{\mathscr{K}},\hat{\mathscr{R}}_{(j)},\hat{\mathscr{T}}_{(j)},\hat{k}_1,\hat{k}_2,\hat{k}_3,\hat{t}_1,\hat{t}_2,\hat{s}_1,\hat{s}_2,\theta,\gamma)\|^2 \tag{7.21}$$

For a simple bundle adjustment, the parameter vector contains only the camera parameters as shown in equation (7.22),

$$\begin{aligned}\mathscr{P} = [&f_x, f_y, sk, u_0, v_0, \mathscr{R}_{(1)}, \ldots, \mathscr{R}_{(m)}, \ldots, \mathscr{T}_{(1)},\\ &\ldots, \mathscr{T}_{(m)}, k_1, k_2, k_3, t_1, t_2, s_1, s_2, c_1, c_2,\\ &\theta, \gamma]\end{aligned} \tag{7.22}$$

Let us represent $\mathscr{K} = (f_x, f_y, sk, u_0, v_0)$, the rotation matrix $\mathscr{R}_{(j)}$ has been converted to 1×3 vector in "rodrigues form", $\mathscr{T}_{(j)}$ is a 1×3 dimensional vector. Let K represent the lens distortion coefficients so that $K = k_1, k_2, k_3, t_1, t_2, s_1, s_2, c_1, c_2$. Therefore, the required Jacobian matrix is shown in equation (7.23). The Jacobian matrix J has a dimension of 2nm $\times$ [5+(3m)+(3m)+9+nm]. If we assume that the number of points n=5 and the number of target pose m=2. Then we should have Jacobian matrix of (20 $\times$ 36) in size.

$$J = \frac{\partial \hat{p}}{\partial \mathscr{P}} = \begin{pmatrix} \frac{\partial \hat{p}^{(i,j)}}{\partial \mathscr{K}}, & \frac{\partial \hat{p}^{(i,j)}}{\partial \mathscr{R}_{(1)}} \cdots \frac{\partial \hat{p}^{(i,j)}}{\partial \mathscr{R}_{(m)}}, & \frac{\partial \hat{p}^{(i,j)}}{\partial \mathscr{T}_{(1)}} \cdots \frac{\partial \hat{p}^{(i,j)}}{\partial \mathscr{T}_{(m)}}, & \frac{\partial \hat{p}^{(i,j)}}{\partial K}, & \frac{\partial \hat{p}^{(i,j)}}{\partial \theta}, & \frac{\partial \hat{p}^{(i,j)}}{\partial \gamma} \\ & & \vdots & & & \\ \frac{\partial \hat{p}^{(n,m)}}{\partial \mathscr{K}}, & \frac{\partial \hat{p}^{(n,m)}}{\partial \mathscr{R}_{(1)}} \cdots \frac{\partial \hat{p}^{(n,m)}}{\partial \mathscr{R}_{(m)}}, & \frac{\partial \hat{p}^{(n,m)}}{\partial \mathscr{T}_{(1)}} \cdots \frac{\partial \hat{p}^{(n,m)}}{\partial \mathscr{T}_{(m)}}, & \frac{\partial \hat{p}^{(n,m)}}{\partial K}, & \frac{\partial \hat{p}^{(n,m)}}{\partial \theta}, & \frac{\partial \hat{p}^{(n,m)}}{\partial \gamma} \end{pmatrix} \tag{7.23}$$

Note : Any parameter block that is not important can be removed from the Jacobian matrix. This is based on which calibration method has been used. For example, in the proposed Scheimpflug **Method I**, the parameter sk, c_1, c_2 block need to be removed from the Jacobian structure of the bundle adjustment.

7.2.3 Scheimpflug Angles Optimization

In reality, the procedure used to optimise the Scheimpflug angles should follow the illustration in figure 7.2. The Scheimpflug angles are optimized between the tilted and untilted image plane. To determine the optimal $\hat{\theta}$ at each iteration, the tilted pixels $\tilde{p}_t$ are backprojected to the untilted plane so that the reprojection error is minimized between the true $\tilde{p}$ and the reprojected $\hat{p}$.

$$min \sum_{j=1}^{m} \sum_{i=1}^{n} \|\tilde{p}^{(i,j)} - \hat{p}^{(i,j)}(\hat{\mathscr{K}}, \hat{\mathscr{R}}_{(j)}, \hat{\mathscr{T}}_{(j)}, \hat{\theta}, \hat{\gamma})\|^2 \tag{7.24}$$

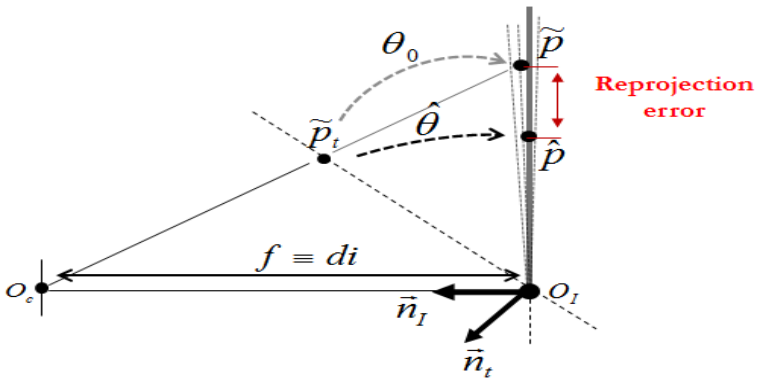

Figure 7.2: Illustration of Scheimpflug angle optimization.

7.3 Fronto-parallel Transformation

To calibrate a camera using a planar calibration target, we must first acquire a set of images of this target according to different poses, to vary the viewpoint of the camera as shown in figure 7.3. The calibration target that is composed of grid circular features is projected on the image plane. These circular features become ellipse-like shapes in the image as a result of the perspective

projection. This makes it difficult to precisely locate the pixel coordinates of the centers of these ellipses (i.e feature pixels).

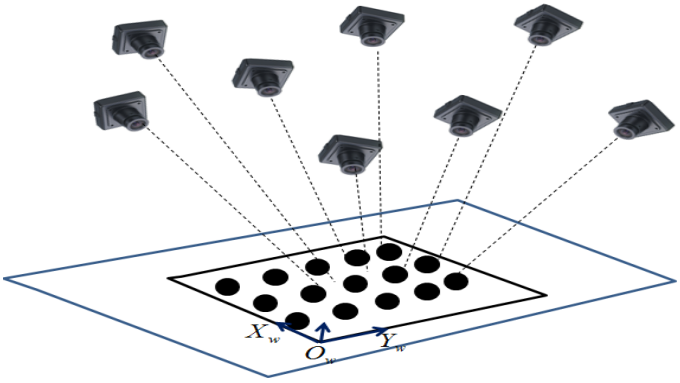

Figure 7.3: Image captured from different viewpoint.

With the Scheimpflug device, these difficulties are even more accentuated, so that the circle grids appear blurred and low contrasted in the acquired images. To improve the accuracy of the camera parameter estimation, we incorporate the fronto-parallel transformation method [14, 97]. This method improves the extraction of the feature pixels. An image is created which looks as if the calibration target has been placed directly in front of the camera (i.e the planar target is perfectly orthogonal to the optical axis of the camera). This is done by projecting all image pixels back onto the object/target plane defined by world coordinate $O_w(X_w, Y_w, Z_w = 0)$ in figure 7.3. The image is created by using the estimated camera parameters ($\mathcal{K}$, $[\mathcal{R}_{(j)}|, \mathcal{T}_{(j)}]$), and distortion coefficients (k_1,k_2,k_3,t_1,t_2, s_1,s_2).

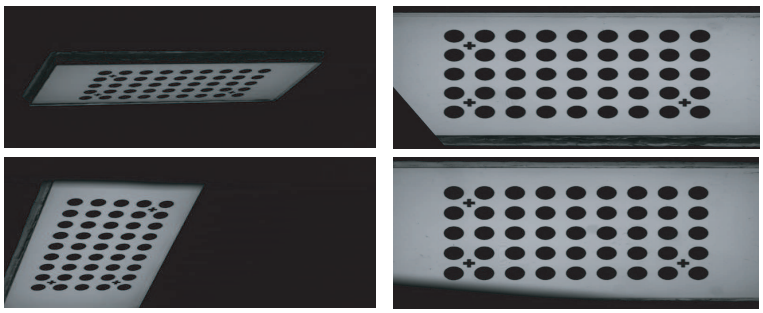

Figure 7.4: Real and resulting frontal images.

The realistic frontal image in this work (see figure 7.4) has been created using cubic interpolation technique [71]. One can see that the resulting images are free from perspective and other deformations. The feature pixels are easy to extract on these images because the dot-grids now have circular shapes with the same radius size. The feature pixels extraction methods such as digital image correlation [97], cross correlation, with sub-pixel detection methods can be used.

These feature pixels can finally be projected back to their real image plane, where Scheimpflug camera calibration method will be performed.

BIBLIOGRAPHY

[1] Y. I. ABDEL-AZIZ AND H. M. KARARA, *Direct linear transformation from comparator coordinates into object space coordinates in close-range photogrammetry*, in proceedings of the symposium on Close-Range photogrammetry, vol. 1, 1971, p. 18.

[2] A.KAMIYA, *Measurement of contact wire wear by laser in the daytime*, in Quarterly Report of Railway Technical Research Institute, Japan, vol. 20, September 1979, pp. 117–121.

[3] T. ASTARITA, *A scheimpflug camera model for stereoscopic and tomographic* PIV, in proceedings of the 16th international symposium on Applications of Laser Techniques to Fluid Mechanics, 2012, pp. 1–9.

[4] D. G. BAILEY, *Subpixel estimation of local extrema*, in proceedings of the Conference on Image and Vision Computing New Zealand, 2003, pp. 414–419.

[5] V. S. BAZIN, Y. V. CHUGUI, S. V. KALICHKIN, V. E. KALIKIN, S. N. MAKAROV, A. G. VERKHOGLIAD, AND I. A. VYKHRISTYUK, *Optical remote inspection of live contact wire cross-sections in a train's electro-supply network*, in Measurement Science and Technology, vol. 18 (6), 2007, p. 1773.

[6] A. BEN-HAMADOU, C. SOUSSEN, C. DAUL, W. BLONDEL, AND D. WOLF, *Flexible calibration of structured-light systems projecting point patterns*, in Computer Vision and Image Understanding, vol. 117 (10), 2013, pp. 1468 – 1481.

[7] A. BJORCK, *Numerical methods for least squares problems*, SIAM, Philadelphia PA, 1996, pp. 165-171.

[8] S. BORROMEO, J. L. APARICIO, AND P. M. MARTINEZ, *MEDES: Contact wire wear measuring system used by the spanish national railway (RENFE)*, in proceedings of the Institution of Mechanical Engineers, Part F: Journal of Rail and Rapid Transit, vol. 217, 2003, pp. 167–175.

[9] D. C. BROWN, *Close-range camera calibration*, in Photogrammetric Engineering, vol. 37 (8), 1971, pp. 855–866.

[10] BVSYS, *Contact wire measuring and inspection system (catenarycheck)*, Accessed January 2012.
http://www.bvsys.de/index.php.

[11] C. CHEN AND A. KAK, *Modeling and calibration of a structured light scanner for 3-d robot vision*, in proceedings of IEEE International Conference on Robotics and Automation, vol. 4, March 1987, pp. 807–815.

[12] N. CHERNOV AND C. LESORT, *Least squares fitting of circles*, in Journal of Mathematical Imaging and Vision, vol. 23 (3), Nov. 2005, pp. 239–252.

[13] Y. CHUGUI, A. VERKHOGLIAD, V. BAZIN, S. KALICHKIN, V. KALIKIN, S. MAKAROV, AND I. VYKHRISTYUK, *Optical remote dimensional inspection of live contact wire in train's electro-supply network*, in Measurement Science Review, vol. 8 (2), 2008, pp. 37–41.

[14] A. DATTA, J. KIM, AND T. KANADE, *Accurate camera calibration using iterative refinement of control points*, in proceedings of 12th IEEE International Conference on Computer Vision Workshops on Visual Surveillance (VS), October 2009, pp. 1201–1208.

[15] M. P. W. DAVID RUPPERT AND R. J. CARROLL, *Semiparametric regression*, in Journal of the American Statistical Association, vol. 101, 2006, pp. 1722–1723.

[16] P. DE RUVO, A. DISTANTE, E. STELLA, AND F. MARINO, *A gpu-based vision system for real time detection of fastening elements in railway inspection*, in proceedings of the 16th IEEE International Conference on Image Processing, Nov 2009, pp. 2333–2336.

[17] A. DEMMLER AND C. REINSCH, *Oscillation matrices with spline smoothing*, in Numerische Mathematik, vol. 24 (5), pp. 375–382.

[18] A. DOUGLAS AND P. E. KERR, *The Scheimpflug principles*, in technical report on the 70th birthday series, issue 2, July 2006.

[19] R. L. EUBANK, *Spline Smoothing and Nonparametric Regression*, Self-Organizing Methods in Modeling, New York, 1988.

[20] EURAILSCOUT, *Contact wire measuring and inspection system*, Accessed February 2013.
http://www.eurailscout.com.

[21] O. FAUGERAS, *Three-dimensional Computer Vision: A Geometric Viewpoint*, MIT Press, Cambridge, MA, USA, 1993.

[22] O. FAUGERAS AND F. LUSTMAN, *Motion and structure from motion in a piecewise planar environment*, Tech. Report RR-0856, June 1988.

[23] H. FENG, Z. JIANG, F. XIE, P. YANG, J. SHI, AND L. CHEN, *Automatic fastener classification and defect detection in vision-based railway inspection systems*, in IEEE Transactions on Instrumentation and Measurement, vol. 63 (4), April 2014, pp. 877–888.

[24] R. B. FISHER AND D. K. NAIDU, *A comparison of algorithms for subpixel peak detection*, in Image Technology, Advances in Image Processing, Multimedia and Machine Vision, Springer-Verlag, 1996, pp. 385–404.

[25] A. FUMI AND A. FORGIONE, *A new complete system for catenary's checking*, in proceedings of the World Congress on Railway Research, Koln, Germany, November 2001.

[26] R. GALIULIN, RISH.M.GALIULIN, J.M.BAKIROV, AND V.V.BYDANOV, *Mobile "OPTEL-CW" system for optoelectronic measurements of contact wire (CW) parameters in railways*, in proceedings of SPIE 7th International Symposium on Laser Metrology Applied to Science, Industry, and Everyday Life, vol. 4900, 2002, pp. 935–940.

[27] R. M. GALIULIN, R. M.GALIULIN, J.M.BAKIROV, V.V.BYDANOV, D.R.BOGDANOV, AND D.V.NAUMOV., *Mobile optoelectronic measurement of a contact net construction in railways*, in proceedings of International Symposium on Automation and Robotics in Construction, 1999, pp. 475–479.

[28] J. M. V. GIGCH, C. SMORENBURG, AND A. W. BENSCHOP, *Le systeme de mesure de l'epaisseur des fils de contact des chemins de fer nederlandais (ns)*, in Rail international (French edition), vol. 22 (4), 1991, pp. 20–31.

[29] J. I. GONZALEZ, J. C. GAMEZ, C. G. ARTAL, AND A. M. N. CABRERA, *Stability study of camera calibration methods*, in proceedings of IEEE Workshop in Agentes Fisicos (WAF), 2005, pp. 271–279.

[30] R. GRABOWSKI, W. SCHWEIZER, J. MOLNAR, AND L. UNGER, *Three-dimensional pictures of industrial scenes applying an optical radar*, in Optics and Lasers in Engineering, vol. 10 (1), 1989, pp. 205–226.

[31] S. K. H. NAGASAWA, T. FUKUTANI, *Development of measuring apparatus for contact wire using sodium vapor lamps*, in Quarterly Report of Railway Technical Research Institute, Japan, vol. 41, Sep. 2000.

[32] C. HAIG, C. HEIPKE, AND M. WIGGENHAGEN, *Lens inclination due to instable fixings detected and verified with vdi/vde 2634 part 1*, technical report by Volkswagen, 2005.

[33] E. L. HALL, J. B. K. TIO, C. A. MCPHERSON, AND F. A. SADJADI, *Measuring curved surfaces for robot vision*, in Computer Journal, vol. 15 (12), Dec. 1982, pp. 42–54.

[34] R. M. HARALICK AND L. G. SHAPIRO, *Image segmentation techniques*, in Computer Vision, Graphics, and Image Processing, vol. 29 (1), 1985, pp. 100–132.

[35] R. HARTLEY AND A. ZISSERMAN, *Multiple View Geometry in Computer Vision*, Cambridge University Press, New York, NY, USA, 2nd ed., 2003.

[36] K. HAUG AND G. PRITSCHOW, *Robust laser-stripe sensor for automated weld-seam-tracking in the ship building industry*, in proceedings of the 24th Annual Conference of the IEEE Industrial Electronics Society (IECON), 1998, pp. 1236–1241.

[37] P. S. HECKBERT AND M. GARLAND, *Survey of polygonal surface simplification algorithms*, tech. report, DTIC Document, 1997.

[38] J. HEIKKILA AND O. SILVEN, *A four-step camera calibration procedure with implicit image correction*, in proceedings of Computer Vision and Pattern Recognition, CVPR, Washington, USA, 1997, pp. 1106–1112.

[39] H. HOFLER, M. DAMBACHER, N. DIMOPOULOS, AND V. JETTER, *Monitoring and inspecting overhead wires and supporting structures*, in proceedings of IEEE Intelligent Vehicles Symposium, 2004, pp. 512 – 517.

[40] Y.-G. HUANG, X.-H. LI, AND P.-F. CHEN, *Calibration method for line-structured light multi-vision sensor based on combined target*, in EURASIP Journal on Wireless Communications and Networking, vol. 2013 (1), 2013, pp. 1–7.

[41] D. HUYNH, *Calibration of a structured light system: a projective approach*, in proceedings of Computer Vision and Pattern Recognition, June 1997, pp. 225–230.

[42] V. KALIKIN, A. VERKHOGLIAD, S. KALICHKIN, S. MAKAROV, V. BAZIN, AND S. SAVKOV, *Automatic optoelectronic system for inspection of wire wear using high-speed image analysis*, in proceedings of 8th International Conference on Measurement, Slovakia, 2011, pp. 201–204.

[43] J. KANNALA AND S. BRANDT, *A generic camera model and calibration method for conventional, wide-angle, and fish-eye lenses*, in IEEE Transactions on Pattern Analysis and Machine Intelligence, vol. 28 (8), Aug 2006, pp. 1335–1340.

[44] H. J. KIM, *Pantograph detection system using image processing techniques*, in Advanced Science and Technology Letters (Information Technology and Computer Science), vol. 85, 2015, pp. 1–4.

[45] N. KOSHIBA, *OCS (overhead catenary system) inspection system for tokyu corporation*, in Meiden review, series no. 3-156, 2012.

[46] S. KUMAR, P. TIWARI, AND S. CHAUDHURY, *An optical triangulation method for non-contact profile measurement*, in proceedings of International Conference on Industrial Technology, Dec 2006, pp. 2878–2883.

[47] S. KUSUMI, *Evolution of overhead catenary system for "shinkansen" high speed railways in japan*, in proceedings of 6th World Congress on High Speed Rail (Amsterdam), 17-19 March 2008.

[48] S. KUSUMI, H. NAGASAWA, AND H. MOCHIZUKA, *Development of measuring apparatus for contact wire wear by sodium vapor lamps*, in proceedings of 17th IEEE Instrumentation and Measurement Technology Conference, vol. 3, 2000, pp. 1404 –1408.

[49] U. LANDAU, *Estimation of a circular arc center and its radius*, in Computer Vision, Graphics, and Image Processing, vol. 38 (3), 1987, pp. 317 – 326.

[50] D. LANMAN AND G. TAUBIN, *Build your own 3d scanner: 3d photography for beginners*, in ACM SIGGRAPH 2009 Courses, SIGGRAPH '09, New York, 2009, ACM, pp. 8:1–8:94.

[51] A. LEGARDA, A. IZAGUIRRE, N. ARANA, AND A. ITURROSPE, *A new method for scheimpflug camera calibration*, in proc. of the 10th IEEE International Workshop of Electronics, Control, Measurement, Signals and their application to Mechatronics (ECMSM), 2011, June 2011, pp. 1–5.

[52] A. LEGARDA, A. IZAGUIRRE, N. ARANA, AND A. ITURROSPE, *Comparison and error analysis of the standard pin-hole and scheimpflug camera calibration models*, in proc. of the 11th IEEE International Workshop of Electronics, Control, Measurement, Signals and their application to Mechatronics (ECMSM), June 2013, pp. 1–6.

[53] J. LI, Y. GUO, J. ZHU, X. LIN, Y. XIN, K. DUAN, AND Q. TANG, *Large depth-of-view portable three-dimensional laser scanner and its segmental calibration for robot vision*, in Optics and Lasers in Engineering, vol. 45 (11), 2007, pp. 1077 – 1087.

[54] H. LOUHICHI, T. FOURNEL, J. M. LAVEST, AND H. B. AISSIA, *Self-calibration of scheimpflug cameras: an easy protocol*, in Measurement Science and Technology, vol. 18 (8), 2007, p. 2616.

[55] L. LUCCHESE, *Geometric calibration of digital cameras through multi-view rectification*, in Image Vision Computing, vol. 23 (5), May 2005, pp. 517–539.

[56] C. MAIR AND S. FARAROOY, *Practice and potential of computer vision for railways*, in IEEE Seminar on Condition Monitoring for Rail Transport Systems (Ref. No. 1998/501), Nov 1998, pp. 10/1–10/3.

[57] F. MAIRE, *Vision based anti-collision system for rail track maintenance vehicles*, in proceedings of IEEE Conference on Advanced Video and Signal Based Surveillance (AVSS), Sept 2007, pp. 170–175.

[58] F. D. MAIRE AND A. BIGDELI, *Obstacle-free range determination for rail track maintenance vehicles*, in proceedings of 11th International Conference on Control, Automation, Robotics and Vision, December 2010, pp. 2172–2178.

[59] F. MAIRESSE, T. M. SLIWA, M. ROY, AND Y. VOISIN, *Needle-shape quality control by shadowgraphic image processing*, in Optical Engineering, vol. 50 (2), 2011.

[60] L. MAISONOBE, *Finding the circle that best fits a set of points*, in Tech. report, 2007.

[61] V. MATIUKAS AND D. MINIOTAS, *Detection of laser beam's center-line in 2d images*, in Elektronika Elektrotechnika, vol. 7, 2009, pp. 67–70.

[62] A. M. MCIVOR, *Calibration of a laser stripe profiler*, in proceedings of 2nd International Conference on 3-D Digital Imaging and Modeling, 1999, pp. 92–98.

[63] T. MELEN, *Geometrical modelling and calibration of video cameras for underwater navigation*, PhD thesis, Norges tekniske hogskole, Institut for teknisk kybernetikk, 1994.

[64] H. M. MERKLINGER, *View camera focus and depth of field*, in VIEW CAMERA magazine, July-October 1996, pp. 55–57.

[65] A. MOLDER, O. MARTENS, T. SAAR, AND R. LAND, *Laser line detection with sub-pixel accuracy*, in Elektronika ir Elektrotechnika, vol. 20 (5), 2014, pp. 133–135.

[66] F. MONTREUIL, R. KOUADIO, C. PETITJEAN, L. HEUTTE, AND V. DELCOURT, *Automatic extraction of information for catenary scene analysis*, in proceedings of 16th European Signal Processing Conference (EUSIPCO'08), Lausanne, Switzerland, Aug. 2008.

[67] R. MULLER, *Contact wire wear measurement devices: A system comparison*, in Quarterly Report of Railway Technical Research Institute, Japan, vol. 41, Sep. 1997.

[68] E. A. NADARAYA, *On Estimating Regression*, in Theory of Probability and Its Application, vol. 9(1), 1964, pp. 141–142.

[69] C. PETITJEAN, L. HEUTTE, R. KOUADIO, AND V. DELCOURT, *Automatic extraction of droppers in catenary scenes*, in proceedings of 11th IAPR Conference on Machine Vision Applications, Yokohama, Japan, May 2009, pp. 497–500.

[70] P.POHL, *3der hagener video-messtriebwagen*, in Der Eisenbahningenieur, vol. 6 (7), 1996, pp. 32–35.

[71] A. PRAJAPATI, S. NAIK, AND S. MEHTA, *Evaluation of different image interpolation algorithms*, in International Journal of Computer Applications, vol. 58 (12), November 2012, pp. 6–12.

[72] L. QI, Y. ZHANG, X. ZHANG, S. WANG, AND F. XIE, *Statistical behavior analysis and precision optimization for the laser stripe center detector based on steger's algorithm*, in Opt. Express, vol. 21 (11), Jun 2013, pp. 13442–13449.

[73] L. H. R. KOUADIO, V. DELCOURT AND C. PETITJEAN, *Video based catenary inspection for preventive maintenance on iris 320*, in SNCF technical report, 2008.

[74] U. RAMER, *An iterative procedure for the polygonal approximation of plane curves*, in Computer graphics and image processing, vol. 1 (3), 1972, pp. 244–256.

[75] U. RICHTER AND R. SCHNEIDER, *Automated optical inspection of overhead contact line systems*, in Siemens AG technical report, 2004.

[76] W. RUFF, K. ALIBERTI, M. GIZA, W. POTTER, B. REDMAN, AND B. STANN, *Translational doppler detection using direct-detect chirped amplitude-modulated laser radar*, in Microwave and Optical Technology Letters, vol. 43 (4), 2004, pp. 358–363.

[77] M. SACCHI, L. ASCARI, S. CAGNONI, A. PIAZZI, D. SPAGNOLETTI, AND J. POMBO, *Pantobot: A computer vision system for the automatic inspection of locomotive pantographs*, in proceedings of the 1st International Conference on Railway Technology: Research, Development and Maintenance, paper 187, Civil-Comp Press, Stirlingshire, UK, 2012.

[78] J. SALVI, X. ARMANGUE, AND J. BATLLE, *A comparative review of camera calibrating methods with accuracy evaluation*, in Pattern Recognition, vol. 35 (7), 2002, pp. 1617 – 1635.

[79] D. SANTOSH KUMAR AND C. JAWAHAR, *Robust homography-based control for camera positioning in piecewise planar environments*, in Computer Vision, Graphics and Image Processing, vol. 4338 of Lecture Notes in Computer Science, Springer Berlin Heidelberg, 2006, pp. 906–918.

[80] U. SCHULZ AND K. BÖHNKE, *Calibration methods for a 3d triangulation based camera*, in proceedings of International Conference on Research and Education in Robotics - EUROBOT 2009, Springer Berlin Heidelberg, 2009, pp. 131–143.

[81] G. SIBLEY, C. MEI, I. REID, AND P. NEWMAN, *Vast scale outdoor navigation using adaptive relative bundle adjustment*, in International Journal of Robotics Research, vol. 29 (8), July 2010, pp. 958 – 980.

[82] S. N. SINHA, D. STEEDLY, AND R. SZELISKI, *A multi-stage linear approach to structure from motion*, in ECCV 2010 Workshop on Reconstruction and Modeling of Large-Scale 3D Virtual Environments, Springer Verlag, September 2010.

[83] C. SMORENBURG AND A. L. G. VALKENBURG, *Automatic inspection of railway overhead wires*, in proceedings of SPIE on Industrial Inspection, vol. 1010, 1988, pp. 107–117.

[84] E. W. Y. SO, S. MICHIELETTO, AND E. MENEGATTI, *Calibration of a dual-laser triangulation system for assembly line completeness inspection*, in proceedings of International Symposium on Robotic and Sensors Environments ROSE, 2012, pp. 138–143.

[85] H. SPÄTH, *Orthogonal least squares fitting by conic sections*, in Proceedings of the 2nd International Workshop on Recent Advances in Total Least Squares Techniques and Errors-in-variables Modeling, Philadelphia, PA, USA, 1997, Society for Industrial and Applied Mathematics, pp. 259–264.

[86] S.TABAYASHI, M. NIWAKAWA, M. IKEDA, AND T. KOYAMA, *Development of advanced OCS inspection system using image processing technology*, in 9th World Congress on Railway Research (WCRR:11), Lille, France, May 2011.

[87] C. STEGER, *Extraction of curved lines from images*, in proceedings of the 13th IEEE International Conference on Pattern Recognition, vol. 2, 1996, pp. 251–255.

[88] E. STELLA, P. MAZZEO, M. NITTI, C. CICIRELLI, A. DISTANTE, AND T. D'ORAZIO, *Visual recognition of missing fastening elements for railroad maintenance*, in proceedings of 5th IEEE International Conference on Intelligent Transportation Systems, 2002, pp. 94–99.

[89] G. SUBRAHMANYAM, A. RAJAGOPALAN, AND R. ARAVIND, *A recursive filter for despeckling sar images*, in IEEE Transactions on Image Processing, vol. 17 (10), Oct 2008, pp. 1969–1974.

[90] Q. SUN, J. CHEN, AND C. LI, *A robust method to extract a laser stripe centre based on grey level moment*, in Optics and Lasers in Engineering, vol. 67 (0), 2015, pp. 122 – 127.

[91] TOKYU, *Contact wire inpection system for tokyu corporation*, Accessed January 2013. `http://www.tokyu.co.jp/global/index.html`.

[92] B. TRIGGS, P. F. MCLAUCHLAN, R. I. HARTLEY, AND A. W. FITZGIBBON, *Bundle adjustment - a modern synthesis*, in proceedings of the International Workshop on Vision Algorithms: Theory and Practice, ICCV '99, London, UK, 2000, Springer-Verlag, pp. 298–372.

[93] R. Y. TSAI, *A versatile camera calibration technique for high-accuracy 3D machine vision metrology using off-the-shelf TV cameras and lenses*, in IEEE Journal of Robotics and Automation, vol. 3 (4), Aug. 1987, pp. 323–344.

[94] T.SHIMADA, T. KOHIDA, AND Y. SATOH, *Development of a solid laser measuring apparatus of contact wire wear*, in Quarterly Report of Railway Technical Research Institute (RTRI), Japan, vol. 98, March 1997, pp. 19–24.

[95] A. B. TSYBAKOV, *Introduction to Nonparametric Estimation*, Nonparametric estimators, Springer, New York, 2009, pp. 1–76.

[96] R. USAMENTIAGA, J. MOLLEDA, AND D. GARCIA, *Fast and robust laser stripe extraction for 3d reconstruction in industrial environments*, in Machine Vision and Applications, vol. 23 (1), Springer Berlin / Heidelberg, 2012, pp. 179–196.

[97] M. VO, Z. WANG, L. LUU, AND J. MA, *Advanced geometric camera calibration for machine vision*, in Optical Engineering, vol. 50 (11), 2011, pp. 110503/1–10503/3.

[98] S. T. W. PRESS, B. FLANNERY AND W. VETTERLING, *Numerical recipes in C*, Cambridge University Press, 1998.

[99] J. WANG, F. SHI, J. ZHANG, AND Y. LIU, *A new calibration model of camera lens distortion*, in Pattern Recognition, vol. 41 (2), 2008, pp. 607 – 615.

[100] G.-Q. WEI AND S. D. MA, *Implicit and explicit camera calibration: theory and experiments*, in IEEE Transactions on Pattern Analysis and Machine Intelligence, vol. 16 (5), May 1994, pp. 469–480.

[101] Z. WEI, M. XIE, AND G. ZHANG, *Calibration method for line structured light vision sensor based on vanish points and lines*, in proceedings of International Conference on Pattern Recognition (ICPR), 2010, pp. 794–797.

[102] Z. WEI, G. ZHANG, AND Y. XU, *Calibration approach for structured-light-stripe vision sensor based on the invariance of double cross-ratio*, in Optical Engineering, vol. 42 (10), 2003, pp. 2956–2966.

[103] J. WENG, P. COHEN, AND M. HERNIOU, *Calibration of stereo cameras using a non-linear distortion model [ccd sensory]*, in proceedings of the 10th International Conference on Pattern Recognition, vol. 1, Jun 1990, pp. 246–253.

[104] J. WENG, P. COHEN, AND M. HERNIOU, *Camera calibration with distortion models and accuracy evaluation*, in IEEE Trans. Pattern Anal. Mach. Intell., vol. 14 (10), Oct. 1992, pp. 965–980.

[105] E. R. WHITE, *Assessment of line-generalization algorithms using characteristic points*, in The American Cartographer, vol. 12 (1), 1985, pp. 17–28.

[106] B. WIENEKE, *Stereo-PIV using self-calibration on particle images*, in Experiments in Fluids, vol. 39 (2), 2005, pp. 267–280.

[107] K. YAMAUCHI, H. SAITO, AND Y. SATO, *Calibration of a structured light system by observing planar object from unknown viewpoints*, in proceedings of the 19th IEEE International Conference on Pattern Recognition, 2008.

[108] H. ZHANG, J. YANG, W. TAO, AND H. ZHAO, *Vision method of inspecting missing fastening components in high-speed railway*, in Applied Optics, vol. 50 (20), Jul 2011, pp. 3658–3665.

[109] J. ZHANG AND A. DJORDJEVICH, *Study on laser stripe sensor*, in Sensors and Actuators A: Physical, vol. 72 (3), 1999, pp. 224 – 228.

[110] J. ZHANG, J. SUN, Z. LIU, AND G. ZHANG, *A flexible calibration method for laser displacement sensors based on a stereo-target*, in Measurement Science and Technology, vol. 25 (10), 2014, p. 105103.

[111] Z. ZHANG, *A flexible new technique for camera calibration*, in IEEE Transaction on Pattern Analysis and Machine Intelligence, vol. 22 (11), Nov. 2000, pp. 1330–1334.

[112] F. ZHOU AND G. ZHANG, *Complete calibration of a structured light stripe vision sensor through planar target of unknown orientations*, in Image and Vision Computing, vol. 23 (1), 2005, pp. 59 – 67.

[113] M. H. ZWEMER, J. M. VAN DE WOUW, E. G. T. JASPERS, AND S. ZINGER, *A vision-based approach for tramway rail extraction*, in SPIE proceedings of conference on Video Surveillance and Transportation Imaging Applications, vol. 9407 OR, March 2015, pp. OR–35.